DOSIMETRY OF SMALL FIELDS USED IN STEREOTACTIC RADIOSURGERY WITH 15-MV PHOTONS FROM A LINEAR ACCELERATOR

A THESIS

Submitted to the Graduate Faculty of the
Louisiana State University
Agricultural and Mechanical College
in partial fulfillment of the
requirements for the degree of

Masters of Science

in

Nuclear Science Center
(Medical Radiation Science Option)

by

Steven Cooper Harrell
B.S., Louisiana State University, 1987
May, 1992

ACKNOWLEDGMENTS

I would like to take this opportunity to thank the staff at Mary Bird Perkins Cancer Center and the LSU Nuclear Science Center for their encouragement and support. A very special thanks goes to my mentor Dr. Hidalgo-Salvatierra, Senior Vice President of Physics and Engineering for his patience, the long hours spent in guiding me along my path, and the encouragement to continue. My special thanks to Dr. Sheldon Johnson, M.D., Dr. Robert Fields, M.D., Carrie Rudolf, M.S. of Mary Bird Perkins Cancer Center and Dr. Edward N. Lambremont of the Nuclear Science Center at Louisiana State University for serving on my committee. A thanks to Dr. Bailey Pullen, Ph.D. for his advice and encouragement throughout my internship at Mary Bird Perkins Cancer Center and while writing my thesis.

Most of all, I want to thank my wife Toni for her love and support throughout this endeavor, for the help in writing this thesis even though she did not understand what I was doing and raising our children Maegan and Stephanie single-handedly during this period.

To my parents, thanks for caring and loving me and most of all believing in me.

TABLE OF CONTENTS

TABLE OF CONTENTS
(Continued)

LIST OF TABLES

LIST OF TABLES
(Continued)

LIST OF FIGURES

LIST OF FIGURES
(Continued)

LIST OF FIGURES
(Continued)

LIST OF FIGURES
(Continued)

LIST OF FIGURES
(Continued)

ABSTRACT

Dosimetric parameters have been determined for the small fields used in stereotactic radiosurgery utilizing the 15 MV photons from a Varian Clinac 20 linear accelerator. The specific parameters measured consisted of linear attenuation coefficients both narrow beam and TMR derived ($\mu_o(cm^{-1})$), fractional depth dose (FDD), total scatter correction factor (S_t), collimator scatter correction factor (S_c), phantom scatter factor (S_p), and tissue maximum ratio (TMR). Radiographic methods were utilized for cross profile determination due to its high spatial resolution in tandem with computer controlled beam scanner utilizing the diode detector. Isodensity plots for each cone were determined in the three principle planes (axial, sagittal, and coronal) utilizing radiographic methods and TLD.

The fractional depth dose and tissue maximum ratios showed the characteristic rapid dose fall off at shallow depths towards the zero area values for the small fields and approached the zero area values at deeper depth for the same field sizes. The total scatter correction factor showed a rapid dose fall off for the small field sizes towards the zero area and a divergence from the expected curve due to the constant head scatter. The collimator scatter factor displayed a constant output for each cone and the same divergence as seen from the total scatter curve. The phantom scatter component did not display this characteristic curve since it is collimator field size independent and only dependent on area of phantom irradiated.

INTRODUCTION

The idea of using radiation as a treatment tool for benign and malignant intracranial diseases has grown over the last three decades. Besides the use of conventional radiotherapy, which is accomplished with standard therapy equipment, relatively large field sizes, and standard dose fractionation regimens, two recently specialized techniques for brain irradiation have been developed. The first technique is the use of stereotactically placed intracranial implants using sealed radioactive sources (Gutin et al., 1981, Hosobuchi et al., 1980, Mackay et al., 1982) and the second technique is the use of very small well collimated multi-arced photon beam on a localized target (Colombo et al., 1985, Hariz etal., 1990, Hartmann et al., 1985, Houdek et al., 1985, Larsson et al., 1974, Leksell et al., 1951,1983,1987, Podgorsak et al., 1989).

Until recently the use of narrow beams smaller than 5x5cm in clinical situations have been limited due to numerous problems associated with determining the dosimetric parameters and the localization methods necessary for this precision work. The use of these small narrow beams; however, gained a strong following with the advancement of high resolution imaging techniques and the development of dosimetric tools capable of determining the data necessary for small field dosimetry. The reported uses of these small narrow beams have been limited to a combined approach with the stereotactic head frame for multiple arc rotations for selected intracranial lesions whether benign or malignant.

In 1951, Lars Leskell developed the use of stereotactically placed narrow beams of photon radiation which was focused on a target volume within the brain using 200 kVp x-rays. The general aim of this type of treatment with small highly defined narrow beams was to achieve a high dose of radiation to a defined volume of tissue which would cause necrosis within the target volume and be clinically comparable to surgical removal of the tissue. The pencil like beams are distributed in such a way that the entrance and exit dose outside the target volume would not adversely affect normal tissue surrounding the target volume. Leksell then introduced a radiosurgical unit utilizing 179 isocentrally focused cobalt-60 gamma ray producing sources. Another possibility was to utilize the Bragg peak isodose characteristics of high energy charged particles such as those produced in cyclotrons or synchrocyclotrons (Larsson et al., 1974, Leksell et al., 1983, Phillips et al., 1989). The use of the Bragg peak method began in the 1950's. These specialized treatments are only possible in a few select centers such as Uppsala, Berkeley, Loma Linda, and Boston. Furthermore, the high capital cost prohibits this technique from being widely used.

In 1974, Larsson et al., had proposed the use of the linear accelerator as an alternate choice for performing the task of small field irradiation. The modern linear accelerator permits a precise dose concentration to be administered via a well collimated narrow photon beam directed towards the isocenter utilizing the multiple arc technique. Several centers have now established radiosurgical techniques using the linear accelerator. Some centers use a single plane 360 degree arc rotation and others have developed more complicated

multiple converging arc techniques. The single arc technique is very simple and does give the steep dose fall-off perpendicular to the beam. The dose gradient, in the plane of rotation, is very shallow due to the infinite number of parallel opposed beams. If the arc rotation is smaller than 180 degrees the problem of parallel opposed beams is diminished. However, the integral dose outside the target volume is worse since the dose is spread over a smaller volume (Hartmann et al., 1985, Pike et al., 1990, Podgorsak et al., 1989). Therefore, to improve the dose fall-off a multiple non-coplanar arc technique was developed (Chierego et al., 1988, Colombo et al., 1985, Hariz et al., 1990, Hartmann et al., 1985, Houdek et al., 1985, Jones et al., 1989, Lutz et al., 1988, Marin-Grez, 1983, Pike et al., 1987, Saunders et al., 1988, Strum et al., 1987). Though differing in their methods, the basic premise is that the target center is placed at the machine isocenter stereotactically. A series of gantry arc movements plus treatment table movements are made to optimize the dose gradient and spread the dose outside the target volume over a large area.

The differences between narrow beam and conventional radiotherapy in brain irradiation are:

1. Small volumes are treated, whereas, whole brain treatments are given by conventional methods for the same tumor.

2. Due to the small beams being utilized, a more precise localization method has to be used to prevent geometric misses.

3. The dose gradient at the beam edges are more pronounced than conventional radiotherapy to allow for the rapid dose fall-off necessary to minimize normal tissue doses.

4. Large dose gradients due to beam size and positioning of the auxiliary cones.

5. Complexness of the treatment procedure compared to conventional radiotherapy.

The narrow well collimated beams have been selectively used to treat lesions found within the brain or Arteriovenous Malformations (AVMs) with diameters of several millimeters to several centimeters. Due to the small diameter field sizes used, the requirements for a successful procedure are: (a) Accurate determination of the target volume (+/- 1mm), (b) Accurate spatial (+/- 2mm) and numerical (+/- 2%) delivery of the dose to the target (Pike et al., 1987, Podgorsak et al., 1989, Rice et al., 1987).

The purpose of this study was the determination of the dosimetric data necessary to treat with small well collimated beams utilizing an auxiliary collimation system with implications for further study for a possible radiosurgical program. This included the determination of the cross profiles, depth dose, scatter correction factors, tissue maximum ratios, and stationary and rotational isodose distributions.

The experiments were done using, for convenience at that time, a 15 MV x-ray producing linear accelerator manufactured by Varian Systems Inc. The Clinac-20 is a isocentrically mounted machine (SAD 100cm) with a standing wave design, a tungsten target, and lead flattening filter. The measured ionization ratio was .768 with a nominal accelerating potential of 13 MV (Task Group 21, 1983). The Clinac-20 has full rotational capabilities for arc therapy with rates variable from 0.5 to 5.0 mu per degree of rotation.

The dosimetric parameters were measured utilizing numerous ionization chambers, diode, film, and TLDs in conjunction with an automatic beam scanner manufactured by CRS Inc. and numerous water and

plastic phantoms. The determination of the dosimetric parameters for small fields poses a two-fold problem utilizing conventional dosimetry equipment. First, the loss of lateral equilibrium across the detection system due to the rapid dose fall-off from the central axis to the beam edge on the order of 10%/mm. The final consideration is the inability to resolve the large dose gradients present and adequately measure off-axis points. The multiple arc technique designed for this study was a modified form used by Hartmann et al of a well collimated small diameter beam utilizing five non-coplanar rotational beams each directed towards the machine isocenter (target center within the patient), enabling a very high dose to be delivered to the target volume and minimizing normal tissue dose. Assuming that the linear accelerator, treatment couch, and target center can be adjusted to very close tolerances so that all major axes and the target central point meet at the isocenter, a relationship between the target volume and the 90% isodose line with a few error modifications can be used to specify the cone diameter for treatment use.

MATERIALS

A. Description of Secondary Collimator System

The conventional collimation system is unsuitable for stereotactic radiosurgery due to the distance from the isocenter (Hartmann et al., 1985, Lutz et al., 1988, Saunders et al., 1988). The idea behind radiosurgery is to deliver a high dose of radiation to the target volume and limit the surrounding normal tissue to a small dose. This is accomplished by a rapid dose fall-off in the penumbra region; however, the conventional collimator penumbra is too large to give the rapid fall-off desired and severely compromises small field beam alignment (Lutz et al., 1988). Small movements of the collimator would transfer into unacceptable movements of the beam at isocenter (Lutz et al., 1988). Therefore, a rigid secondary collimation system was custom built by Radiation Products Design and fits into the accessory tray slot on the accelerator head. By design, the custom built collimator improves beam collimation over the primary collimator and in conjunction with the small beam spot of the accelerator, minimizes the penumbra and thereby increases the dose fall-off outside the target volume (Hartmann et al., 1985, Lutz et al., 1988, Rice et al., 1987, Saunders et al., 1988). Assuming that the tumor volume is spherically symmetrical, the shape of the isodose curves produced from circular fields are best suited to give the desired spherical isodose distribution in the convergent beam method over rectangular fields (Hartmann et al., 1985, Lutz et al., 1988). The secondary collimator system consist of an aluminum plate that fits into the accessory mounting slot of the accelerator head and a threaded

stainless steel cup attachment which houses the lead collimator cones (Figure 1). The cones are 10cm in height and 6cm in outside diameter. The distance from source to bottom of collimator cup attachment is 64.5cm. Each clinical cone was designed from the results obtained with a set of experimental cone. The design produces a beam edge which is sharper than those defined by the accelerator's collimator. The primary collimator field size was set to a 5x5cm field size for all experiments. The initial set of cones A to E (Figure 2) are referred to as the experimental cones in this thesis. The data generated by this set of cones was used to design the final set of cones ready to use for clinical treatment and are referred to as clinical cones.

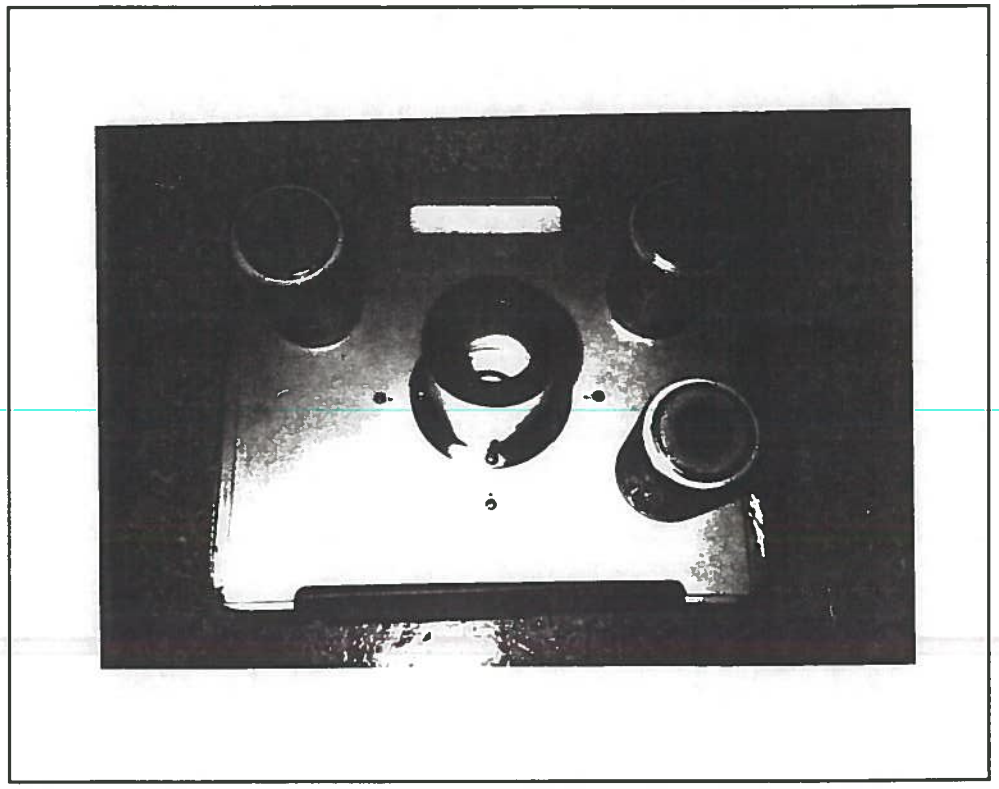

Figure 1 Secondary collimator system with stainless steel cup (center) and clinical inserts - cone 1 (upper left corner), cone 2 (upper right corner), and cone 3 (lower right corner).

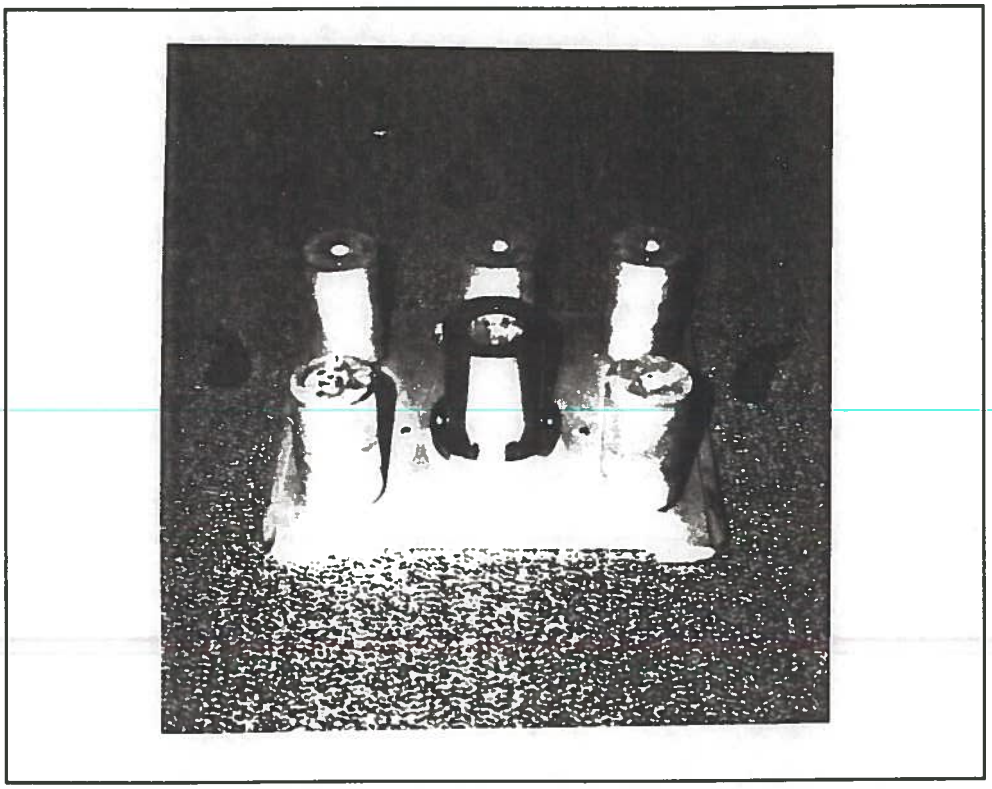

Figure 2 Experimental cones A-E (top row A-C bottom row D and E looking left to right) with stainless steel cup in center.

B. Beam Scanning System

The ionization and profile measurements were made utilizing the CRS x-y radiation beam scanner. The scanner is a two-dimensional data acquisition system designed by Comrad System, Inc. The CRS system is based on AT compatible 286 computer with a 30 megabyte hard drive running Quickbasic 3.0. The computer whether a portable or standard desk top model is modified to include the interface board to control scanner movements. The beam data is acquired by means of a specially designed computer board which combines the electrometer amplifier and an analog to digital converter for data conversion from an electrical signal to a useful digital signal. The software package is written in Quickbasic and includes screen and plotting display of multiple scans of central axis depth dose and cross beam profiles; numeric values of symmetry and flatness displayed on screen and plotter; scan data in numeric printout in 1mm steps; generation of fractional depth dose (FDD) and tissue maximum ratio (TMR) tables; and raw data storage capabilities for future data analysis and data manipulation allowing editing, scaling and zooming in on areas of interest. The CRS data acquisition system requires that the depth of maximum reading in relation to the water/air interface be determined for each experiment. The CRS system will automatically determine both values if the calibration protocol setup by CRS is followed.

C. Artronix Film Dosimetry System

The dosimetry system (model 3301) consist of the isodose processor (model 3307), X-Y recorder (model 1655), and isodensitometer (model

1705). The isodensitometer system scans relative density patterns from maximum to minimum percentage density patterns. The isodose processor features automatic (10% decrements) or manual (0.1% decrements) percent isodensity tracking with the maximum being 100 percent. Cross profile scans in the linear mode produce a scaleable plot of true position versus percent density and all plots are automatically produced in lifesize format.

D. Dosimeters

1. Ionization chambers

The ionization chamber is the most widely used type of dosimeter today for relative and absolute measurements in radiation therapy. Cavity ionization chambers come in many shapes and chamber volumes, but basically consist of a solid wall surrounding a gas filled cavity in which an electric field is established to collect the ionization that occur in the gas filled cavity.

a. The PTW 0.6cc Farmer type chambers (model 30-351 and 30-352) have a volume of 0.6cc and the chamber wall is constructed of acrylic with a thickness of 0.5mm. The chambers cavity dimensions are 6.1mm in diameter and 20.7mm long. For accelerator calibration the model 30-352 was placed in water with the 0.46cm acrylic buildup cap and was used along with a penrose drain to effectively waterproof this chamber.

b. The PTW model 30-316 SN 233641 #703 is a waterproof cylindrical ionization chamber that has a collection volume of 0.3cc. The chamber wall material is made of acrylic with a thickness of 0.75mm. The chamber's cavity dimensions are 5.5mm in diameter and 14mm in length.

c. The PTW model 30-350 #162031 is also a waterproof cylindrical ionization chamber. This chamber has a collection volume of 0.1cc with the wall thickness

of 1.75mm of acrylic. The cavity dimensions are 3.5mm in diameter and 10mm in length.

d. The PTW/Markus Parallel Plate ionization chamber (model 30-329) SN 23343-291 has a collecting volume of 0.04cc. The chamber design is not of a cylindrical type, but flat with a cylindrical acrylic body whose collecting dimensions are 5mm in diameter and 2mm in height. The chamber's window is the polarizing electrode which is made of polyethylene layered with graphite, The collector is also made of polyethylene layered with graphite with an effective diameter of 4.6mm. The chamber uses a 1mm acrylic cap to waterproof the chamber for in water readings. Because of the small collecting volume this chamber proved to be ideal for determining all of the necessary parameters for small field dosimetry.

2. Solid state dosimeters

There exist several solid state dosimeter types that can be used for dosimetry purposes i.e. diode, thermoluminescent dosimeters (TLD), and film. The thermoluminescent dosimeter is regarded as the solid state dosimeter of choice for determination of absorbed dose in comparison to its counterparts, the diode and film. Both the diode and film show an over response to low energy photons. The TLD and film are integrating dosimeters while the diode is an electrical conducting dose rate dosimeter. Due to the TLDs small size and its tissue equivalency, it can be placed almost anywhere within the body and can be used to determine absorbed dose quickly. Because of its chemical composition, film is not tissue equivalent and due to its energy dependence it should not be used to measure absorbed dose directly. It has been shown that diode sensitivity is affected not only by photon energy but also by temperature changes and radiation history (Ricker et al., 1987). Therefore, it should not be used for absolute dosimetry.

The diode used in this experiment was specially built by Bo Anderson of CRS, Inc. The diode was a standard store bought photodiode

housed within a cylindrical aluminum case. The diode was selected so that its response closely resembles that of a 0.3 cc standard cavity ionization chamber. However, the diode still retains the important advantage necessary for resolving the cross profiles of small beams that ionization chambers are not capable of. Because of the gain adjustment limitations of the CRS electrometer, the commercially available diodes could not be used.

The thermoluminescent dosimeters used in this experiment were purchased from Harshaw Chemical Company and are made of natural lithium fluoride duped with magnesium. The TLD-100 rods are one millimeter by one millimeter by six millimeters in length (control number T-2618-S-1). The TLDs were used to corroborate the ion chamber calibration value for each secondary collimator cone, field dependence in air, and phantom.

Film is an important tool in radiation therapy because large amounts of useful information can be derived from a single sheet. The data derived from film is permanently recorded so future data determination is possible. In this study, Kodak XV-2 X-Omat ready pak (LOT 122-17-71) was used to corroborate the diode cross profile determination, symmetry, flatness, beam diameter at the 50% and 90% isodose lines, and penumbra for each secondary collimator cone. The XV-2 film dose response curve shows a linear relationship through 40 cGy with film saturation occurring around 100 cGy. The film was automatically processed by the Kodak X-OMAT rapid processor.

E. Keithley 602 Mod and 614 Electrometer

The Keithley 602 and 614 are solid state operational-amplifiers which have been modified to give an adjustable +/-150 and +/-300 volt high voltage source that can be used to bias either the chamber collector or chamber wall. The Keithley 602 Mod replaced the analog readout with a digital readout and also has a built-in battery to supply the high voltage (HV) to the chamber. Both electrometers provide a variety of ranges of charge measurements by means of several built-in input capacitors.

The Keithley 614 (SN 312275) was utilized along with the 0.6cc PTW chamber (#433) to determine the halve value layer (HVL) for various field sizes and each of the secondary collimator cones. The Keithley 602 Mod and PTW Markus Parallel Plate Chamber were utilized to determine the fractional depth dose (FDD), tissue maximum ratio (TMR), field size dependence in water (FSDw), field size dependence in air (FSDa) and accelerator calibration utilizing the TG-21 protocol. The Keithley 602 Mod was also matched with the 0.6cc PTW calibration chamber (#768) to confirm the markus chamber calibration.

F. Phantoms

1. Full scatter phantoms:

   a. Clear polystyrene phantom (density 1.046 g/cc) dimensions 25x25x20cm

   b. Clear polystyrene irradiation phantom for TLD rods (density 1.046 g/cc) with dimensions of 25x25x0.5cm

   c. High impact (white) polystyrene phantom (density 1.054 g/cc) dimensions of 25x25x30cm

d. Med Tech water phantom with dimensions of 32x38x38cm

e. Water phantom with high impact polystyrene bottom dimensions of 30x30x20cm

f. Alderson head phantom constructed by Radiology Support and Devices, Inc.. The head phantom consisted of 9 axial slices 2.5cm thick with 5mm x 5mm grid pattern with 1.42mm diameter holes drilled throughout the simulated brain and neck area. The head phantom is constructed of simulated tissue material surrounding a human skull (Figures 3a,b).

g. Bees wax head phantom constructed from a mold taken from the Alderson phantom (Figure 4).

Acceptance testing of the Alderson head phantom consisted of a lateral and anterior radiographic projection to confirm the position of the bone material within the simulated tissue material. The bees wax head phantom was constructed to match the dimensions of the Alderson head phantom. The wax head phantom was cut in the coronal and sagittal direction for use in film determination of isodensity curves. The water phantoms were used in the manual determination of fractional depth dose, tissue maximum ratios, field dependence in water, and peak scatter factor for 10x10cm field size. The polystyrene phantoms were used in film and TLD experiments.

2. Miniphantoms:

a. High impact polystyrene disk (density 1.054)
b. Acrylic buildup cap (density 1.17)
c. Superflab disk (density 1.02)
d. Brass cap (density 8.4 g/cc)

The miniphantoms were used in the determination of field dependence in air and peak scatter factors.

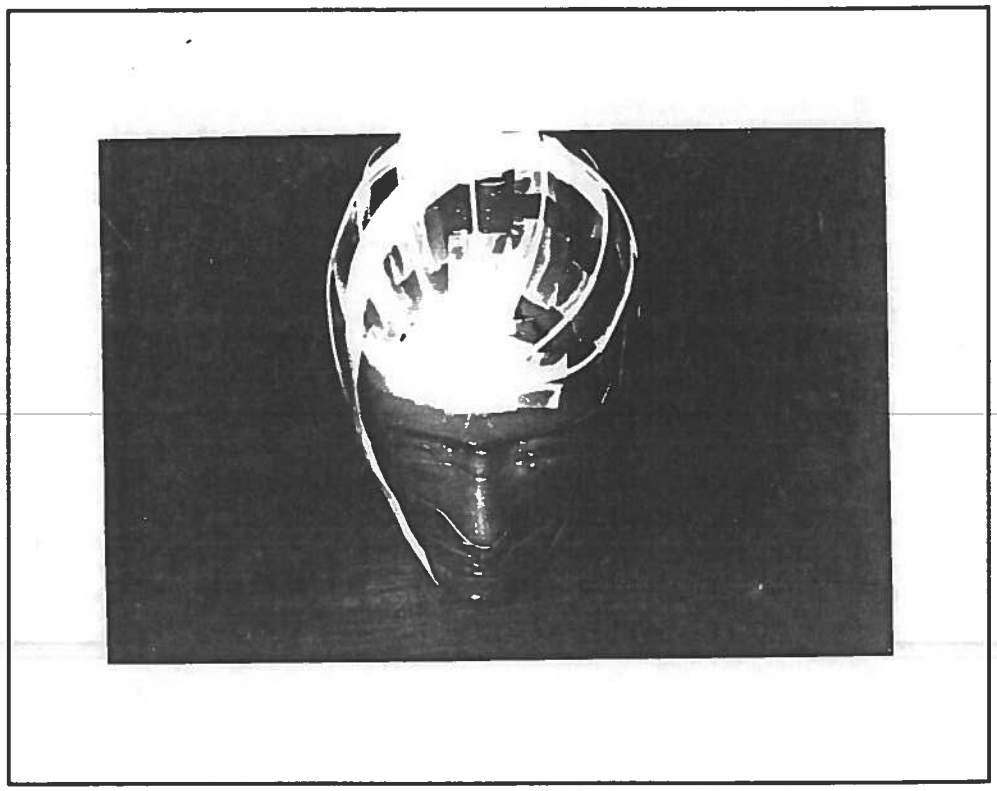

Figure 3a Front view of the Alderson head phantom with the catheters depicting the arc paths followed by the beam with the intersection of these paths at the AP setup mark.

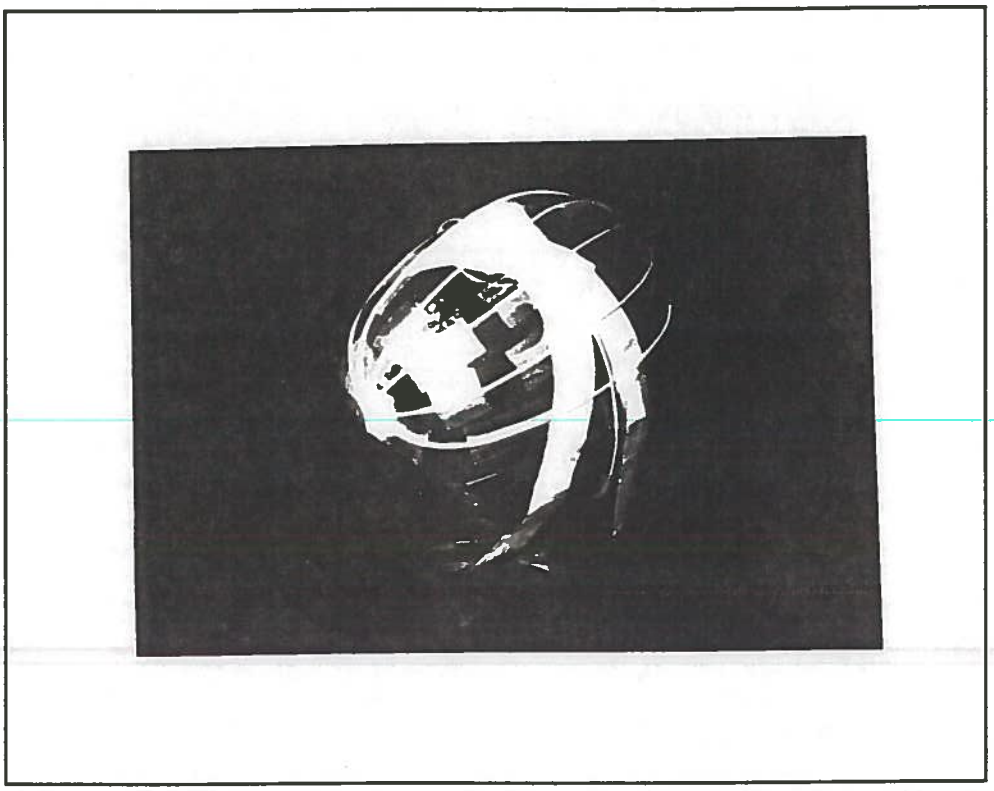

Figure 3b Left oblique view of the Alderson head phantom showing the use of catheters to designate the arc paths being followed and also the setup laser lines in the axial, coronal, and sagittal planes.

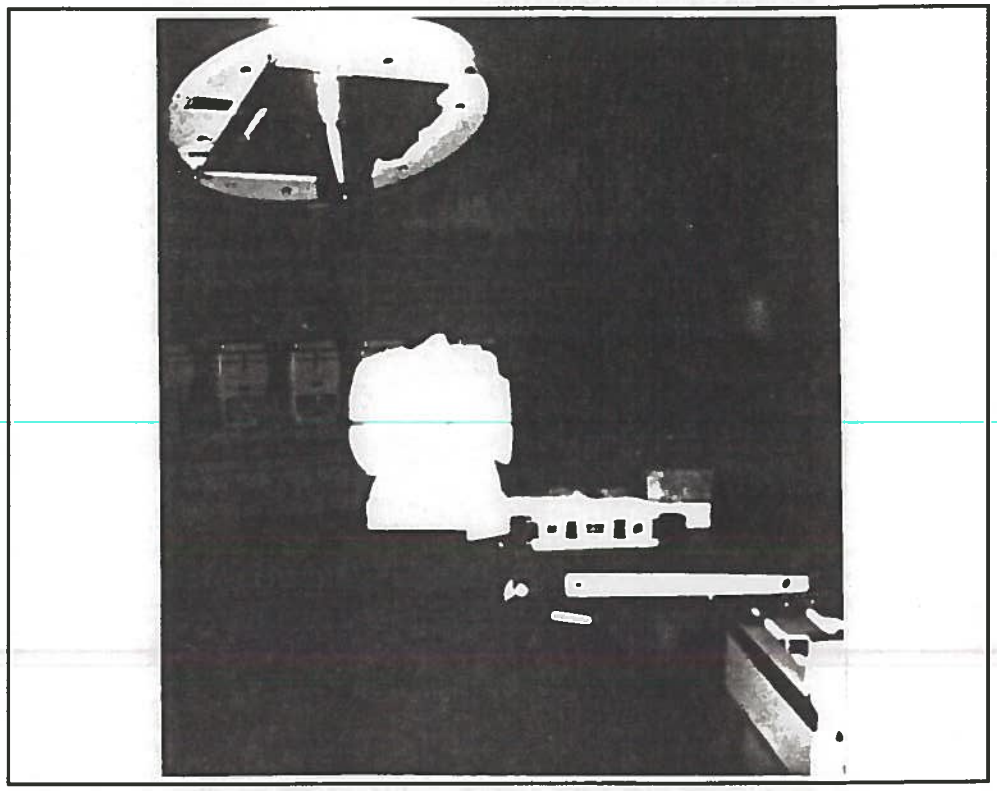

Figure 4 Wax replicate of the Alderson head phantom sliced for coronal placement of film. Phantom was also sliced for sagittal placement of flim.

EXPERIMENTAL METHODS

A. Beam Profiles

The cross profiles for cone 1, cone 2, and cone 3 were determined using both film and diode detectors. The Artronix model 3307 scanning isodensitometer was utilized in the determination of the cross profiles using film as the detector. The diode detector built by Bo Anderson and the CRS data acquisition system were also used in the acquisition of the cross profiles (Figure 5). The setup used to obtain the cross profiles when the film was placed perpendicular to the beam central axis involved placing the film at 102.8cm from the source with the addition of 2.8cm of clear polystyrene as buildup, therefore placing the isocenter at the surface of the polystyrene phantom (Figure 6). The setup used for film placement parallel to the beam central axis was to place the isocenter on the surface of the high impact polystyrene phantom. The film was placed between the sheets of the polystyrene which was parallel to the beam. The edge of the film was level with the surface of the phantom and excess paper wrapper folded over and taped to the phantom (Figure 7). All of the experimental setups involved the use of Kodak XV-2 X-OMAT ready pak Lot # 122-17-71 film and the clear polystyrene phantom. Due to the Artronix's analog output to an x-y plotter the flatness, symmetry, and penumbra had to be measured by manual methods.

The flatness describes the variation in intensity over the central eighty percent of the beam as defined at full width at half maximum. The beam symmetry is defined as the difference in the left half intensity and right half intensity over the central eighty percent as

defined at full width at half maximum if the beam profile was folded in half along the central axis. The flatness was determined by taking the average maximum and minimum beam intensity determined over the central eighty percent of the full width at half maximum dimension. The determination of the beam symmetry was done by dividing the field in half giving left and right side intensities defined at the same position as for beam flatness. The symmetry is determined by taking the average beam intensity of the left half and the right half over the central 80% of the beam, then subtracting these value and dividing the sum by left half plus the right half and multiplying by 2 and 100%. The penumbra width is the distance measure of the rate of dose fall off specified between two intensity points. The penumbra width is determined for the 90/10% and 80/20% separation for each of the cones.

The CRS system and diode detector were utilized in the determination of the cross profiles, but only scans perpendicular to the beam central axis were able to be done. The same information determined from the film is also determined from the CRS supplied data (flatness, symmetry, and penumbra) for each cone. It was found that the methods used to determine the flatness and symmetry were not accurate therefore, manual determination was done as described above. The software program used in the CRS system determines the penumbra width for the 80/40% isodose lines, whereas the 90/10% and 80/20% differences are needed. Cross profiles for both the CRS system and film were taken at 2.8cm, 5cm, 7.5cm, 10cm, and 20cm depths and normalized to maximum reading.

The beam width at 90% and 50% were determined for each of the clinical cones from the cross profiles taken at 2.8cm depth for each

experimental method. Cone 1, cone 2, and cone 3's defined beam diameter for clinical purposes will be the 90% isodose line defined at isocenter. For comparison between the clinical cones and the primary collimator field sizes, equivalent fields have to be determined and are defined at the 50% isodose lines at isocenter.

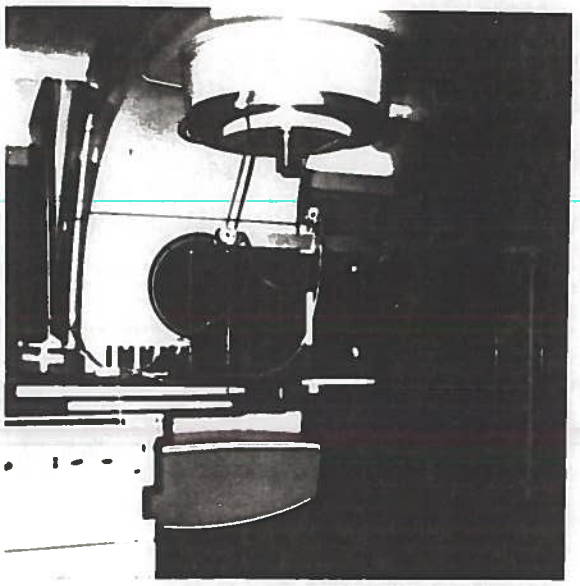

Figure 5 Cross profiles setup using the CRS system with the diode detector. The surface of the water is at 100cm SSD with the diode scanning at multiple depths.

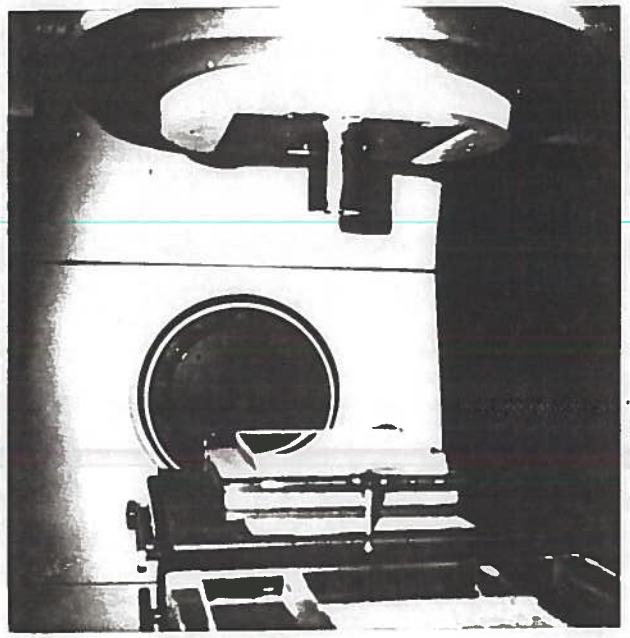

Figure 6 Cross profile setup for clinical cones ith film placed at 102.8cm with 2.8cm of buildup (polystyrene) with film placed perpendicular to the beam.

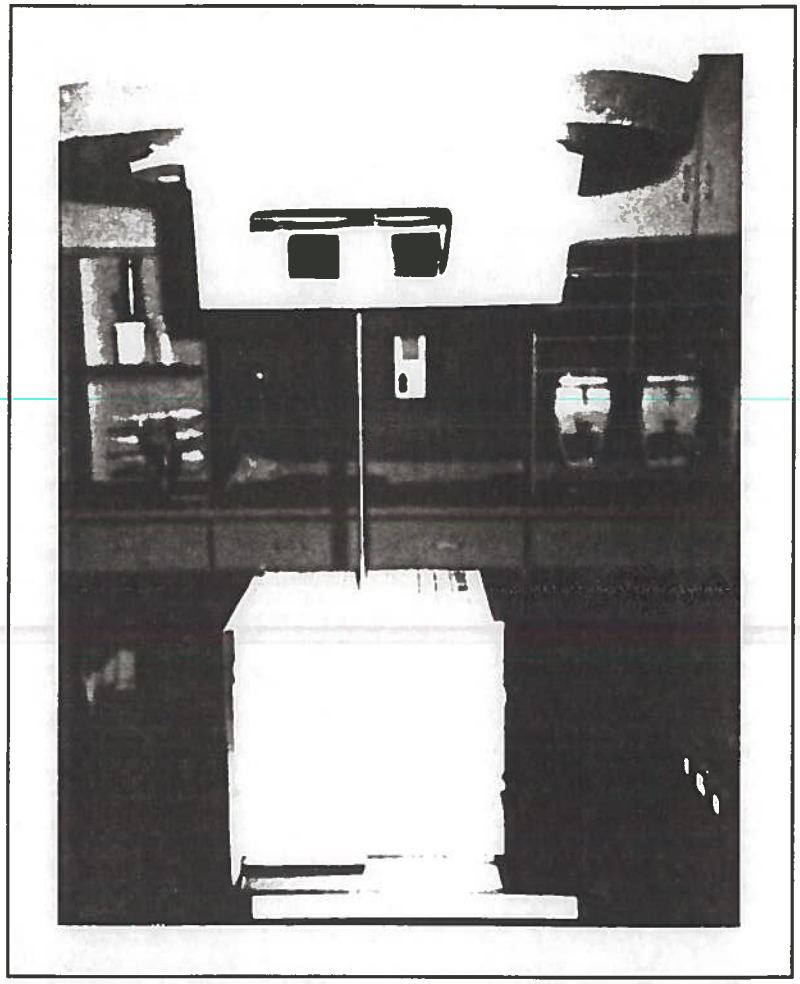

Figure 7 Cross profile setup for film placed parallel to beam central axis with top of phantom placed at 100cm SSD.

B. Thermoluminescent and Film Dosimetry

The conversion of TLD reading in microcoulombs (μC) or film optical density (O.D.) reading, to absorbed dose is accomplished by experimentally determining the dose response curves by exposing the TLDs or film to known doses of radiation.

A correction factor is first determined for each TLD rod by irradiating a population of TLDs rods to the same dose (100 cGy) and under the same conditions. The purpose of the correction factor is to correct each TLD rod reading so that all the TLD rods from the same population can be compared to each other. The conversion of the corrected TLD reading to absorbed dose is accomplished by exposing a different group of rods to a known dose of radiation and from the corrected readings determine a dose response curve. The dose response curve generated is good only for that population of TLD rods. A control set of TLDs must be irradiated with each experiment to account for variations in the TLD reader. The TLDs are placed in individual slots within a 25x25x0.5cm clear polystyrene plate. The TLD phantom holds 50 TLD rods spaced 1cm apart center to center. The irradiation phantom is placed on top of the 25x25x15cm clear polystyrene phantom with a 2.7cm clear polystyrene sheet placed on top of the TLD irradiation phantom. The surface of the complete phantom is placed 100cm from the radiation source. In determining the sensitivity correction factor for each TLD rod, the collimator field size was set at 25x25cm so that 50 TLDs could be irradiated at once. For the other experiments the collimator field size was set at 10x10cm.

The dose to individual TLDs:

$$Dose_{TLD}(cGy) = MU * FDD(s,d,f) * CR * OF(s) \qquad (1.)$$

where MU is the monitor units used, FDD(s,d,f) is the fractional depth dose (at 2.8cm depth is 1.00), CR is the constancy ratio (which is the ratio of variation from 1 cGy/mu for a 10x10cm field size at 2.8cm depth) and OF(s) is the output factor or field dependence in phantom (OF(25)= 1.092 and OF(10)= 1.000), s is the side of the equivalent square, d is the depth, and f is source to surface distance.

Dose determination from film is not recommended for photons due to the energy dependence of the film. Film shows a high energy absorbance for low energy photons around a 150 to 200 KeV (thousands of electron volts) range due to the photoelectric effect which is predominate at these energy ranges (Williamson et al., 1981). Since the high energy photons used in radiation therapy have an increasingly low energy scatter component with depth, the degree of film blacking (optical density) which is used to determine the dose can be misleading. Film can be useful for relative work such as the determination of flatness, symmetry, and beam penumbra width. It has also been reported that film can be used in the determination of isodose curves for high energy accelerator with an acceptable accuracy (+/-3%) (Williamson et al., 1981). The determination of multiple depth dose response curves or sensitometric curves for 2.8cm and 10cm depths were carried out to determine the effect of the low energy scatter components on dose determination from film. If the low energy scatter component causes a significant variation in the optical density, a difference in the 2.8cm and 10cm depth dose response curves would be evident and if no variation

exist the curves should be the same.

The determination of the absorbed dose versus optical density was carried out using Kodak XV-2 film Lot # 122-17-71 cut into strips and read by the Macbeth TD-504 manual densitometer. The Macbeth manual densitometer has to be calibrated each time it is turned on and should be periodically calibrated during use to check for drift. The calibration method uses the Kodak calibration step strip (No. 706 ST121) to manually adjust, if necessary, the optical density reading to correspond to the optical density assigned to each area of the calibration strip.

The film strips were placed on top of the 25x25x15cm clear polystyrene phantom (leveled) and 2.8cm and also 10cm of clear polystyrene was placed on top of the phantom and film. A 100cm source to surface of phantom distance with a collimator setting of 10x10cm was used. Each strip of film was given a set monitor unit count ranging from 0 (background) to 110 units. The dose to the film was calculated by:

$$Dose_{FILM}(cGy) = MU * FDD(s,d,f) * CR * OF(s) \qquad (2.)$$

where MU is the monitor units given, FDD(s,d,f) is the fractional depth dose (at 2.8cm depth FDD is 1.00 and 10cm depth FDD is .724), other factors as defined in equation 1. Once the optical density was determined for each piece of film, the background reading was subtracted from each reading to give the net optical density. The optical density readings were then plotted versus dose to give the dose response curve for that lot of film only.

C. Half Value Layer (HVL) and Linear Attenuation Coefficient (μ)

Beam attenuation in water was investigated to determine the narrow beam linear attenuation coefficients for each secondary cone and primary field sizes ranging from 4x4cm to 8x8cm. From the graph of the attenuation coefficient versus field size, the zero-area linear attenuation coefficient was determined by extrapolation and also by determining the slope of the equation that describes the linear attenuation versus field size curve.

The zero-area attenuation coefficient (μ_o) will be used in the determination of the zero-area FDD and TMR. Also investigated was the effect, if any, the secondary cones had on the beam quality by determination of the first half value layer in water following the equation:

$$HVL = \frac{Ln\ 2}{\mu_o} \qquad (3.)$$

also, the HVL was determined by direct interpolation from the beam attenuation curves for each field size.

The experimental method followed to determine the linear attenuation coefficient for each field size and the secondary collimator cones were as follows (Figure 8):

1. Place the outside bottom of the tank (phantom with the high impact polystyrene bottom) at 100cm from the radiation source.
2. Place the 0.6cc PTW chamber in the clear polystyrene phantom at 202.8cm (source to center of chamber distance).
3. Add water to the tank. Take reading for the following levels of 6cm, 10cm, 14cm, 18cm and 20cm using fields that range from 4x4cm to 8x8cm and the secondary collimator cones.

The readings were plotted versus water equivalent depth for each field size. The slope of these curves yields the attenuation

coefficient for that field size. By plotting the attenuation coefficients versus field size, the zero-area attenuation coefficient can be determined by extrapolation. Under ideal conditions where only the primary beam is measured, the beam attenuation curve will be exponential and will be field size independent. Under experimental conditions a different set of curves is obtained.

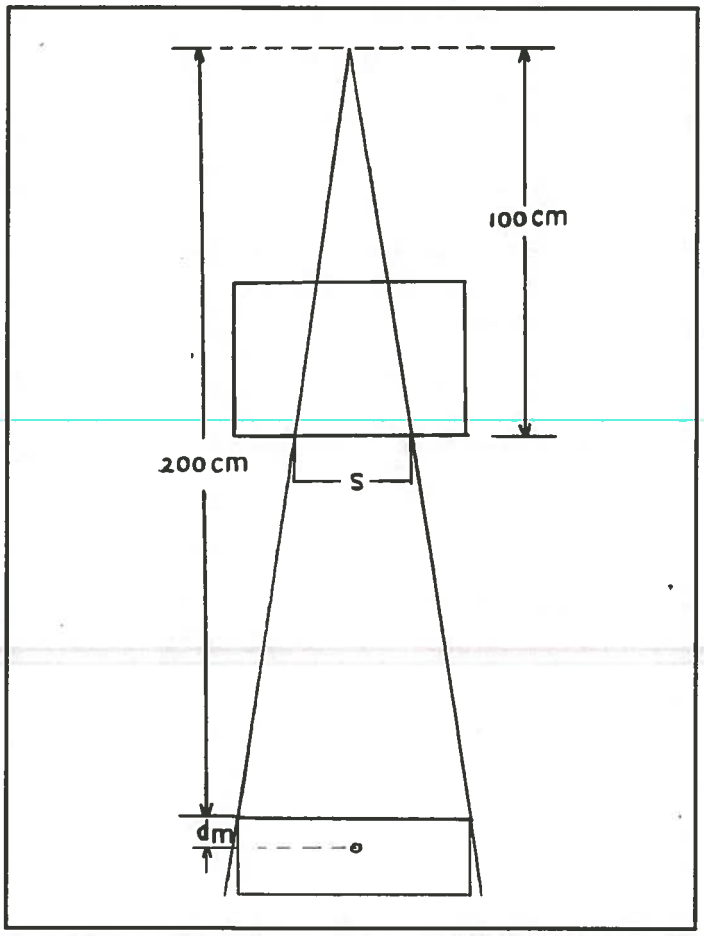

Figure 8 Setup used for determination of attenuation in water under conditions of good geometry.

D. Central Axis Depth Dose (FDD)

The central axis depth dose measurements were carried out using the 0.6cc PTW chamber, PTW/Markus chamber and diode detector in the Med Tech water phantom, and CRS data acquisition system. The central axis depth dose is determined from the ratio of the dose at depth and the dose at the reference depth according to the formula (Figure 9):

$$FDD(s,d,f) = \frac{D(d)}{D(d_m)} = \frac{M(d)}{M(d_m)} \qquad (4.)$$

where $M(d)$ and $M(d_m)$ are the electrometer corrected readings corrected for temperture and pressure.

The FDD measurements made with the CRS system required the calibration of the CRS system to determine the water surface and depth of maximum reading for a 10x10cm field size for each chamber and diode used. The source to surface distance (SSD) was set to 100cm with the depth of maximum dose being normalized to 2.8cm. The FDD was determined for field sizes ranging from 3x3cm to 10x10cm and the clinical cones using the various chambers and CRS system. The fractional depth dose (FDD) was verified using the Med Tech water phantom and Markus Parallel Plate chamber for each of the clinical cones, 5x5cm, and 10x10cm field sizes. The fractional depth dose (FDD) values determined with the CRS system and Markus Parallel Plate chamber were compared to the fractional depth dose (FDD) values used by Mary Bird Perkins Cancer Center (MBPCC) and also compared to the depth dose values determined with the 0.1cc PTW chamber and diode detector. The zero-area fractional depth dose (FDD) was determined by experimentally determining the narrow beam linear attenuation coefficient (μ_o) and calculating the FDD or zero-area

according to the formula:

$$FDD(0,d,f) = \exp^{-\mu_e * (d-d_m)} * \left(\frac{f+d_m}{f+d}\right)^2 \qquad (5.)$$

where f=SSD (100cm) and depth of maximum dose (d_m= 2.8cm).

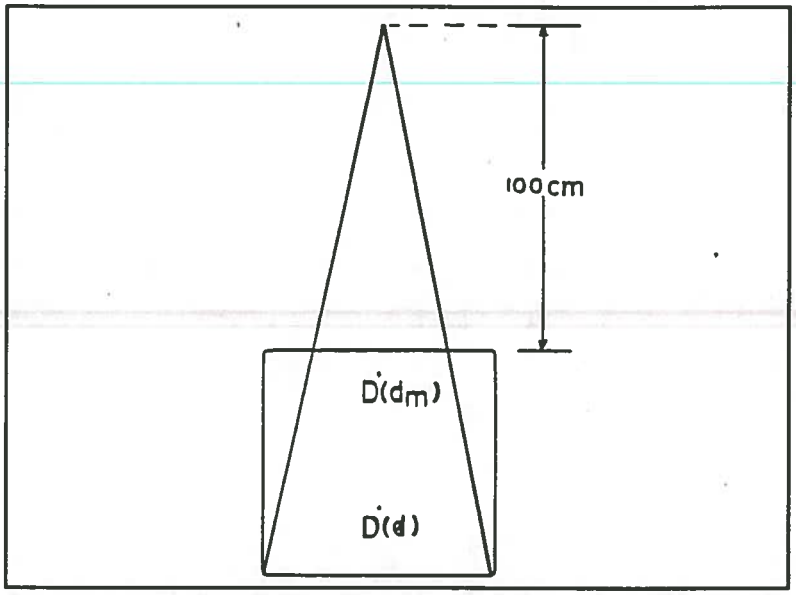

Figure 9 The fractional depth dose is defined by the equation FDD(s,d,SSD) = D(d)/D(dm) following the setup of 100cm SSD with dm = 2.8cm.

E. Scatter Correction Factors

The relationship between absorbed dose and the monitor unit for different field sizes was found to be a function of the primary and scatter dose (Arcovito et al., 1985, Houdek et al., 1985). Since the primary radiation beam is field size independent (Houdek et al., 1985) the relationship between absorbed dose and the monitor unit for different field sizes is solely dependent on the scatter dose correction. The total scatter correction is a function of the field size (collimator angle scatter) and the area of the phantom being irradiated (peak scatter factor).

The total scatter correction factor (S_t) or field size dependence in phantom (FSD_p) is defined as the ratio of the dose for the collimator field size of interest to that dose for the reference field size (10x10cm) measured at the depth of maximum dose in a full scatter medium (Figure 10). The measurements are carried out with the PTW/Markus chamber in the Med Tech water phantom at the depth of maximum dose (2.8cm) and with the source to phantom surface set at 100cm following the equation.

$$S_t(s) = FSD_p(s) = \frac{\bar{M}(s,d_m)}{\bar{M}(10,d_m)} \qquad (6.)$$

where $\bar{M}(s,d_m)$ and $\bar{M}(10,d_m)$ are the average electrometer readings. The same results are obtained with the chamber at the isocenter. The total scatter correction factor can be broken down into the collimator scatter correction factor and the phantom scatter correction factor.

The collimator scatter (S_c) or field size dependence in air (FSD_a) is a function of the primary collimator angle and also encompasses the

primary beam component. The collimator scatter is defined as the ratio of the dose in air at isocenter for the collimator field size of interest to that dose at isocenter for the reference field size (10x10cm) (Figure 11). The experiment was carried out using the 0.6cc PTW chamber with acrylic build-up cap, the PTW/Markus chamber with superflab, or high impact polystyrene as the build-up material. All experiments were carried out at isocenter (SAD=100cm) except when the light field did not cover the build-up material, an extended source to chamber distance (>200cm) was employed. Arcovito et al., 1985 and Houdek et al., 1983 have shown that the collimator scatter factor is independent of source to chamber distance. The equation to determine the collimator scatter is:

$$S_c(s) = FSD_a(s) = \frac{\bar{M}_c(s)}{\bar{M}_c(10)} \qquad (7.)$$

where $\bar{M}_c(s)$ and $\bar{M}_c(10)$ are the average corrected readings for the collimator field size of interest and the reference field size (10x10cm).

The final component of the total scatter correction factor is known as the normalized phantom scatter correction factor (S_p), but is also called the normalized peak scatter factor (NPSF(s)). The $S_p(s)$ takes into account the change in scatter that occurs within the phantom when the area irradiated is reduced due to secondary blocking as compared to an unblocked field. The $S_p(s)$ can be experimentally determined but it is easier to calculate from the field dependence in phantom (FSD_p) and field size dependence in air (FSD_a)

according to the equation:

$$S_p(s) = NPSF(s) = \frac{S_t(s)}{S_c(s)} = \frac{FSD_p(s)}{FSD_a(s)} \qquad (8.)$$

The peak scatter factor (PSF(s)) determined at depth of maximum dose is commonly known as tissue air ratio (TAR(s,d_m)) and also as backscatter factor (BSF). The peak scatter factor (PSF) for a 10x10cm field size was determined using the 0.6cc PTW chamber with the acrylic build-up cap and the PTW/Markus chamber with superflab, or high impact polystyrene as the build-up material. All experiments were carried out in the Med Tech water phantom. The experimental procedure followed calls for in water readings and in air readings. The waterproofed chambers were placed at the depth of maximum dose in water (2.8cm) and the isocenter was placed at the center of the chamber. While the chamber remained at isocenter, the water was drained off and the chamber was allowed to come to thermal equilibrium with air medium. The ratio of the readings corrected for temperature and pressure for the in water and in air measurements gives the peak scatter factor (PSF).

$$PSF(s) = \frac{\overline{M}_w(s)}{\overline{M}_a(s)} \quad , \quad NPSF(s) = \frac{PSF(s)}{PSF(10)} \qquad (9.)$$

where $\overline{M}_w(s)$ and $\overline{M}_a(s)$ are the average corrected electrometer readings in water and in air following the setup found in Figure 12.

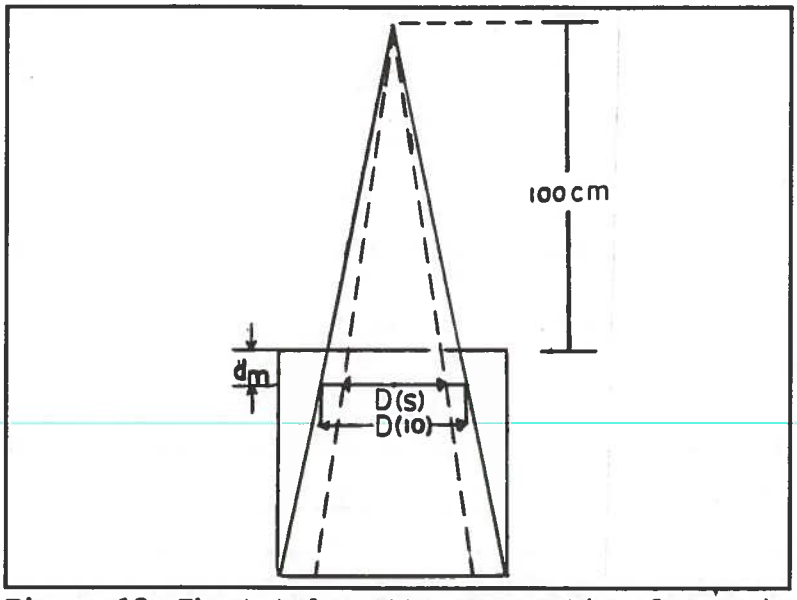

Figure 10 The total scatter correction factor is defined by the equation $S_t(s) = D(s)/D(10)$ following the setup above.

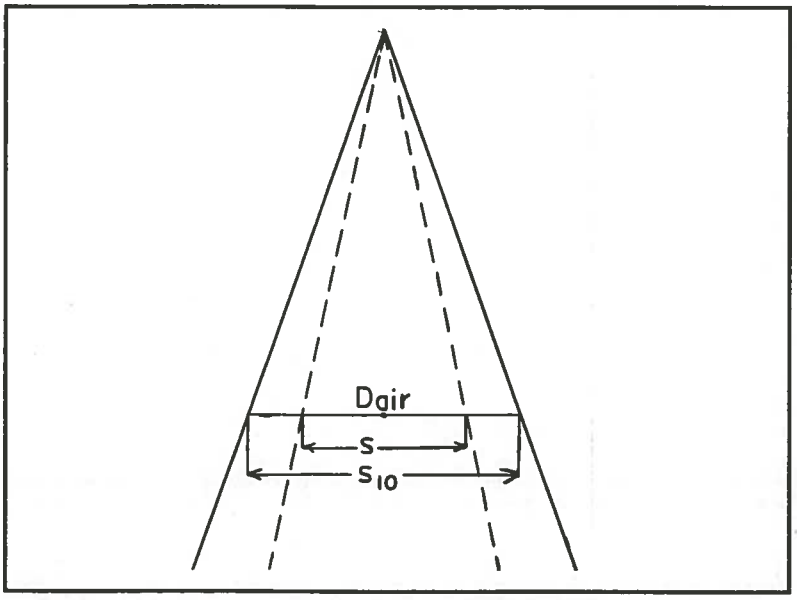

Figure 11 The field size dependence in air is determined from the equation $S_c(s) = D_{air}(s)/ D_{air}(s_{10})$ following the setup above.

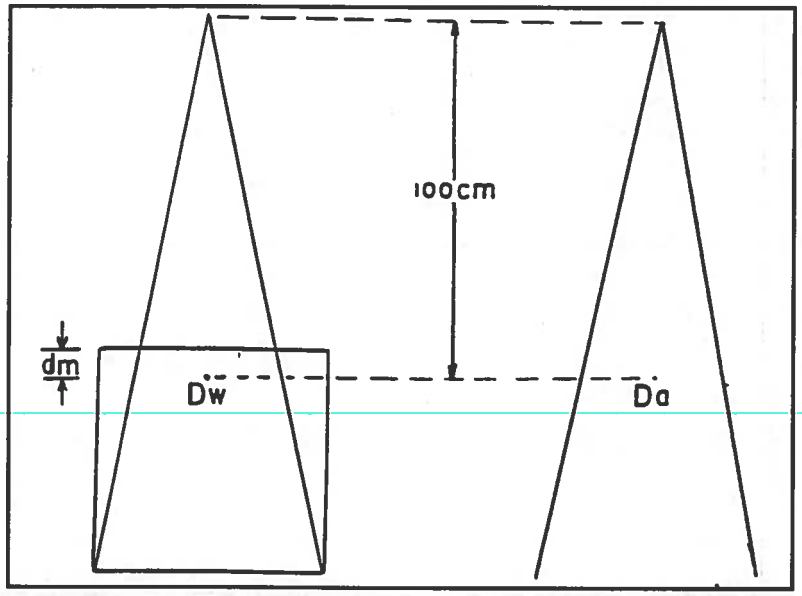

Figure 12 The peak scatter factor is analogous to the backscatter factor which is defined by the equation $PSF(s_{dm}) = D_{water}/D_{air}$ at depth of maximum dose in water.

F. Central Axis Tissue Maximum Ratio (TMR)

The central axis tissue maximum ratios were manually determined using the PTW/Markus Parallel Plate chamber and Med Tech water phantom. The reference depth for normalization was 2.8cm. For tissue maximum ratios (TMR) the reference depth is the depth of maximum dose or maximum electrometer reading. The experimental setup requires that both the chamber and phantom be moved simultaneously in order to increase the water depth but at the same time maintaining the same source to chamber distance. This simultaneous movement places the chamber and accelerator isocenter at the desired depth with the field size remaining constant at depth. The TMR is determined according to the equation:

$$TMR(s,d) = \frac{D(s,d)}{D(s,dm)} = \frac{\bar{M}(s,d)}{\bar{M}(s,dm)} \qquad (10.)$$

where $\bar{M}(s,d)$ and $\bar{M}(s,dm)$ are the average corrected readings at depth and the reference depth of maximum reading (Figure 13).

The TMR measurements were manually determined for each secondary collimator cone and the 5x5cm field size at 2.8cm, 5cm, 10cm, 15cm, and 20cm depths. The TMR values were also calculated from the FDD and the normalized peak scatter factors (NPSF) following the formula:

$$TMR(s_d,d) = PDD(s,d,f) * \left(\frac{f+d}{f+dm}\right)^2 * \frac{NPSF(s_{dm})}{NPSF(s_d)} \qquad (11.)$$

where f is the SSD (100 cm) and $NPSF(s_{dm})$ and $NPSF(s_d)$ are the normalized peak scatter factors for field size at depth of maximum dose and for field size at depth of interest.

The zero-area TMRs are a function of the linear attenuation coefficient (μ_s) determined for each field size by using an exponential

fit of the TMR data beyond 10cm depth and plotting these values versus field size. By extrapolating back to the zero-area field size the linear attenuation coefficient (μ_o) for the zero-area is determined. Another method to determine the zero-area TMRs is to use the effective linear attenuation coefficient derived from the half value layer experiment. By the following formula, the zero-area TMRs are calculated for both methods:

$$TMR(0,d) = \exp^{(-\mu_o * (d-d_m))} \qquad (12.)$$

where μ_o is the effective linear attenuation coefficient and d_m is the depth of maximum dose (2.8cm).

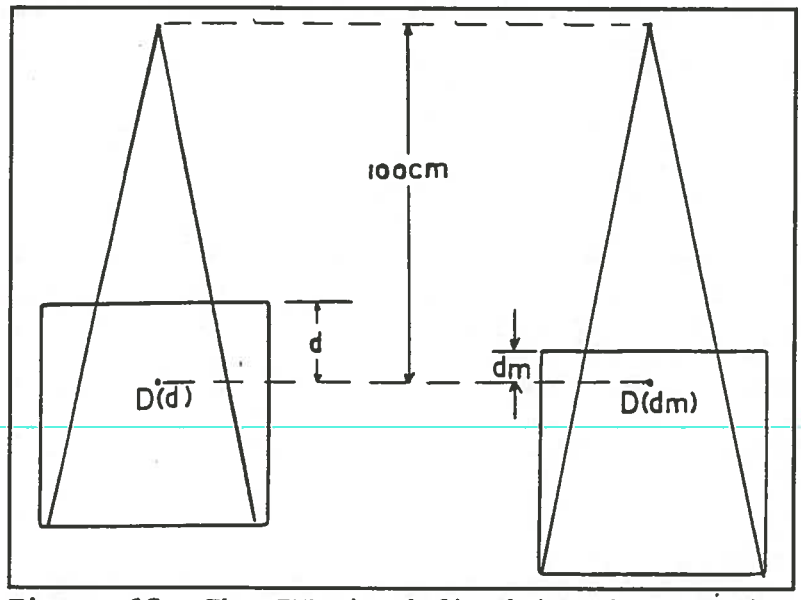

Figure 13 The TMR is defined by the equation TMR(s,d) = D(d)/D(dm) according to the experimental setup as seen above.

G. Isodensity and Isodose Curves

Irradiation Technique

The technique designed for this study was of a well collimated, small diameter beam field utilizing five non-coplanar rotational beams each directed towards the machine isocenter (target center within the patient), enabling a very high dose to be delivered to the target volume and high dose gradient outside the target volume (Figure 14 and 15). The technique was modified from numerous protocols found in the literature (Colombo et al., 1985, Hartmann et al., 1985, Lutz et al., 1988, Saunders et al., 1988).

The convergent beam irradiation technique consists of a combination of five arcs in such a way that each of these arcs are performed at different couch positions. The couch angle will follow either table 1 or table 2 below depending on the start angle (Figure 16).

Table angle:	Table 1	Table 2	
	90 deg	270 deg	start table angles
	120 deg	240 deg	
	150 deg	210 deg	
	210 deg	150 deg	
	240 deg	120 deg	

Each of the irradiations consist of a 120 degree arc rotation from 160 to 40 degrees for table angle of 210, 240, and 270 degrees or 200 to 320 degrees for table angles of 120 and 150 degrees. Since the center of the target volume must be placed at the machine isocenter it is critical that the axis of rotation of the gantry and the couch intersect the machine isocenter and remain stable throughout treatment (Figure 17). To ensure compliance, a strict quality assurance program must be implemented and a beam target verification system set up.

Because of the small diameter beams being studied and the lack of a three dimensional data acquisition system with appropriate detectors, the determination of the isodensity plots through the three major planes (axial, sagittal, and coronal) that passed through the beam central axis were setup utilizing the Alderson (axial only) and wax head (sagittal and coronal only) phantoms with film placed along the plane of interest.

TLDs were utilized in determining the isodose plots through the axial plane only, due to the design of the Alderson head phantom. A comparison in isodensity/isodose plots were made between film and TLD in the axial plane. The Capintec RT110 treatment planning computer was utilized to generate a isodose plan for a single 120 degree arc. It was used to compare to the isodensity/isodose plots experimentally determined for a single 120 degree arc in the axial plane for both film and TLD (Figure 18).

The setup used for the Alderson and wax head phantoms for isodensity/isodose experiments was to place the phantoms on a table extension on the treatment table and place the phantoms in the treatment position as set by the laser marks put on each phantom in simulation. The anterior (AP) setup SSD was set to 90cm (three millimeters cephalad to the slice two/three interface for the Alderson phantom) to the surface of the aquaplast with the sagittal laser mark drawn through the sagittal midplane of each phantom (Figures 19a,b and Figure 4). Fifty four (54) TLDs were used to create a eight spoke star pattern in the axial plane of slice two of the Alderson phantom with the central TLD to be placed at isocenter (TAD 100cm). The number of monitor units given per arc was calculated to deliver approximately 200 cGy total dose to

the central TLD for all arc rotations. The average TMR was determined by determining the average depth through the sagittal midplane to isocenter and using the 4x4cm field size. The calculated number of monitor units (mu) to give 200 cGy to isocenter was divided by the number of arcs to give monitor units per arc (mu/arc). The monitor units per arc was used for each of the five 120 degree arcs which was divided by the arc angle to give the monitor units per degree of rotation (mu/deg).

Determination of the isodensity plots in the major central planes by film dosimetry methods was accomplished by cutting out the film to the shapes of the phantom through the plane of interest (sagittal, coronal, and axial). Then placing the sheet of film between the two phantom halves and securely taping the phantom together to expel any air pockets in the XV-2 ready pak film. The phantoms setup was the same for the TLD experiments. The total dose to the film was limited to around 90 cGy to prevent film saturation. Film dosimetry followed the dosimetry methods utilized for the TLD experiments.

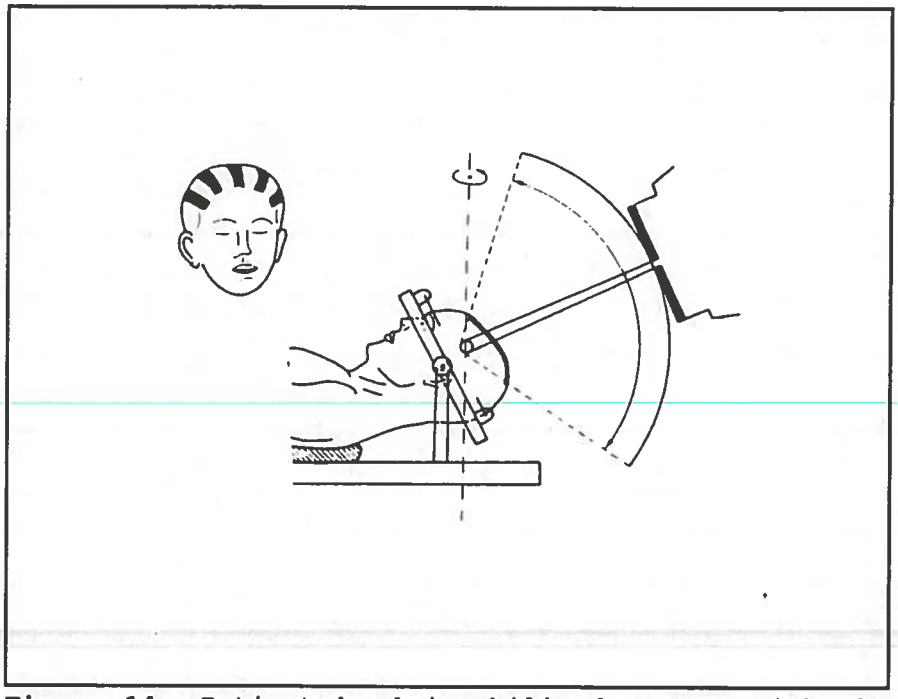

Figure 14 Patient head immobilized on PSA with the target at isocenter. Each of the arc treatments rotates around the PSA vertical axis. (Colombo et al., 1985)

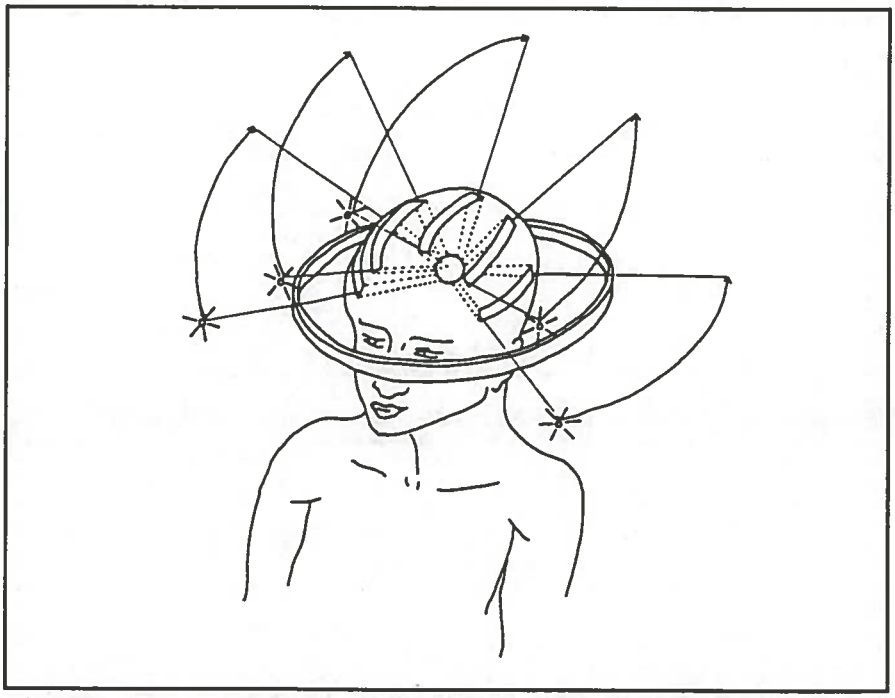

Figure 15 Illustration of the five arc coverage of the upper hemisphere of the skull with the non-coplanar beams intercepting at the isocenter. (Chierego et al., 1988)

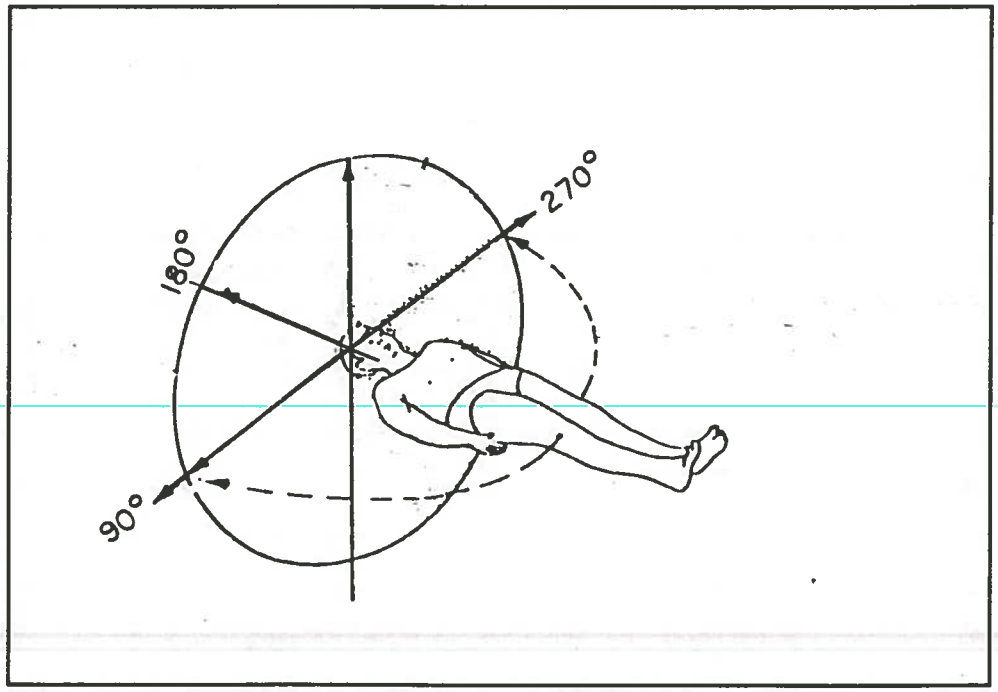

Figure 16 Diagram of patient in reference to treatment table angles for each of the five arc angles.

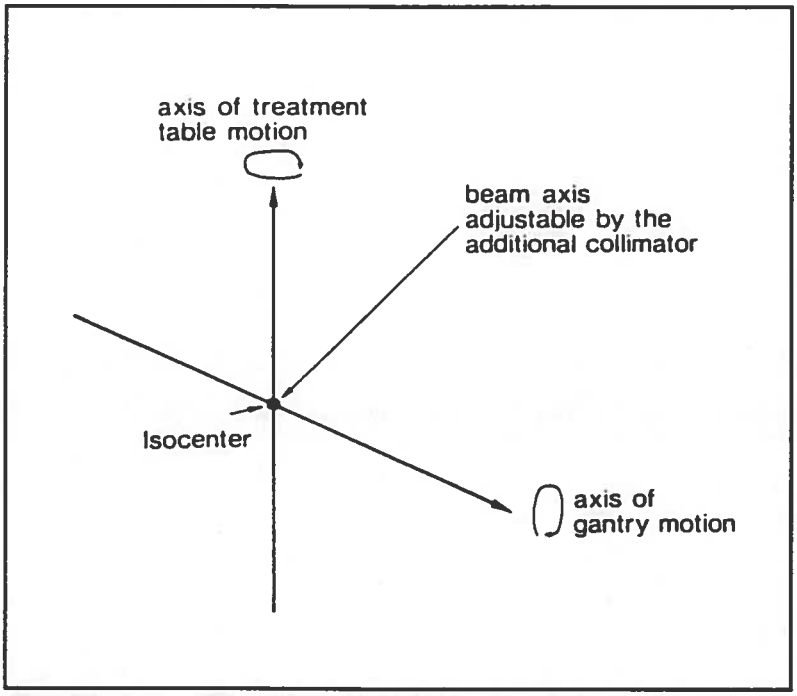

Figure 17 The requirements for axis alignment between the gantry and PSA. (Hartmann et al., 1985)

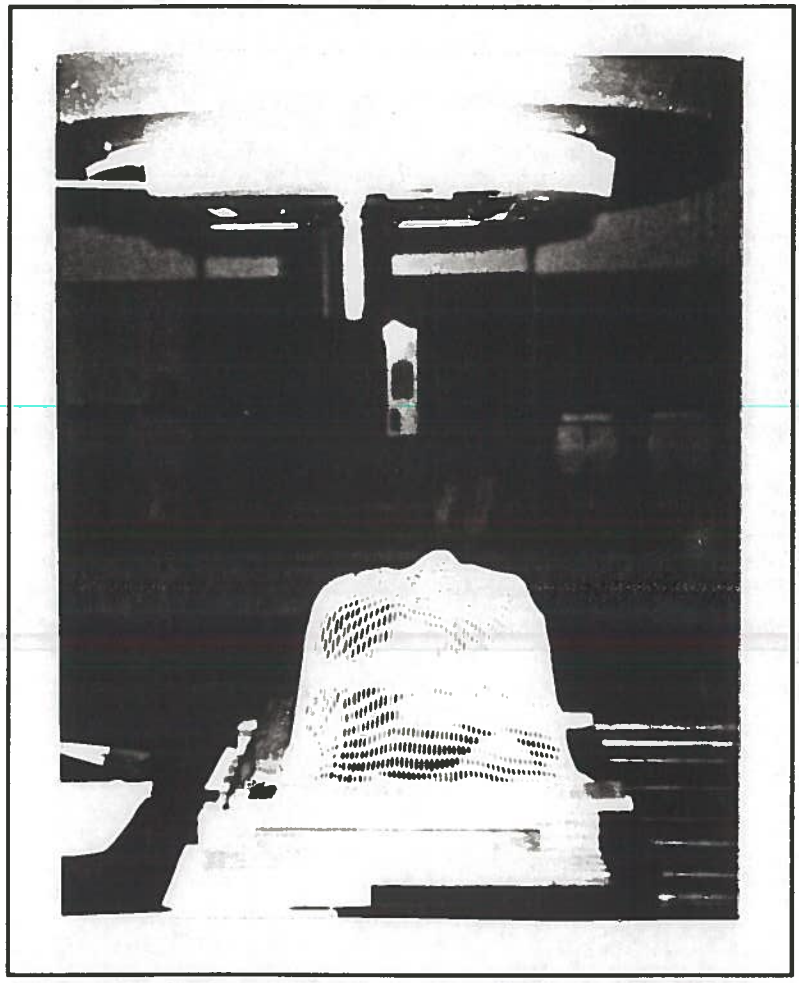

Figure 18 The Alderson head phantom placed in a Aquaplast head holder for a single 140 degree arc treatment using film and TLD's to compare to Capintec RT110 for cone 1.

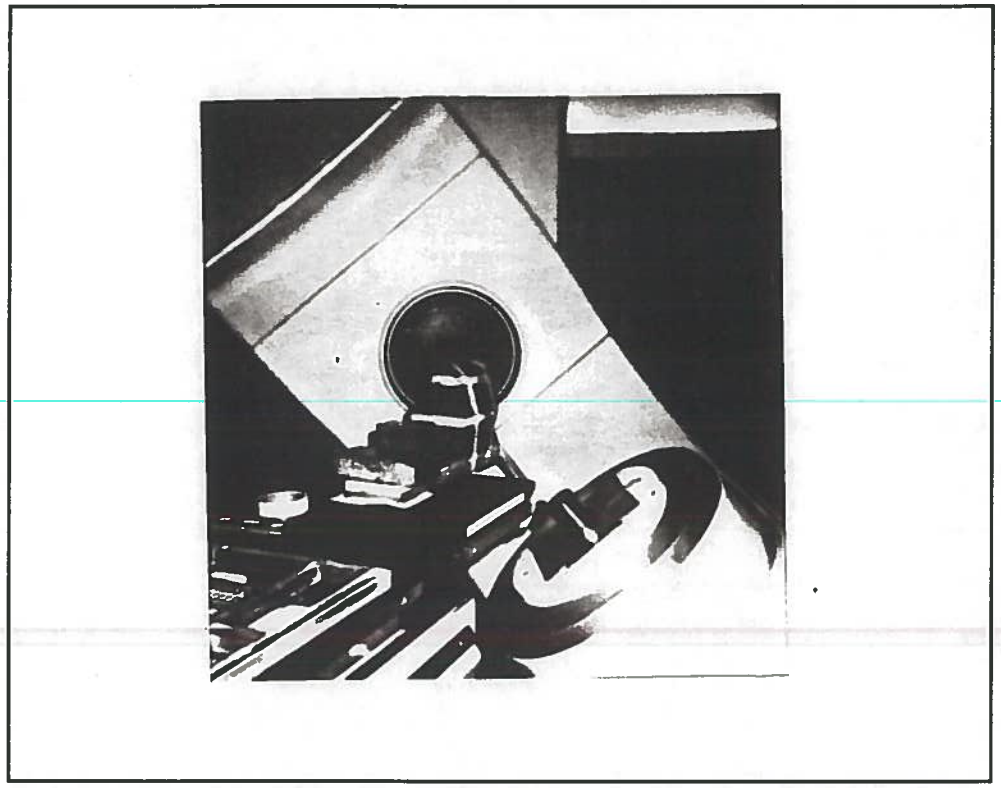

Figure 19a The Alderson head phantom setup for both film and TLD's for axial determination of isodensity/isodose plots for the five 120 degree arc treatments.

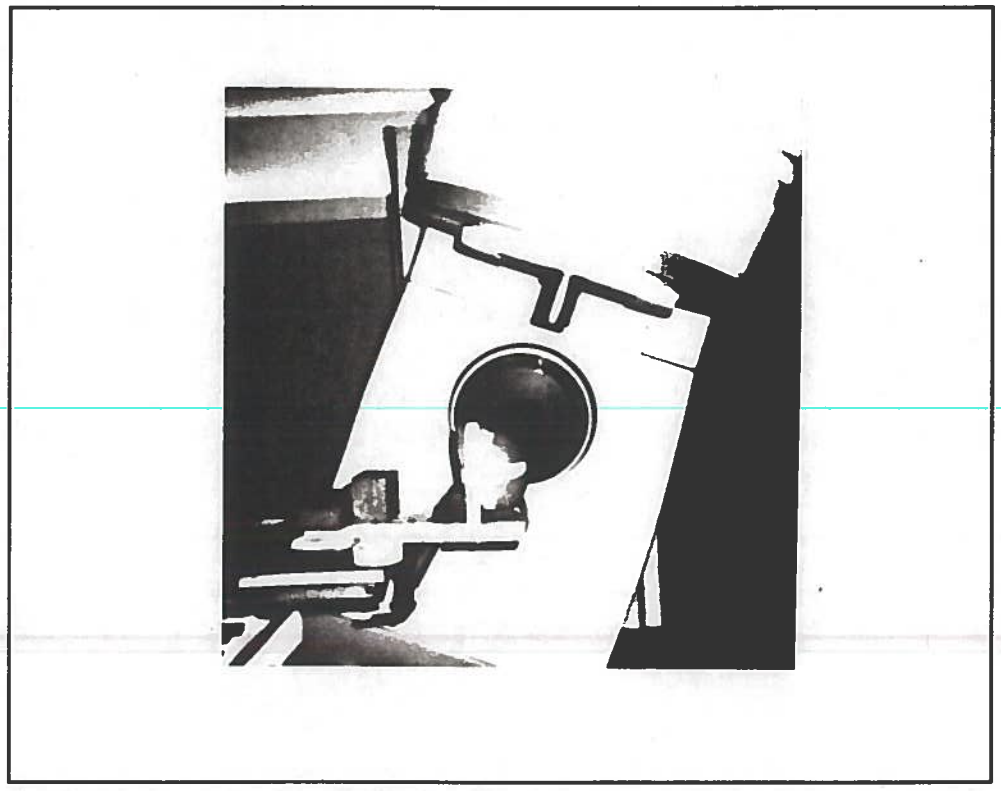

Figure 19b Wax head phantom cut for sagittal determination of isodensity curves for the five 120 degree arc treatments.

H. Quality Assurance

Because of the small fields being used, it was critical that a strict quality assurance program be maintained to ensure accurate data taking. The areas followed:

1. Accelerator calibration and output consistency.
2. Optical distance indicator (ODI) versus mechanical distance indicator.
3. Field sizes between 2x2cm and 10x10cm by ruler measurement versus digital readout.
4. Gantry rotation (level versus digital).
5. X-hair rotation.
6. Treatment table rotation.
7. Isocenter tolerance-difference in the point of rotation of the gantry versus the point of rotation of the table.

During experimental sessions where in water and in air measurements were taken, the ionization chamber was allowed to sit for thirty minutes before data was taken to allow for thermal equilibrium to occur between chamber and surrounding medium. Temperature and pressure readings were always recorded during each experiment to determine if a correction was needed for a change in the temperature and/or pressure. Chamber and electrometer leakage was checked before each experiment to prevent erroneous data from being taken. The chamber was always operated at a nominal bias voltage of -300 volts. Gantry angle and target to surface distances (TSD) as well as target to chamber distances were checked using a level and mechanical distance indicator before each experiment to ensure experimental reproducibility.

RESULTS AND DISCUSSION

A. Beam Profiles

The determination of beam symmetry and flatness by film for each cone showed that the crossprofiles were found to be symmetrical around the central axis and the degree of unflatness of the beam ranged from 5% for cones 2 and 3 to 10% for cone 1. The manufacturers specified diameter for each cone at the 90% ionization point at isocenter is 2cm, 3cm, and 4cm referenced from previous experiments done for the manufacturer in-air using a diode with buildup cap of sufficient thickness to establish electronic equilibrium.

The crossprofiles comparing parallel versus perpendicular placement of the film for both inplane and crossplane measurements (Figures. 20a,c) were found to show no significant variation in the results between setups. The beam diameters defined for the 90% and 50% isodensity point taken at 2.8cm depth at 100cm SSD in phantom and referenced to isocenter are found in table 1. The diode crossprofile measurements made at various depths for each cone and referenced to maximum reading gave comparable spatial results to the parallel placed film under the same experimental setup; however, a noticeable shift between the isodensity and isodose curves is seen due to the overresponse of the film to low energy scatter photon at depth (Figures 21a,c). The resulting diode and film diameter measurements referenced to isocenter in full phantom gave 1.5 +/-0.1cm for cone 1, 2.8 +/-0.1cm for cone 2, and 3.5 +/-0.2cm for cone 3 at the 90% ionization point while at the 50% ionization point the diameters were 2.0 +/-0.1cm, 3.5

+/-0.1cm, 4.3 +/-0.1cm respectively. The effective square determined from the British Journal of Radiology supplement 11 and Van Dyk's paper for each cone referenced to the 50% ionization point is 1.8cm^2, 3.15cm^2, and 3.85cm^2 for cone 1, cone 2, and cone 3 (Cohen et al., 1972, Van Dyk, 1972). As seen from the experimental results the manufacturers stated cone diameters were not found to be 2cm, 3cm, and 4cm at the 90% ionization points but measured 1.5 +/- 0.1cm, 2.8 +/- 0.1cm, and 3.5 +/- 0.2cm.

The in-air crossprofile measurements using the diode referenced to isocenter but measured at 102.8cm and 110cm source chamber distance (SCD) yielded results of 1.6 +/-0.01cm, 3.1 +/-0.01cm, and 3.9 +/-0.02cm for the 90% ionization points and 2.0 +/-0.00cm, 3.5 +/-0.00cm, and 4.3 +/-0.00cm for the 50% ionization points. The in-air diode profiles show a broader curve across the central region in relation to the in-phantom results (Table 2).

The penumbra widths defined at the 80/20% and 90/10% isodensity points measured in-phantom for diode and film detectors is corroborated by the values seen by Dawson et al., 1986 for 6 MV and 31 MV photons (Table 3). The resulting decrease in penumbra width with a decrease in beam diameter as seen in Table 3 is predicted by Arcovita et al., 1985 due to the decrease in the scatter component. The penumbra width determined from the in-air cross profiles is also corroborated by results seen by Dawson et al., 1984 with the penumbra width being defined by the primary radiation, collimator scatter, and the cone transmission while the penumbra width determined from the in-phantom measurements, an added scatter component from the phantom is present.

This added scatter will tend to drive the penumbra outward and therefore explain the difference in penumbra width between the in-air diode and in-phantom diode measurements (Table 4).

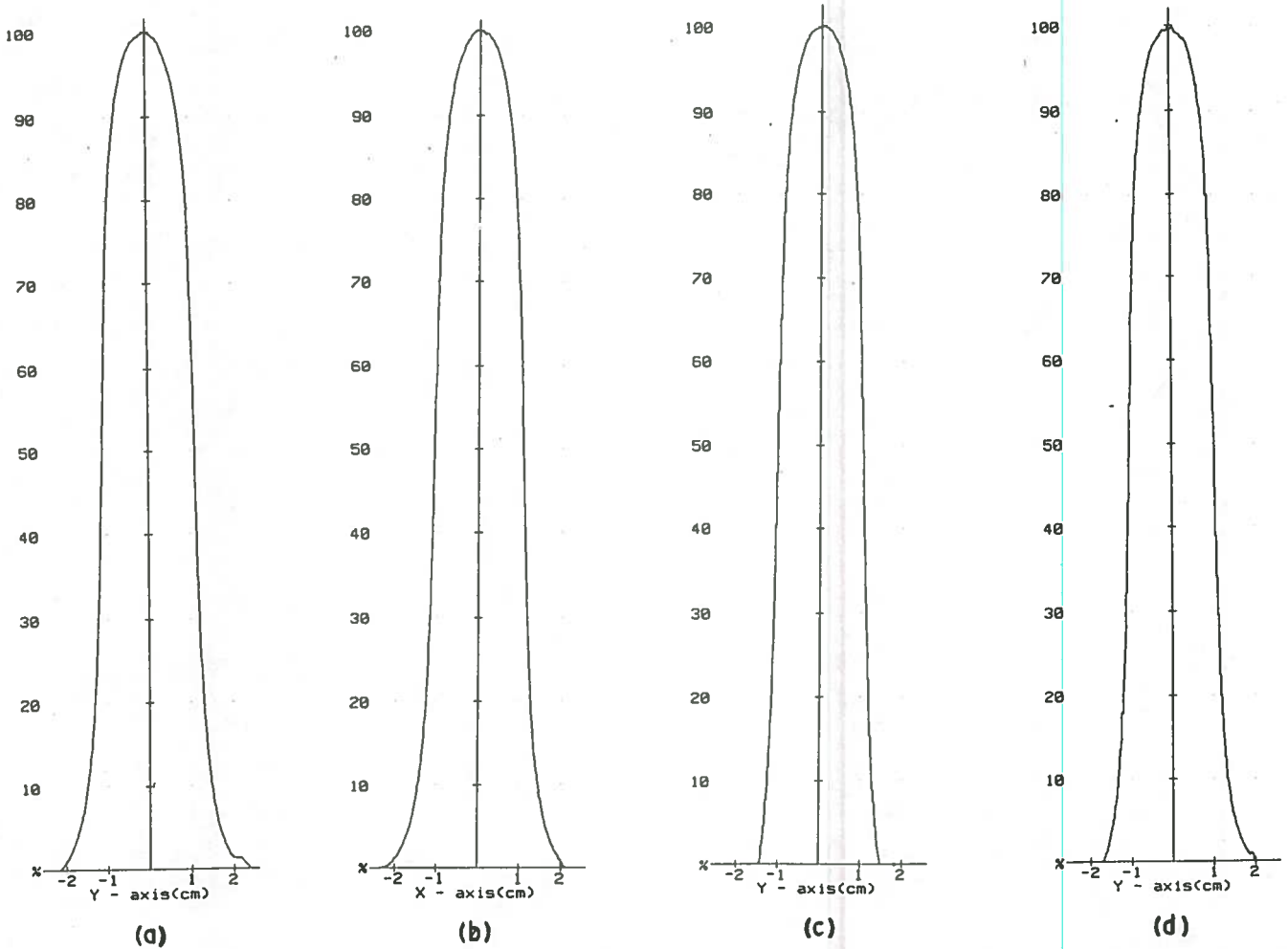

Figure 20a Cross profiles of cone 1 comparing perpendicular versus parallel placement of film scanned both inplane and crossplane. Experimental setup at 100cm SSD with a scan depth of 2.8cm. (a) perpendicular inplane scan (b) perpendicular crossplane scan (c) parallel inplane scan (d) parallel crossplane scan.

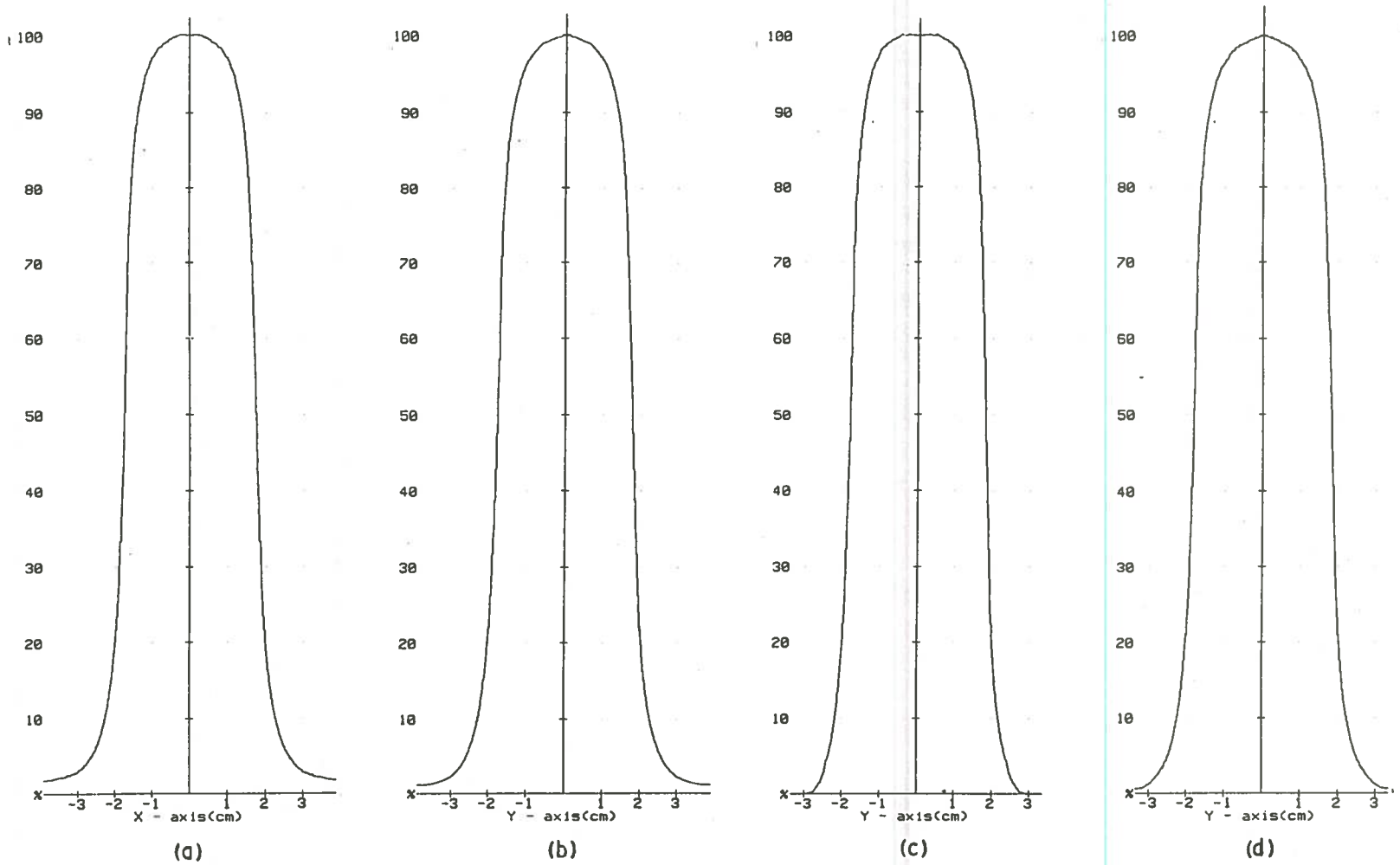

Figure 20b Cross profiles of cone 2 comparing perpendicular versus parallel placement of film scanned both inplane and crossplane. Experimental setup at 100cm SSD with a scan depth of 2.8cm. (a) perpendicular inplane scan (b) perpendicular crossplane scan (c) parallel inplane scan (d) parallel crossplane scan.

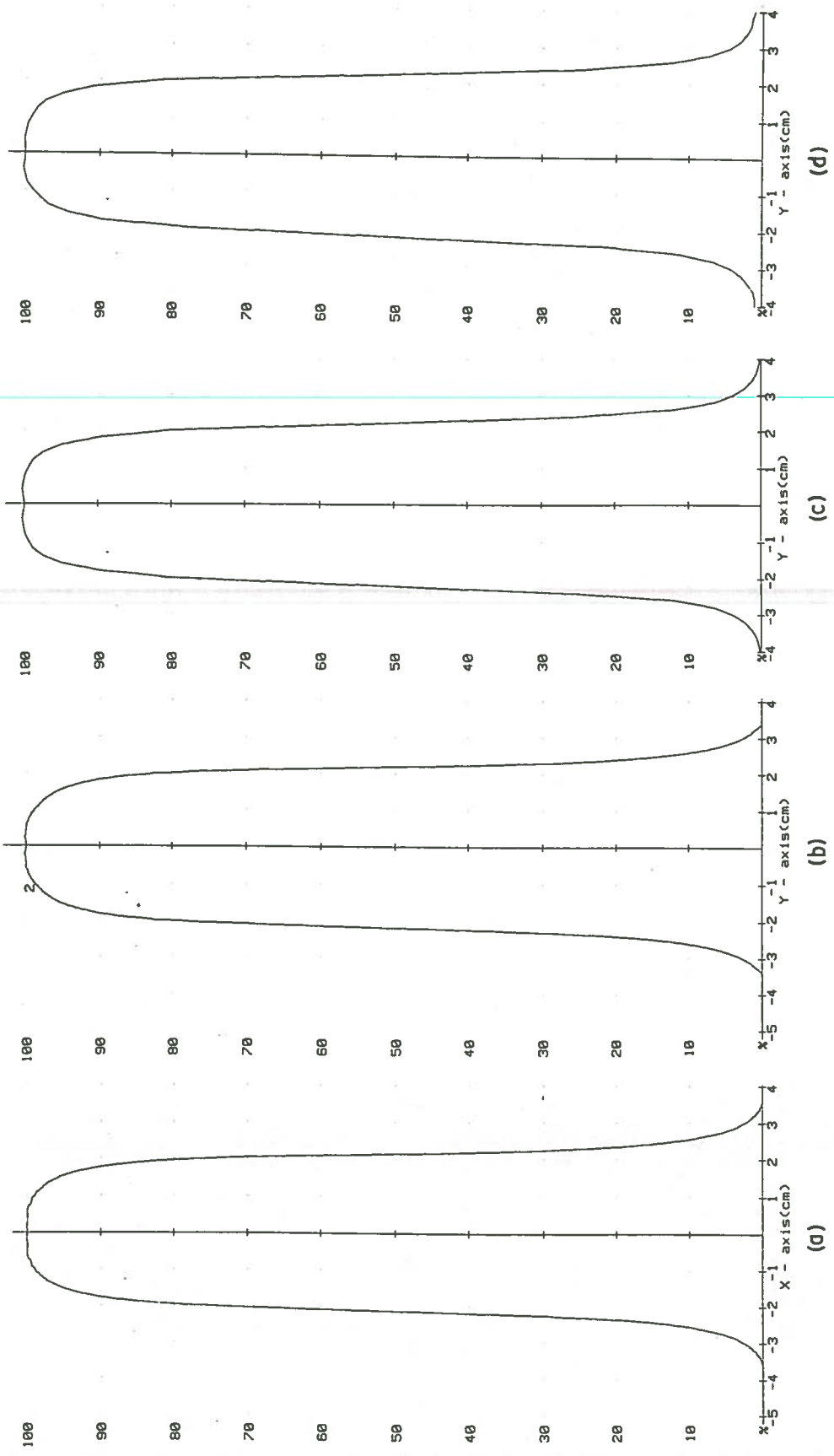

Figure 20c Cross profiles of cone 3 comparing perpendicular versus parallel placement of film scanned both inplane and crossplane. Experimental setup at 100cm SSD with a scan depth of 2.8cm. (a) perpendicular inplane scan (b) perpendicular crossplane scan (c) parallel inplane scan (d) parallel crossplane scan.

Table 1 Beam diameters at 90% and 50% isodensity/isodose points from film and diode measurements for cone 1, cone 2, and cone 3. Experimental setup at 100cm SSD at 2.8cm depth and referenced to isocenter.

	FILM		DIODE
	Perpendicular	Parallel	
CONE 1			
90%	1.40 +/- 0.04 cm	1.40 +/- 0.07 cm	1.50 +/- 0.05 cm
50%	2.10 +/- 0.05 cm	2.00 +/- 0.08 cm	2.00 +/- 0.02 cm
CONE 2			
90%	2.80 +/- 0.05 cm	2.70 +/- 0.10 cm	2.80 +/- 0.05 cm
50%	3.60 +/- 0.05 cm	3.40 +/- 0.13 cm	3.50 +/- 0.01 cm
CONE 3			
90%	3.40 +/- 0.06 cm	3.50 +/- 0.19 cm	3.60 +/- 0.07 cm
50%	4.30 +/- 0.07 cm	4.20 +/- 0.18 cm	4.30 +/- 0.03 cm

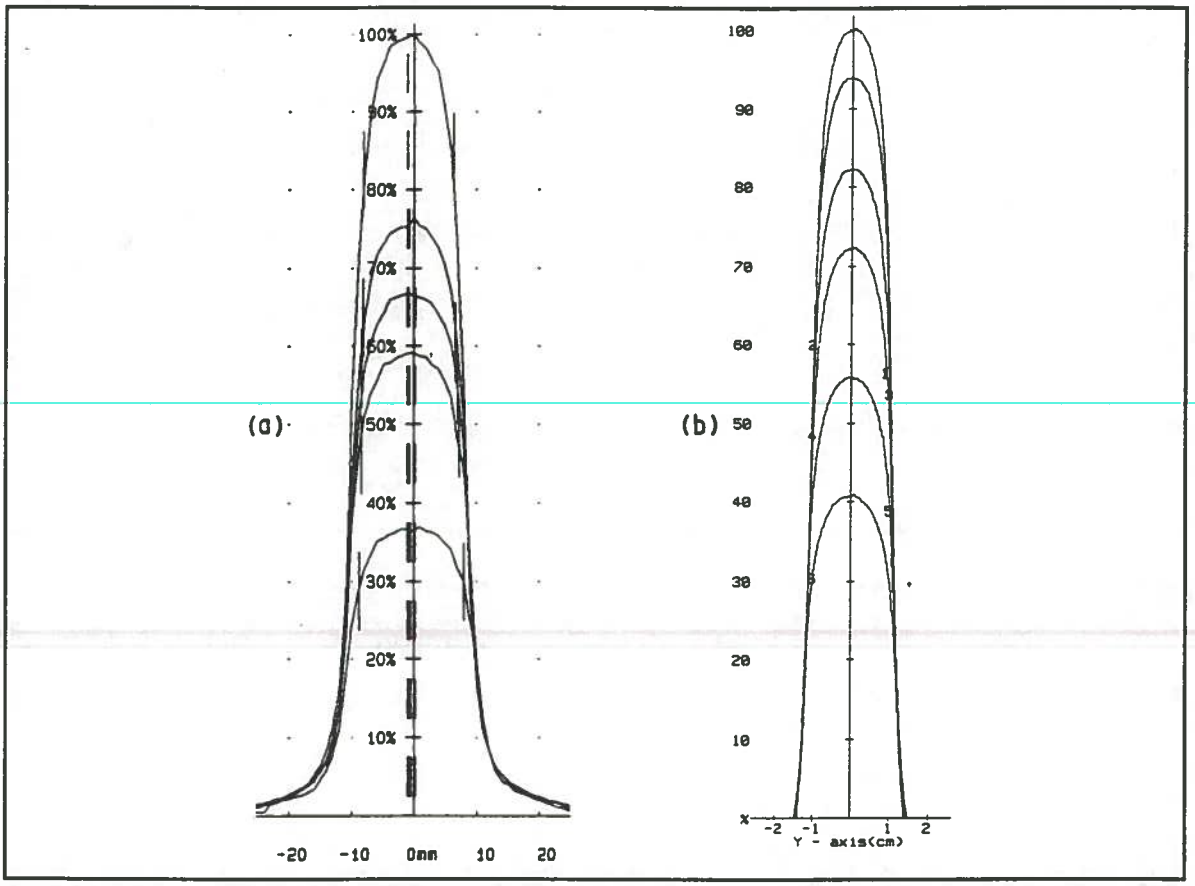

Figure 21a Diode inplane profile (a) of cone 1 at 2.8, 5, 7.5, 10, and 20cm depths 100cm SSD compared to the film (b) inplane profile under the same conditions. The difference between the scans is the lack of isodensity to isodose conversion.

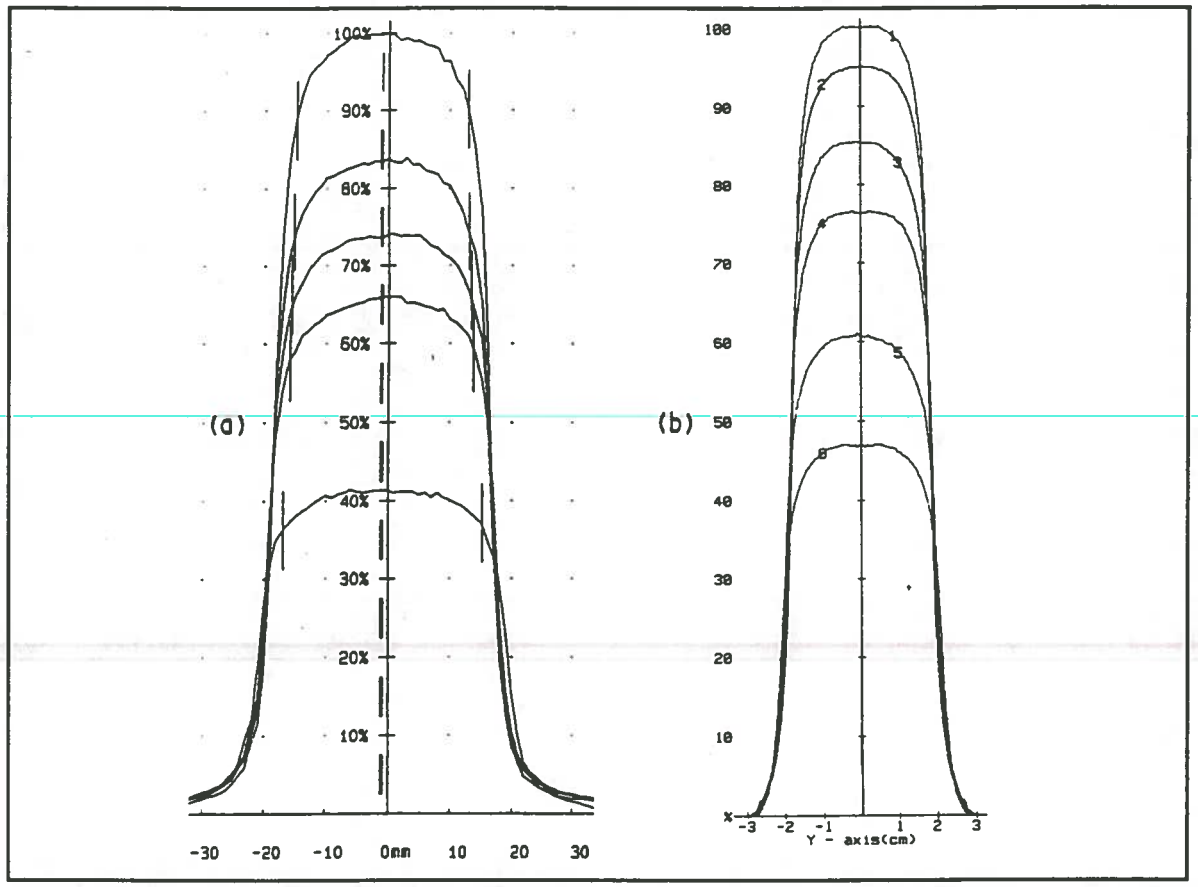

Figure 21b Diode inplane profile (a) of cone 2 at 2.8, 5, 7.5, 10, and 20cm depths 100cm SSD compared to the film (b) inplane profile under the same conditions. The difference between the scan is the lack of isodensity to isodose conversion.

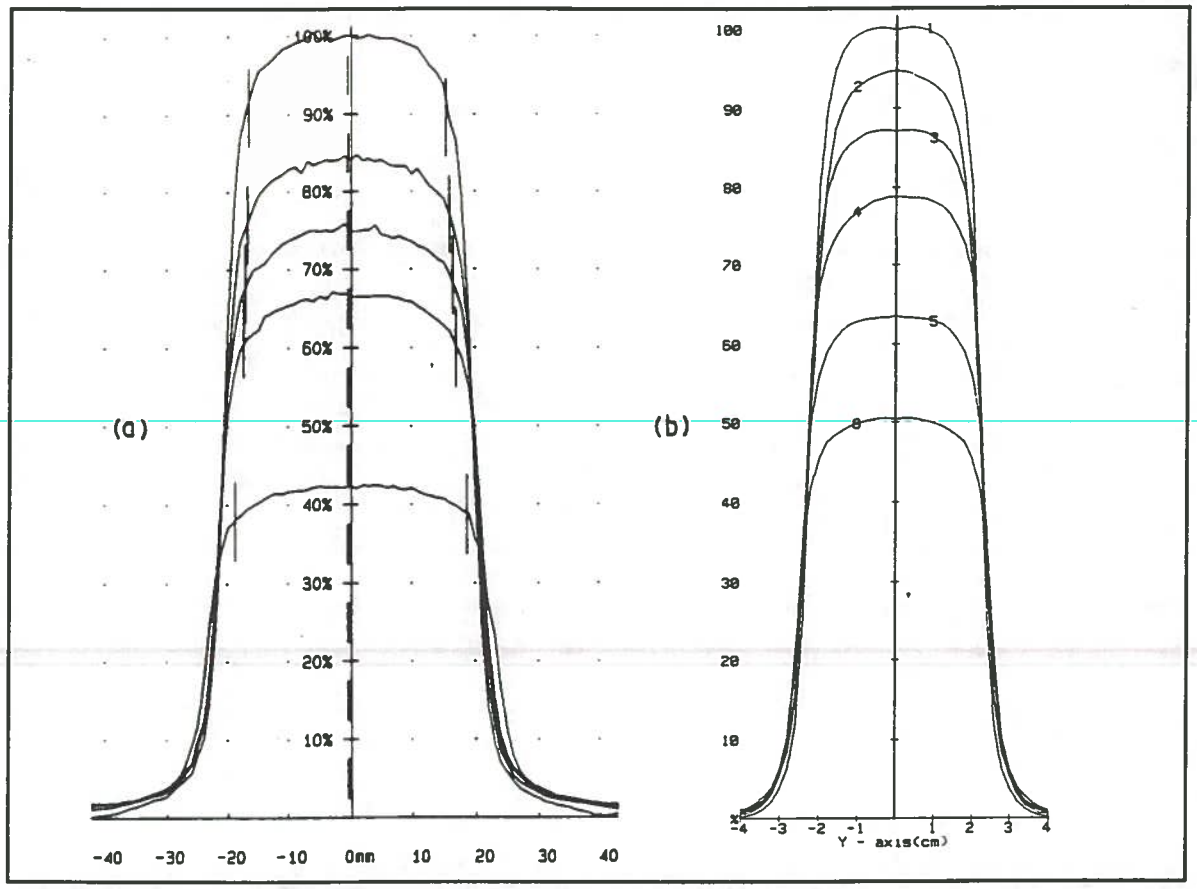

Figure 21c Diode inplane profile (a) of cone 3 at 2.8, 5, 7.5, 10, and 20cm depths 100cm SSD compared to the film (b) inplane profile under the same conditions. The difference between the scans is the lack of isodensity to isodose conversion.

Table 2 Comparison of beam diameters at 90% and 50% isodose points from in-water and in-air diode measurements for cone 1, cone 2, and cone 3. Experimental setup at 100cm SSD at 2.8cm depth and referenced back to isocenter.

	DIODE	
	In-Water	In-Air
CONE 1		
90%	1.50 +/- 0.05 cm	1.60 +/- 0.01 cm
50%	2.00 +/- 0.02 cm	2.00 +/- 0.00 cm
CONE 2		
90%	2.80 +/- 0.05 cm	3.10 +/- 0.01 cm
50%	3.50 +/- 0.01 cm	3.50 +/- 0.00 cm
CONE 3		
90%	3.60 +/- 0.07 cm	3.90 +/- 0.02 cm
50%	4.30 +/- 0.03 cm	4.30 +/- 0.00 cm

Table 3 Half beam penumbra widths generated from film measurements both perpendicular and parallel placement of the film and diode measurements in-phantom. Experimental setup at 100cm SSD at 2.8cm depths and referenced back to isocenter.

	FILM		DIODE
	Perpendicular	Parallel	
CONE 1			
90/10%	0.70 cm	0.57 cm	0.68 cm
80/20%	0.35 cm	0.32 cm	0.33 cm
CONE 2			
90/10%	0.85 cm	0.75 cm	0.78 cm
80/20%	0.42 cm	0.35 cm	0.37 cm
CONE 3			
90/10%	0.80 cm	0.87 cm	0.80 cm
80/20%	0.40 cm	0.50 cm	0.38 cm

Table 4 Comparison of half beam penumbra widths from in-water and in-air diode measurements for cone 1, cone 2, and cone 3. Experimental setup at 100cm SSD at 2.8cm depth and referenced back to isocenter.

	DIODE	
	In-Water	In-Air
CONE 1		
90/10%	0.68 +/- 0.05 cm	0.50 +/- 0.00 cm
80/20%	0.33 +/- 0.05 cm	0.20 +/- 0.00 cm
CONE 2		
90/10%	0.78 +/- 0.04 cm	0.65 +/- 0.02 cm
80/20%	0.37 +/- 0.05 cm	0.30 +/- 0.00 cm
CONE 3		
90/10%	0.80 +/- 0.07 cm	0.65 +/- 0.05 cm
80/20%	0.38 +/- 0.04 cm	0.25 +/- 0.05 cm

B. Film and TLD Dose Response

The film dose response curves determined at 2.8cm and 10cm depth for a 10x10cm field size at 100cm SSD were compared to determine if the film displays an energy dependence at depth. The results of this experiment indicates that a difference does exist at depth on the order of 9.1 +/- 0.9% averaged over the dose range of interest for a 10x10cm field size (Figure 22). However, from the discussion in Kubsads paper and in Mohans paper the same results for small fields would not be seen due to the flattening filter design which leads to a constant beam energy across the small beam diameters being studied (Kubsads et al., 1990, Mohan et al., 1985). From this idea further study needs to be done to determine if the film dose response from small fields will vary with depth as seen for large field sizes.

From the dose response data generated, the equation that is found to describe the curves follows the form of a rational function or rectangular hyperbola:

$$Y = \frac{X}{(a * X + b)} \qquad (13.)$$

where y and x are the net optical density and dose respectively and a and b are constants. The constants for the dose response curves described at 2.8cm and 10cm depth are a= 0.20347 $\frac{1}{O.D.}$, b= 26.564 $\frac{cGy}{O.D.}$ and a= 0.19493 $\frac{1}{O.D.}$, b= 23.940 $\frac{cGy}{O.D.}$ respectively with a r^2 of 1.000 and 0.999 for the 2.8cm and 10cm depths. The idea of linearizing the curves to predict the values beyond the experimental data were investigated realizing the limitations of the film due to saturation. The method used to linearize the dose response curves involved multiplying through

the above equation by 1/X to achieve the form

$$Y = \frac{1}{a + \frac{b}{X}} \qquad (14.)$$

then by taking the inverse of this equation the form

$$\frac{1}{Y} = a + \frac{b}{X} \qquad (15.)$$

which is the equation of a straight line.

$$Y = bX + a \qquad (16.)$$

The plot of the inverse optical density versus the inverse dose yielded a straight line (Figure 23).

The use of Lithium Fluoride (LiF) TLDs poses its own problem for the use in absorbed dose determination. The published reproducibility in absorbed dose determination is on the order of 5% and under ideal conditions 2% has been claimed. The response of the TLD is dependent on its mass and therefore a correction factor is needed. The TLD does not show an energy dependence and therefore no correction is needed. Since large numbers of TLDs were needed the idea of weighing the TLDs after each exposer became impracticable. The method chosen to achieve reproducibility for 300 TLDs was to determine the sensitivity of each TLD rod. This was achieved by delivering an equal dose of 100 cGy to each TLD and then determining the light output given off by each. The thermoluminescence measured in microcoulombs (μC) is plotted versus number of TLDs with the same reading in histogram form. A family of TLDs with a +/- 5% spread were chosen. The TLD readings were averaged and then the average reading divided by each of the TLD reading to get a correction factor unique to each TLD and independent of the mass (Table 5). The plot of TLD reading versus dose gives a linear response

following the form:

$$Y = mX + b \qquad (17.)$$

where y and x are dose and TLD reading respectively and m and b are constants. The plot yielded a slope of 20.0 $\frac{cGy}{\mu C}$ with a r^2 of.998 (Figure 24). The equation used to calculate TLD dose:

$$\text{Dose(cGy)} = 20\,\frac{cGy}{\mu C} * \text{corrected TLD reading } (\mu C) \qquad (18.)$$

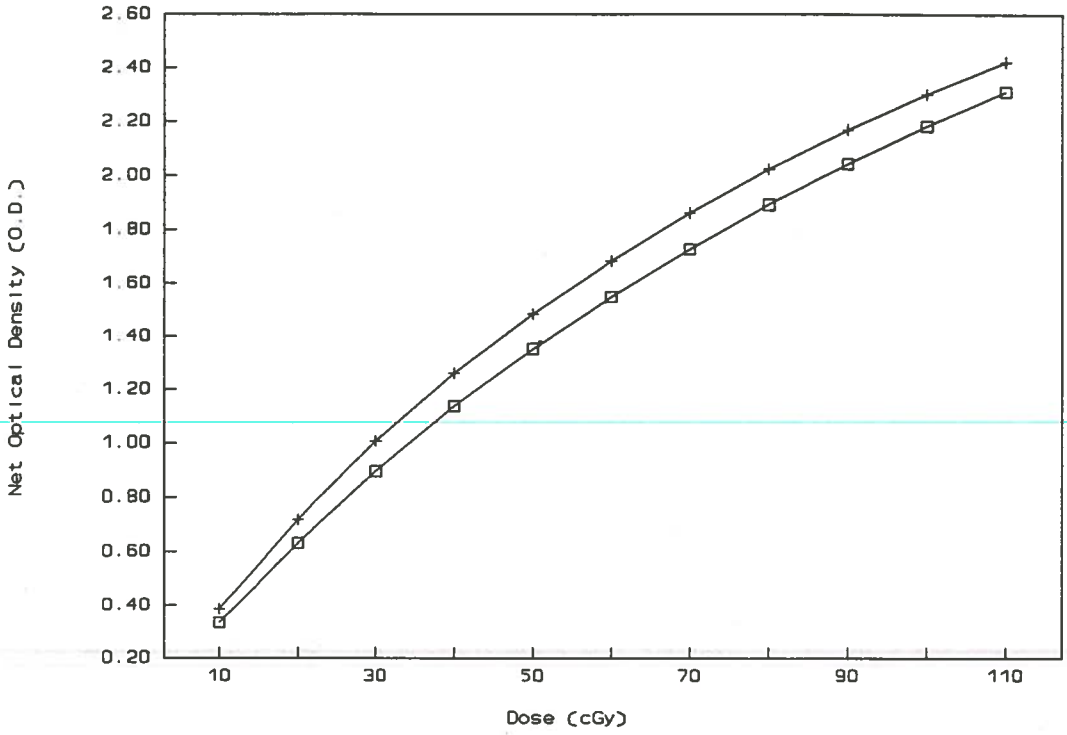

Figure 22 Film response curve at 2.8cm (□) and 10cm (+) depths for 10x10cm F.S. at 100cm SSD. The results of this suggest an over response of the film at depth due to the film's energy dependence.

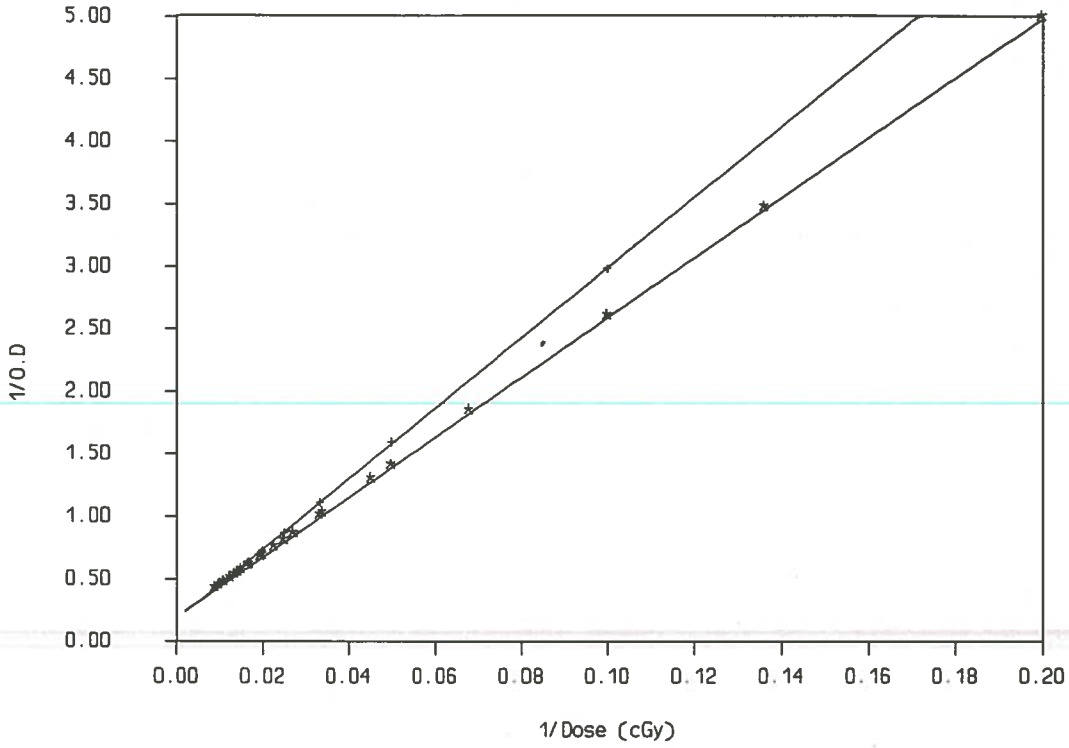

Figure 23 Linearilizing the film dose response curves for the 2.8cm (+) and 10cm (*) depths allows easier prediction of data points beyond the experimental bounds within the limitations of the film.

Table 5 TLD correction factors. The TLD rods are identified by a letter and number code. The correction factor is multiplicitive.

	A	B	C	D	E	F	G	H	I
1	-	-	-	-	0.96	1.02	1.00	1.01	0.98
2	1.04	1.03	1.05	1.06	1.02	1.00	1.06	1.01	1.00
3	0.99	0.97	-	1.04	-	-	0.98	1.02	1.00
4	0.97	1.02	0.97	-	1.02	1.00	0.98	-	1.01
5	1.02	0.96	1.00	1.00	0.99	1.07	1.07	1.00	0.97
6	1.02	1.00	0.97	1.00	0.97	0.96	-	-	-
7	1.01	-	1.00	1.02	1.03	-	1.02	1.04	1.07
8	1.01	0.98	-	-	1.05	0.99	0.97	0.97	1.01
9	0.99	0.98	0.95	0.96	1.03	-	1.02	1.00	1.01
10	-	-	0.97	1.03	1.02	-	0.97	0.97	0.99
11	1.04	0.96	1.05	1.01	1.01	1.00	0.98	0.99	1.00
12	-	1.02	0.99	0.97	-	1.02	-	0.96	0.99
13	0.96	-	1.01	1.03	0.99	1.01	0.97	1.00	1.02

	J	K	L	M	N	O	P	Q	R
1	-	1.05	1.02	1.06	1.04	1.02	-	1.03	0.99
2	0.95	-	1.03	-	0.96	0.99	-	0.96	1.02
3	0.99	-	-	-	0.97	1.01	1.03	0.96	-
4	0.97	-	-	0.99	-	0.97	-	0.96	0.97
5	1.00	0.98	-	1.00	0.97	0.98	-	0.98	-
6	-	0.96	1.01	0.99	-	0.98	0.99	0.98	0.97
7	-	1.01	1.03	1.05	1.05	1.02	1.00	-	0.96
8	-	1.00	-	-	0.99	1.00	0.96	0.97	0.96
9	-	1.06	0.96	1.04	-	-	0.98	0.96	1.02
10	1.01	1.03	1.02	1.02	-	0.97	1.02	0.97	0.97
11	1.01	1.00	1.06	1.05	1.06	-	-	1.06	-
12	1.01	1.01	0.99	1.02	1.03	-	-	1.01	0.96

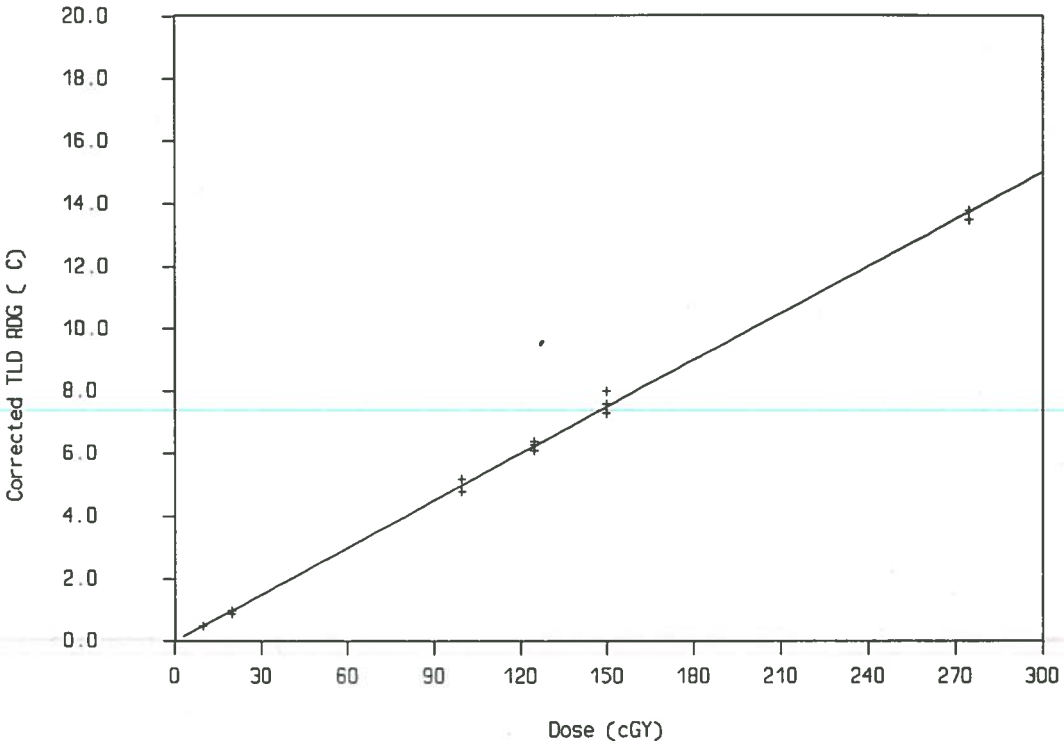

Figure 24 TLD dose response curve showing the corrected TLD reading (μC) versus given dose for 10x10cm F.S. @ 100cm SSD with 2.8cm polystyrene buildup.

C. Central Axis Depth Dose

Because of the small fields being measured there exist a volume limitation on detector size for central axis depth dose measurements. The reason is due to the lack of lateral electronic buildup resulting from the rapid dose fall off from the central region to the periphery of the detector from these small fields on the order of 10%/mm (Houdek et al., 1983, Rice et al., 1987). The central axis depth dose data for cone 1, cone 2, cone 3, and field sizes ranging from 4x4cm to 14x14cm was determined using the Markus parallel plate chamber (collection volume of 0.04cc) by both manual and by the CRS beam scanner methods and normalized to 2.8cm depth (Table 6). The other method employed to determine the small field central axis depth dose data is by plotting the central axis depth dose values for the measured fields (4x4cm to 10x10cm) and the zero area depth dose data versus field size and then determining the small field depth dose values from the curves (Figure 25).

The Markus chamber generated data was compared to the depth dose values used by MBPCC and the published values from BJR supplement 17 for field sizes ranging from 4x4cm to 14x14cm and depths from surface to 20cm showing that the Markus gave comparable results within 2%. The difference seen in the buildup region varied with field size with a difference ranging from 1.8% to 7.6% at 1cm depth from the largest to smallest field sizes (14x14cm to 4x4cm) in comparison to the MBPCC data. The differences seen could be the result of the chamber used in the determination of the depth dose values for the MBPCC data. From the paper by Mellenberg the over response of the Markus PP is on the order

of 0.6 to 0.9 percent at 1cm depth and decreases with increasing depth when compared to a extrapolation chamber for 10 MV and 18 MV photons respectively (Figure 26). The results of the comparison of the Markus and the PTW 0.1cc and diode detector show that the difference range was found to be field size independent with the Markus giving consistently greater depth dose values in the buildup region on the order of 4% to 6% over the PTW 0.1cc and diode detector. The PTW 0.1cc chamber and diode were also used in the determination of the central axis depth dose data and compared to the Markus chamber with the data varying from 2% to 10% at depth for all field sizes (4x4cm to 14x14cm) for both the diode and PTW 0.1cc chamber.

The manual versus the CRS beam scanner determination of the central axis depth dose gave comparable results for each of the cones, the 5x5cm, and 10x10cm field sizes for 4cm, 8cm, 12cm, 16cm, and 20cm depths with a difference of less than 2% for all fields and depths (Table 7).

The final analysis being the CRS system gives comparable results to manual methods and published data and therefore can be used with confidence in the determination of the central axis depth dose.

Beam attenuation was measured in water along the central axis for various field sizes ranging from 4x4cm to 8x8cm and also for cone 1, cone 2, and cone 3 by measuring the beam ionization behind varying thickness of water (6cm, 10cm, 14cm, 18cm, and 20cm of water) (Table 8). If good geometry was achieved, the resulting attenuation curve would be exponential in form and independent of field size. The results of the experiments yielded curves which were exponential in nature with an

average slope value (effective linear attenuation coefficient) of 0.0327 +/- .0003 cm^{-1} which translates into an HVL of 21.2cm of water. This is in good agreement with the published values of 0.0326 cm^{-1} (van de Geijn et al., 1984, Thomas, 1970) and HVL of 21.3cm in water (Nath et al., 1977). The linear attenuation coefficient for cone 1 (0.0334 cm^{-1}) did not fall within 1σ of the expected value due to the loss of electronic equilibrium. The resulting effective linear attenuation coefficient will be used to determine the zero area fractional depth dose and will be confirmed from the determination of the effective linear attenuation coefficient from the exponential portion of the TMR derived curve.

The determination of the small field central axis depth dose from the plot of the large field central axis depth dose and the zero area depth dose was in good agreement with the manual and CRS derived central axis depth dose within 1% for all cones. The resulting central axis depth dose values will be normalized to 100% at 2.8cm depth and not the depth of maximum dose for each field size. The central axis depth dose in conjunction with the normalized peak scatter factors will be used in the determination of the central axis tissue maximum ratios.

Table 6 Normalized central axis depth dose, Clinac 20, 15 MV x-rays 100cm SSD with the zero area depth dose derived from narrow beam linear attenuation coefficient.

Depth (cm)	Cone				Square Field Size				
	1	2	3						
	0x0	1.8^2	3.1^2	3.8^2	4^2	5^2	8^2	10^2	14^2
2.8	100.0	100.0	100.0	100.0	100.0	100.0	100.0	100.0	100.0
3.0	99.0	100.0	100.0	100.0	100.0	100.0	99.9	99.8	99.8
4.0	93.9	96.8	97.6	97.5	97.5	97.5	97.5	97.3	96.8
5.0	89.2	92.0	94.0	94.2	94.3	94.9	94.5	94.3	93.3
6.0	84.7	87.6	89.6	90.0	90.1	90.5	90.6	90.4	89.9
7.0	80.5	83.9	85.4	86.1	86.0	86.6	87.1	86.5	86.6
8.0	76.4	79.6	81.6	81.9	82.0	82.8	83.2	83.5	83.4
9.0	72.6	75.7	77.9	78.0	78.6	79.0	79.7	79.9	80.2
10.0	69.0	72.2	73.8	74.7	75.1	75.4	76.2	76.3	77.2
11.0	65.6	68.8	70.5	71.3	71.4	72.0	72.9	73.3	74.2
12.0	62.4	65.4	67.2	67.7	68.1	68.8	69.7	70.0	71.0
13.0	59.3	62.0	64.0	64.9	65.0	65.6	66.8	67.6	68.6
14.0	56.4	58.8	61.2	61.6	61.9	62.7	63.9	64.3	65.7
15.0	53.6	56.2	58.1	59.0	58.9	59.5	61.1	61.6	63.2
16.0	51.0	53.5	55.2	56.0	56.3	56.9	58.2	58.9	60.5
17.0	48.5	51.1	52.6	53.3	53.6	54.1	55.6	56.5	58.1
18.0	46.2	48.7	50.1	50.5	51.0	51.5	53.3	54.1	55.6
19.0	43.9	46.0	47.7	48.5	48.5	49.2	50.9	51.7	53.2
20.0	41.8	43.6	45.4	45.9	45.9	46.7	48.5	49.2	51.3

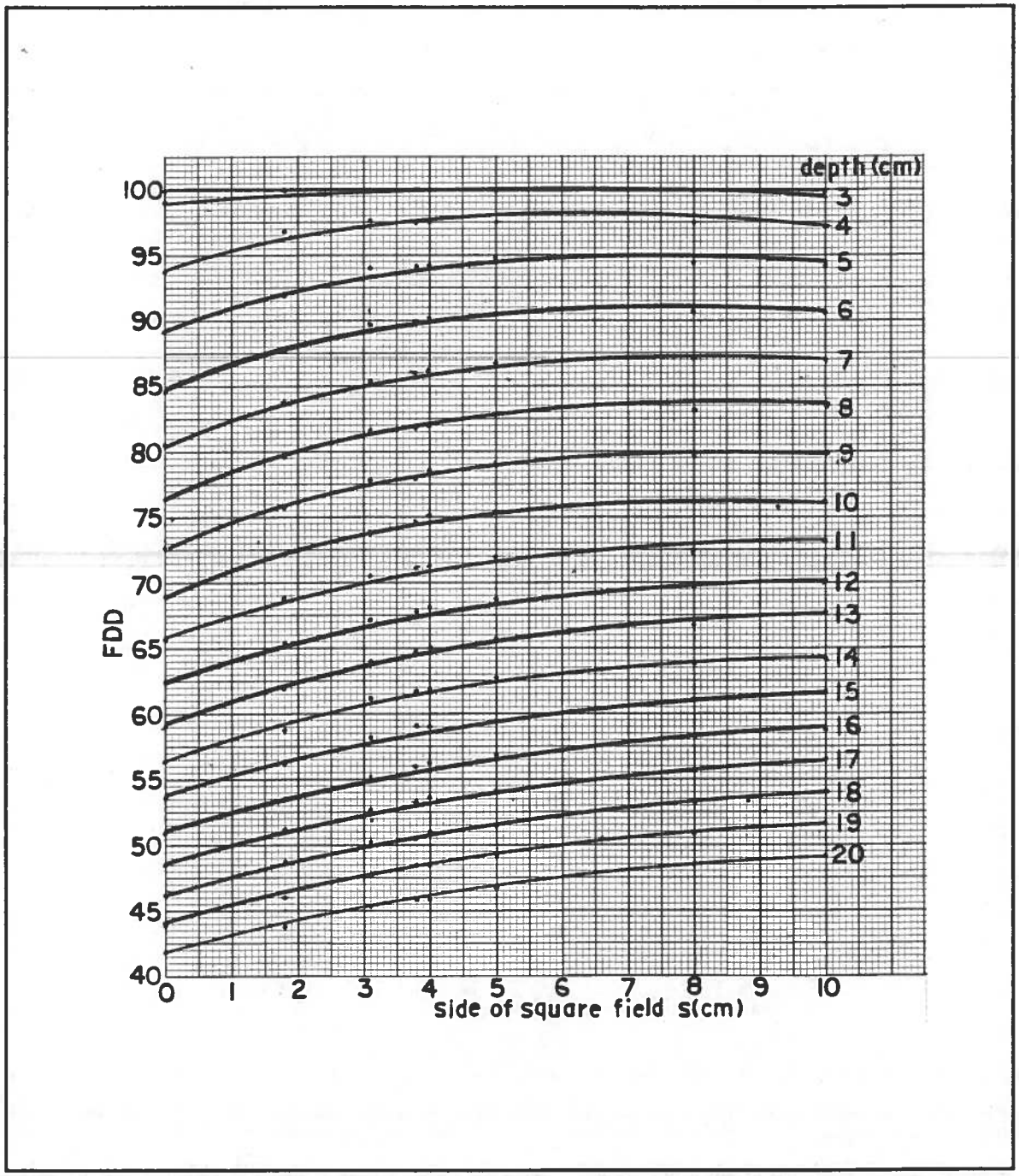

Figure 25 Graph of the normalized depth dose values and zero area depth dose versus side of square field for determination of cone 1, cone 2, and cone 3 depth dose values.

Table 7 Ratio of the CRS derived depth dose values versus the manually derived values for cone 1, cone 2, cone 3, 5x5cm, and 10x10cm field sizes.

	Cone (dia.)			Collimator	
Depth (cm)	2.0cm	3.5cm	4.3cm	5x5cm	10x10cm
4	1.007	1.004	1.001	1.003	1.000
8	1.007	1.007	1.004	1.004	1.006
12	1.006	1.001	1.001	1.003	0.997
16	0.998	0.996	1.000	0.998	0.997
20	0.980	0.985	0.983	0.985	0.992

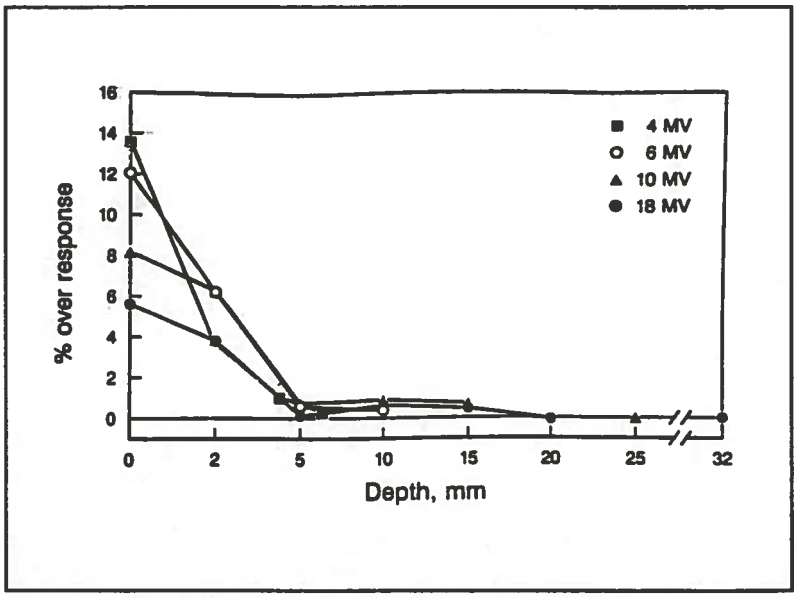

Figure 26 Graph depicting the Markus over response for the 4 MV, 6 MV, 10 MV, and 18 MV photon beams (Mellenberg, 1990).

Table 8 Ionization values determined behind varying Thickness of water for various field sizes to be used in the determination of the narrow beam derived zero area linear attenuation coefficient following a simple exponential function.

Thickness of H_2O	TPC Corrected Electrometer Reading Equivalent Square Fields (s)							
	$1.8cm^2$	$3.1cm^2$	$3.8cm^2$	$4.0cm^2$	$5.0cm^2$	$6.0cm^2$	$7.0cm^2$	$8.0cm^2$
0cm	1.3333	1.3897	1.3956	1.3987	1.4205	1.4393	1.4563	1.4750
6cm	1.0743	1.1273	1.1325	1.1343	1.1520	1.1680	1.1850	1.2003
10cm	0.9350	0.9873	0.9913	0.9938	1.0103	1.0253	1.0406	1.0533
14cm	0.8240	0.8678	0.8720	0.8737	0.8880	0.9023	0.9140	0.9273
18cm	0.7172	0.7600	0.7630	0.7643	0.7788	0.7893	0.8013	0.8137
20cm	0.6712	0.7140	0.7175	0.7202	0.7305	0.7423	0.7520	0.7620

D. Scatter Correction Factors

The relationship between the monitor unit and dose at the depth of maximum is a function of the primary dose component and the scatter dose component. The combination of these primary and scatter components was described by Holt et al., 1970 and termed the total scatter correction factor (S_t) which is also commonly known by other terms as the field size dependence in phantom (FSD_p) or the output factor (OF).

The total scatter correction factor (S_t) is separated into the collimator dependence factor (S_c) or field size dependence in air (FSD_a) and phantom scatter component (S_p) with the collimator dependence factor being a function of the collimator scatter within the accelerator head and the primary component. The phantom scatter component (S_p) or normalized peak scatter factor (NPSF) is calculated from the S_t or FSD_p and S_c or FSD_a but also can be determined experimentally from the peak scatter factors or tissue air ratio at the depth of maximum dose.

The field size dependence in phantom was experimentally determined utilizing the Markus chamber and TLDs with the combined results found in table 9. The results show a good agreement between the experimental values and expected values within 2% with the expected values being those used by MBPCC. The circular fields were converted to equivalent square fields (Br. J. Radiol. suppl. 17) and the averaged FSD_p data plotted versus side of field (Figure 27). The deviation seen in the curve is due to the increased output of the cones when compared to equivalent field size defined by the primary collimator (Rice et al., 1987). This is due to the constant head scatter created when the primary collimator is set to 5x5cm field size for all cones.

The method used to determine the field dependence in air (FSD_a) was the use of the Markus parallel plate chamber with superflab or high impact white polystyrene disks as buildup (Table 9). It was determined that the use of superflab and white poly yielded comparable results within 0.5%. It was also determined that the use of backscatter material in conjunction with buildup did not significantly change the results and therefore it was left off. Due to the small fields being used at the standard 100cm SSD setup electronic equilibrium was not achievable. To alleviate this condition numerous experimental setups were used such as a brass buildup cap fitted to the PTW 0.3cc chamber, extended SSD's beyond 100cm SSD for the Markus/superflab combination, and TLD's. The brass results for in air measurements were within 2% for all field sizes in relation to the superflab results. The Markus/superflab combination at extended SSD's yield results within a 0.5% of the results achieved at 100cm SSD except for the 2cm diameter cone were there was an increase of 6.5% in the output, which confirms that electronic equilibrium was not achieved at the 100cm SSD experiment. The TLD results fell within the 5% error reported for TLD work but most of the results fall within 2% to 3% of the Markus/ superflab results. The graph of the field size dependence in air versus the side of field here again shows the deviation of the cone results from the standard curve generated from the primary collimator (Figure 28). Since the same collimator field size is used for all cones the field size dependence theoretically should be the same for each cone. The results reflect this theory with the cone results within 1% of the FSD_a for the 5x5cm field.

The phantom scatter component (S_p) or normalized peak scatter factor (NPSF) can be calculated from the field dependence in phantom and air according to the equation above. The NPSF's were calculated and plotted for the primary collimator set field sizes as well as the cones (Table 9). The resulting curve does not show the deviation in the cone data as found in the FSDp and FSDa since the phantom scatter component is dependent on the area of the phantom being irradiated (Figure 31). The calculated results fall within 1% of the published results found in the British Journal of Radiology supplement 17, 1983 and Spicka et al., 1988. The NPSF factors were fitted to an hyperbolic function according to Horns paper which yielded an equation following the form with an r^2 of .990 (Horn, 1981):

$$NPSF(s) = 1.014226 - \frac{0.1303259}{(- 0.8387159 + F.S)} \qquad (18.)$$

which will be used in conjunction with the fractional depth dose to calculate the tissue maximum ratios and zero area tissue maximum ratio.

The peak scatter factor (PSF) was determined for the 10x10cm field size using the PTW 0.6cc chamber and acrylic buildup cap with a measured value of 1.022 which is in good agreement with the published value of 1.021 (Personal communication from the Radiological Physics Center (RPC)). For the other field sizes and cones the PSF was calculated by varying equation 9 using the known NPSF(s) and the PSF(10) with the results for the 20x20cm and 30x30cm within 0.5% of the expected values of 1.034 and 1.044 respectively (Personal communication with the RPC) (Table 9). The experimental determination of the peak scatter factor for a 5x5cm, 10x10cm, and 20x20cm field size using the brass buildup cap

and the PTW 0.3cc chamber yielded results which were not consistent with the expected values. The experimental results yielded in-air measurements which were greater than the in-water measurements which yielded peak scatter factors ranging from 0.974 for the 20x20cm to 0.980 for the 5x5cm. The reason for this discrepancy is unknown and further evaluation is needed.

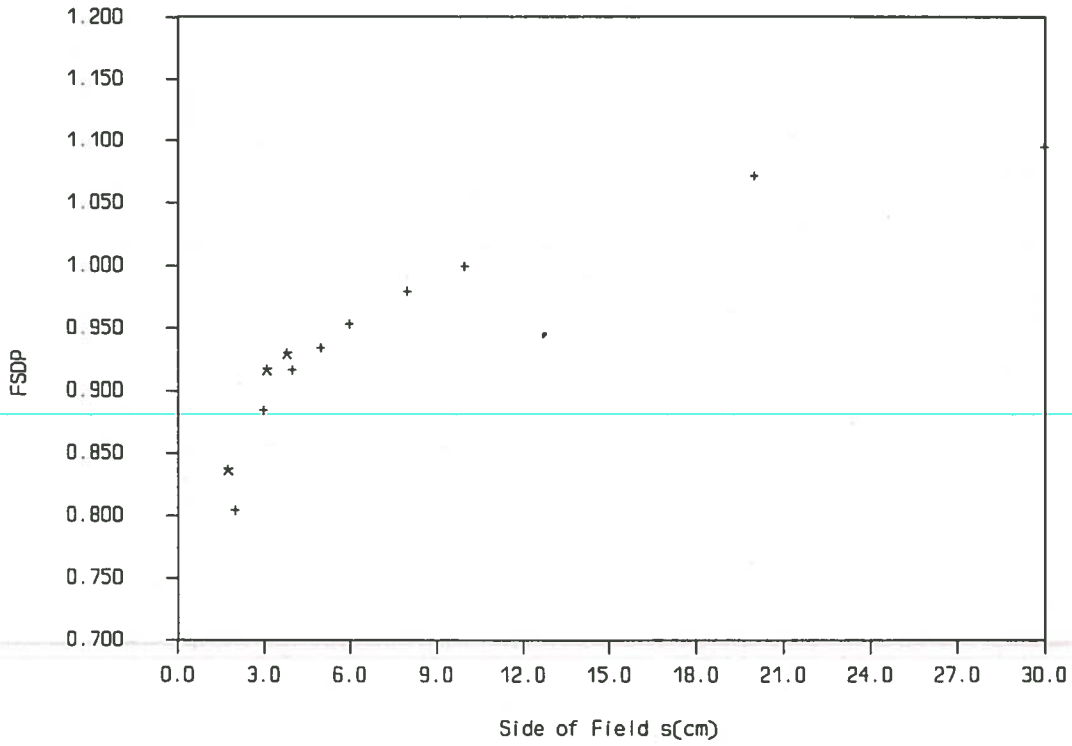

Figure 27 Field size dependence in phantom as a function of side of field for square fields showing the effect of the head scatter and phantom scatter for the cones (*) and the collimator fields (+).

Table 9 Summary of scatter correction factors for cone 1, cone 2, and cone 3 and square fields from 2x2cm to 30x30cm.

Side of * Square Field	FSD_p	FSD_a	NPSF	PSF**
1.8	0.834 +/- 0.005	0.954 +/- 0.004	0.874	0.893
3.1	0.914 +/- 0.002	0.954 +/- 0.003	0.958	0.979
3.8	0.925 +/- 0.003	0.954 +/- 0.002	0.970	0.991
2.0	0.812 +/- 0.047	0.922 +/- 0.003	0.881	0.900
3.0	0.885 +/- 0.010	0.931 +/- 0.009	0.950	0.971
4.0	0.920 +/- 0.004	0.947 +/- 0.008	0.971	0.992
5.0	0.935 +/- 0.003	0.956 +/- 0.007	0.978	0.999
6.0	0.954 +/- 0.001	0.963 +/- 0.006	0.990	1.012
8.0	0.980 +/- 0.000	0.984 +/- 0.002	0.995	1.015
10.0	1.000 +/- 0.000	1.000 +/- 0.000	1.000	1.022
20.0	1.072 +/- 0.000	1.055 +/- 0.006	1.016	1.038
30.0	1.095 +/- 0.000	1.066 +/- 0.007	1.027	1.050

*Where the field size for cone 1, cone 2, and cone 3 are reported as a side of a square field according to the equation: F.S. = r * $\sqrt{\pi}$ where r is the radius of the circle

**PSF derived from the measured value for 10x10cm F.S. and calculated for the other field sizes.

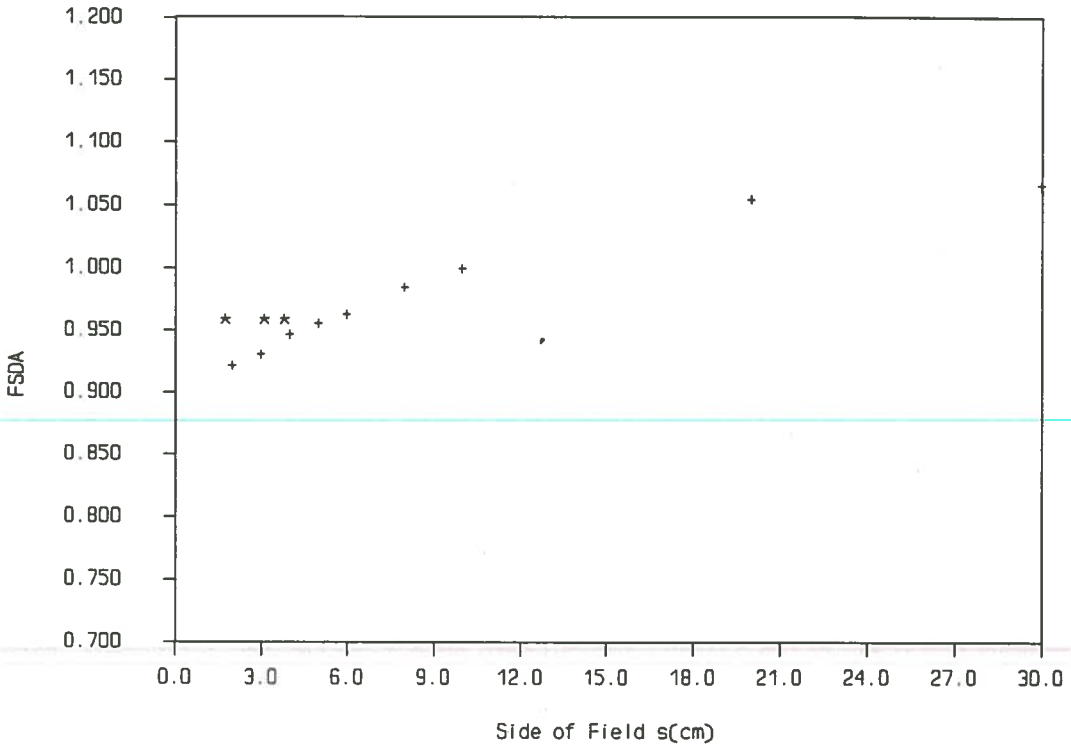

Figure 28 Field size dependence in air as a function of side of field showing the effect of the head scatter only for the cones (*) and for the collimator fields (+).

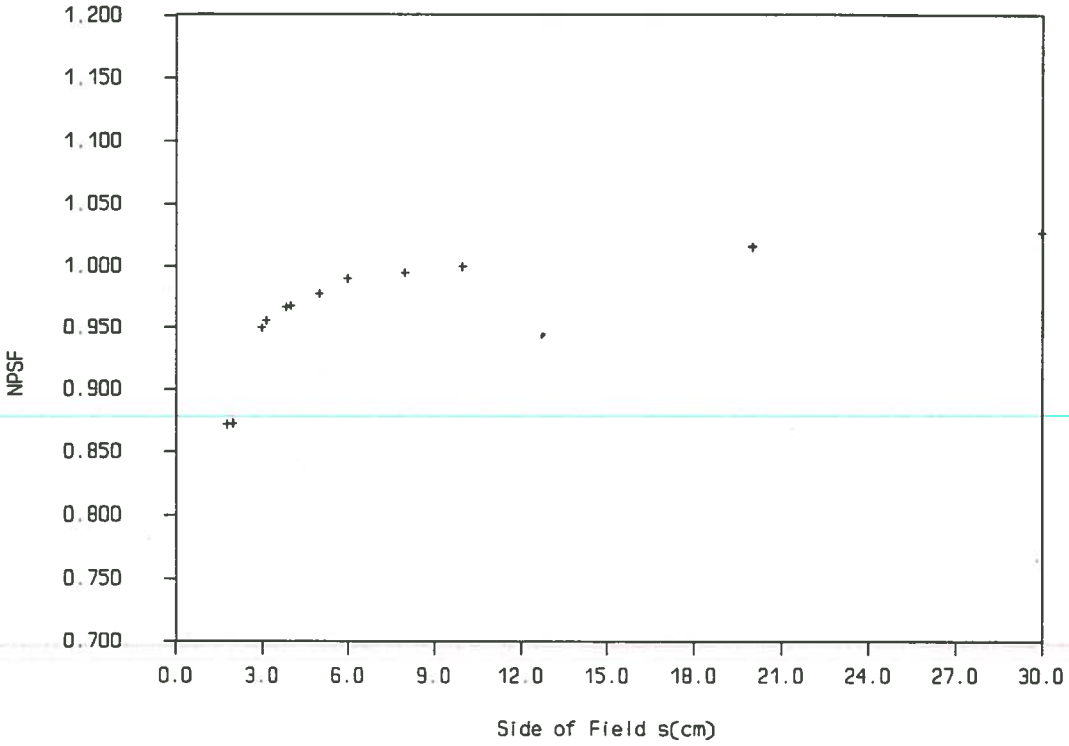

Figure 29 Normalized peak scatter factor as a function of side of field for square fields showing the effect of the phantom scatter only for the circular cones and collimator fields.

E. Central Axis Tissue Maximum Ratio

The FDD/NPSF derived TMR values using equation 11 for cone 1, cone 2, cone 3 and field sizes ranging from 4x4cm to 10x10cm can be found in table 10. Since no data exists for small fields using 15 MV photons, the FDD/NPSF derived results are confirmed by manual determination using the Markus chamber and extrapolation using the zero area TMR's and BJR supplement 17 data. The TMR values were derived from the FDD and NPSF according to the conversion formula 2a found in the BJR supplement 17 with the field size defined at surface.

The manually determined TMR values at 5cm, 10cm, 15cm, and 20cm depths were compared and were found to be within 2.0% of the FDD/NPSF derived TMR's (Table 11 columns a and b). The comparison between the extrapolated TMR values and FDD/NPSF derived TMR's showed a increasing deviation with depth for cone 1 on the order of 3.5% with the deviation decreasing to 0.2% at the shallow depths with the other cones within 1.0% at all depths (Table 11 column a and c). The paper by Houdek et al. 1983 suggest that for small fields there is a rapid falloff of dose at the shallow depths with the dose at depth approaching the zero-area data which is observed with cone 1's TMR values (Table 10). The TMR data for the 5x5cm to 10x10cm field sizes are corroborated by the data for the infinite SSD found in the BJR supplement 17 within 2% except at deep depths were the deviation is 3.5%.

Two methods are discussed for the determination of the zero-area TMR values. The first method is by exponential fit of the TMR data versus depth beyond 10cm depth for each cone and field sizes ranging from 4x4cm to 10x10cm. The resulting slope values (linear attenuation

coefficients) for each of the field sizes are then plotted versus field size and extrapolated back to zero area to obtain the effective linear attenuation coefficient for a zero area field. This value is then used according to equation 12 to calculate the zero area TMR's. The resulting extrapolated zero area linear attenuation value of 0.0331 cm^{-1} was determined from the plot of the TMR values for sides of fields of $4cm^2$ to $10cm^2$. The extrapolated value is in agreement with the narrow beam derived linear attenuation coefficient (.0327 +/-0.0003) and the published value of 0.0326 (Van de Geijn et al., 1984, Nath et al., 1977, Thomas, 1970). However, when the cone derived values are plotted versus side of field the extrapolated zero area value increases to .0381 (Figure 30). A possible explanation in the increase in the linear attenuation coefficient seen with the cones is due to the high energy secondary electrons produced from primary photon interaction and the lower energy secondary electrons produced from the scatter photons within the accelerator head. With the practical range of the high energy secondary electrons produced from the primary photon interactions exceeding the diameter of the small field and therefore are lost. Whereas, the lower energy electrons produced from the accelerator head scatter the practical range is less than that of the beam diameter being studied and therefore are detected which decreases the mean energy of the beam and increases the interactions per distance of travel which is displayed as an increase in the linear attenuation coefficient. The final method is by direct determination of the narrow beam linear attenuation coefficient (see central axis depth dose section). The resulting difference in the two values excluding the cone derived values

yielded an average maximum variation of 1% in the calculated zero area TMR values with the TMR derived linear attenuation coefficient giving the steepest falloff at all depths (Table 11). The papers by Rice et al. 1987 and Ikoro et al. 1987 suggest that both methods of deriving the effective zero area linear coefficient should give comparable results.

Table 10 Tissue maximum ratios, Clinac 20, 15 MV x-rays 100cm SCD with the zero area TMR's derived from both TMR extrapolated and narrow beam linear attenuation coefficient.

Depth (cm)	(a) 0cm²	(b) 0cm²	1.8cm²	3.1cm²	3.8cm²	4cm²	5cm²	10cm²
2.8	100.0	100.0	100.0	100.0	100.0	100.0	100.0	100.0
3.0	99.3	99.3	99.9	100.4	100.4	100.2	100.2	99.9
4.0	96.2	96.1	98.3	99.7	99.6	99.4	99.7	99.5
5.0	93.1	93.0	95.0	97.8	98.1	97.8	98.9	98.3
6.0	90.1	89.9	91.9	94.9	95.4	95.2	96.0	96.4
7.0	87.2	87.0	89.5	92.1	93.0	92.3	93.6	94.5
8.0	84.4	84.2	86.5	89.6	90.1	89.6	91.2	92.1
9.0	81.6	81.4	83.4	87.1	87.3	87.2	88.6	89.7
10.0	79.0	78.8	80.9	83.9	85.1	84.6	86.1	87.3
11.0	76.5	76.2	78.3	81.6	82.7	82.2	83.7	85.3
12.0	74.0	73.7	75.6	79.1	79.9	79.5	81.4	83.0
13.0	71.6	71.3	72.8	76.7	77.9	77.4	78.9	81.5
14.0	69.3	69.0	70.2	74.6	75.3	74.8	76.8	78.9
15.0	67.1	66.8	68.1	72.0	73.3	72.6	74.1	76.9
16.0	64.9	64.6	65.9	69.6	70.8	70.4	72.1	74.8
17.0	62.9	62.5	63.9	67.4	68.5	68.1	69.7	73.0
18.0	60.8	60.5	61.8	65.3	66.0	66.1	67.5	71.1
19.0	58.9	58.5	59.3	63.2	64.4	64.6	65.6	69.1
20.0	57.0	56.6	57.1	61.1	62.0	62.0	63.3	66.9

(a) Zero area TMRs calculated from narrow beam linear attenuation coefficient.

(b) Zero area TMRs extrapolated from TMR data.

Table 11 Comparison of the Tissue maximum ratios for cone 1, cone 2, and cone 3, which were derived from the FDD and NPSF, manual determination, and extrapolated from BJR suppl. 17 and MBPCC data and zero area TMR's.

Depth	Cone 1			Cone 2			Cone 3		
(cm)	(a)	(b)	(c)	(a)	(b)	(c)	(a)	(b)	(c)
2.8	100.0	100.0	100.0	100.0	100.0	100.0	100.0	100.0	100.0
3.0	99.9		100.0	100.4	.	100.0	100.4		100.0
4.0	98.3		97.8	99.7		98.8	99.6		99.2
5.0	95.0	95.2	95.8	97.8	97.0	97.2	98.1	98.1	97.7
6.0	91.9		92.7	94.9		94.3	95.4		95.0
7.0	89.5		89.7	92.1		91.4	93.0		92.1
8.0	86.3		86.9	89.6		88.7	90.1		89.4
9.0	83.4		84.3	87.1		86.1	87.3		86.9
10.0	80.9	81.0	81.7	83.9	83.7	83.6	85.1	84.7	84.4
11.0	78.3		79.1	81.6		81.0	82.7		81.8
12.0	75.6		76.7	79.1		78.6	79.9		79.4
13.0	72.8		74.3	76.7		76.1	77.9		77.0
14.0	70.2		72.0	74.6		73.9	75.3		74.8
15.0	68.1	68.1	69.7	72.0	71.4	71.6	73.3	72.7	72.5
16.0	65.9		67.5	69.6		69.3	70.8		70.2
17.0	63.9		65.3	67.4		67.1	68.5		68.1
18.0	61.8		63.2	65.3		65.1	66.0		66.0
19.0	59.3		61.1	63.2		62.9	64.4		63.9
20.0	57.1	58.3	59.1	61.1	61.1	60.8	62.0	62.1	61.7

(a) TMR's derived from FDD and NPSF.
(b) TMR's determined from Med Tech water phantom and Markus parallel plate chamber.
(c) Extrapolated TMR's from graph of zero area TMR's and primary collimator field sizes from BJR suppl. 17 and MBPCC data.

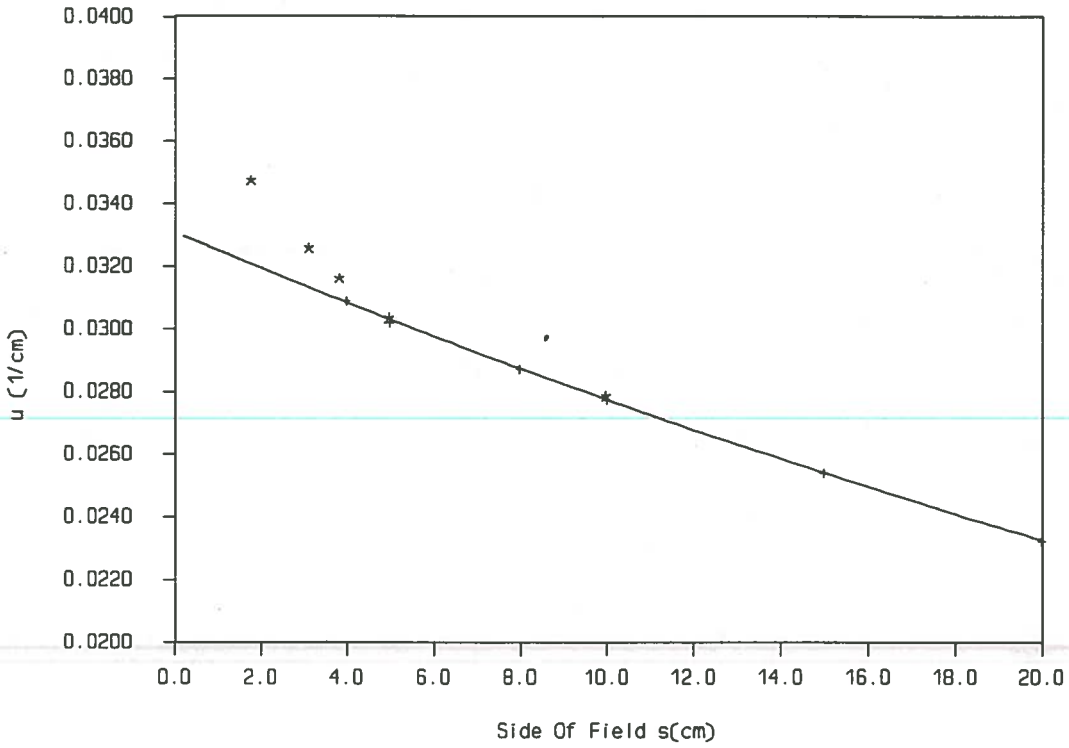

Figure 30 Graph of the TMR derived linear attenuation coefficients versus field size with the cone derived factors denoted by (*) and the collimator field sizes denoted by (+).

F. Treatment Isodose Distributions

Until a clear method is developed to accurately determine isodose plots for small fields, film will be the method of choice due to its high resolution capabilities even though the film shows an energy dependence and lack of water or tissue equivalency (Chierego et al., 1988, Colombo et al., 1985, Hartmann et al., 1985, Smith et al., 1989, Williamson et al., 1981). TLD's were used in limited studies using the 2cm cone for the multiple arc technique and single 140 degree arc rotation in conjunction with the Capintec RT110 treatment planning computer.

The isodensity data was not converted to isodose data for the lack of a computer controlled scanning densitometer and supporting software to convert isodensity plots to isodose plots. It should be remembered that the isodensity curves are not a true representation of the three dimensional dose distribution that occurs in tissue equivalent material because of its lack of tissue equivalency. However, film is used as the basis of comparison for the published isometric curves due to its high resolution capabilities (Chierego et al., 1988, Colombo et al., 1985, Hartmann et al., 1985, Smith et al., 1989).

The data presented here consists of film produced rotational isodensity curve and TLD isodose results. Each film was scanned by the Artronix film dosimetry system and maximum optical density reading was determined by the Macbeth manual densitometer. The optical density of the film was kept below 2.0 to prevent film saturation from distorting the isodensity plots in all experiments. The TLD results were converted to dose using the linear dose response curve with a dose constancy check

for each experiment.

The interest behind small field sizes on the order of 0.5cm to 4cm diameter is due to the rapid dose fall-off outside the target volume, measured by the distances from 90% or 80% isodose line, defined at the edge of the tumor volume, to lower values such as the 10% or 20% isodose lines with the idea of treating the target but sparing the normal tissue surrounding the target volume (Podgorsak et al., 1989). The optimal dose fall-off will occur with a 4-π distribution in a spherical phantom when all beams are directed towards the center. The resulting isodose distributions will be isotropic i.e., the same steepness in dose fall-off in all directions. However, due to constraints in patient setup and treatment, a 4-π geometry is not practical. Any other treatment technique will result in anisotropic isodose distributions that will have a maximum and minimum dose fall-off outside the target volume. The dose fall-off will therefore have to be characterized by the direction of interest with the maximum asymmetry occurring in the lower isodose region in the plane of rotation (Pike et al., 1990, Podgorsak et al., 1989). The dose fall-off is also found to be a minimum due to beam over lap outside the target volume. To maximize the rate of dose fall-off outside the target volume, parallel opposed beams should be avoided with a maximum arc rotation of 160 degrees and a minimum of 100 degrees with the minimum set to give adequate dose volume distribution within the normal tissue (Chierego et al., 1988, Pike et al., 1990, Podgorsak et al., 1989).

The multiple arc isodensity plots obtained in this work corroborated other studies using a series of photon energies, arc

angles, and arc numbers (Chierego et al., 1988, Colombo et al., 1985, Hartmann et al., 1985). From Chierego et al., 1988 and Jones et al., 1989 papers it was shown that photon energy did not significantly alter the shape of the isometric lines for the high dose regions, however, the low dose regions showed an increase spread as energy was increased. The other conditions that caused an effect in the low dose regions was the arc rotational angle and number of arcs used.

The experimental isodensity plot for the single 140 degree arc using cone 1 was compared to the isodose plot generated by the Capintec RT110 and the TLD derived isodose distribution in the axial plane. The isodensity plot gives a good approximation of the spatial dose distribution; however, it is recognized that the film shows an over response due to its energy dependence but still retains the spatial shape as seen in the Capintec RT110 isodose plot and TLD derived distribution. The variance in the TLD derived distribution from the Capintec isodose plan and the film is significant but could be related to the gradient created across the TLD's.

The five arc technique was limited in the arc angle achievable due to film saturation problems for the wax head phantoms. In the axial plane (with the Alderson head phantom) a 120 degree arc rotation was achievable which yielded optical densities ranging from 1.75 to 1.98 for cone 1, cone 2, and cone 3 at isocenter (Figures 31a, 32a, and 33a). However, under identical setup arrangements the sagittal and coronal planes (wax head phantom) exceeded an optical density of 2 due to the differences in the wax and Alderson phantom construction. The solution to the problem was to decrease the arc angle to prevent film saturation

from occurring. The sagittal (Figures 31b, 32b, and 33b) and coronal (Figures 31c, 32c, and 33c) films were limited to arc rotations of 100 degrees. The resulting optical densities ranged from 1.76 to 2.0 for both sagittal and coronal planes. The isodensity curves generated from the five arc technique displays the same characteristic isodensity/ isodose curves as seen in the published data (Figure 34) (Chierego et al., 1988, Pike et al., 1990, Podgorsak et al., 1989). Cross profiles scans were obtained for the axial, sagittal, and coronal planes according the cross sections drawn on Figure 31 for each cone (Figures 35a,c). The results of the beam diameters measured at 90% and 50% isodensity points for the axial, sagittal, and coronal planes showed a marked variation in beam widths depending on plane and axis scanned (Table 12) and also in comparison to table 1. The general view of the multi-arced profile is the broadening of the profile especially when the plane was within the parallel axis of rotation.

The use of TLDs for cone 1 for the five 120 degree arc technique in the axial plane yielded results which conflicted the results seen for film. However, the results do show the expected result of the film to over respond which would explain the discrepancy seen between the film and TLD results.

Due to the mu per degree limitation of the Clinac 20 and the five 120 degree arc method used, the optical density limitation of 2.0 was exceeded for cone 2 and cone 3 with the result being distortion of the isodensity plot. This was due to the central region (isocenter) becoming saturated (optical density reaches a maximum) which prevents additional radiation events from being detected. However the areas

which are not saturated are still detecting the events and respond by increasing the optical density. This situation causes a distortion in the relationship between the central region optical density (normalization point) and the subsequent isodensity points. The isodensity plots therefore are expanded in relation to a normal isodensity plot from a nonsaturated film. Due to the construction of the secondary collimator system the addition of a lead attenuator with sufficient thickness to prevent saturation from occurring for methods using multiple arcs paths greater than 100 degrees were not possible. It has been reported that the lead attenuator does not seriously distort the isodensity plot (Hartmann et al., 1985) but decreases the dose rate to a level which will prevent film saturation from occurring under experimental conditions and therefore allow larger arc angles to be used.

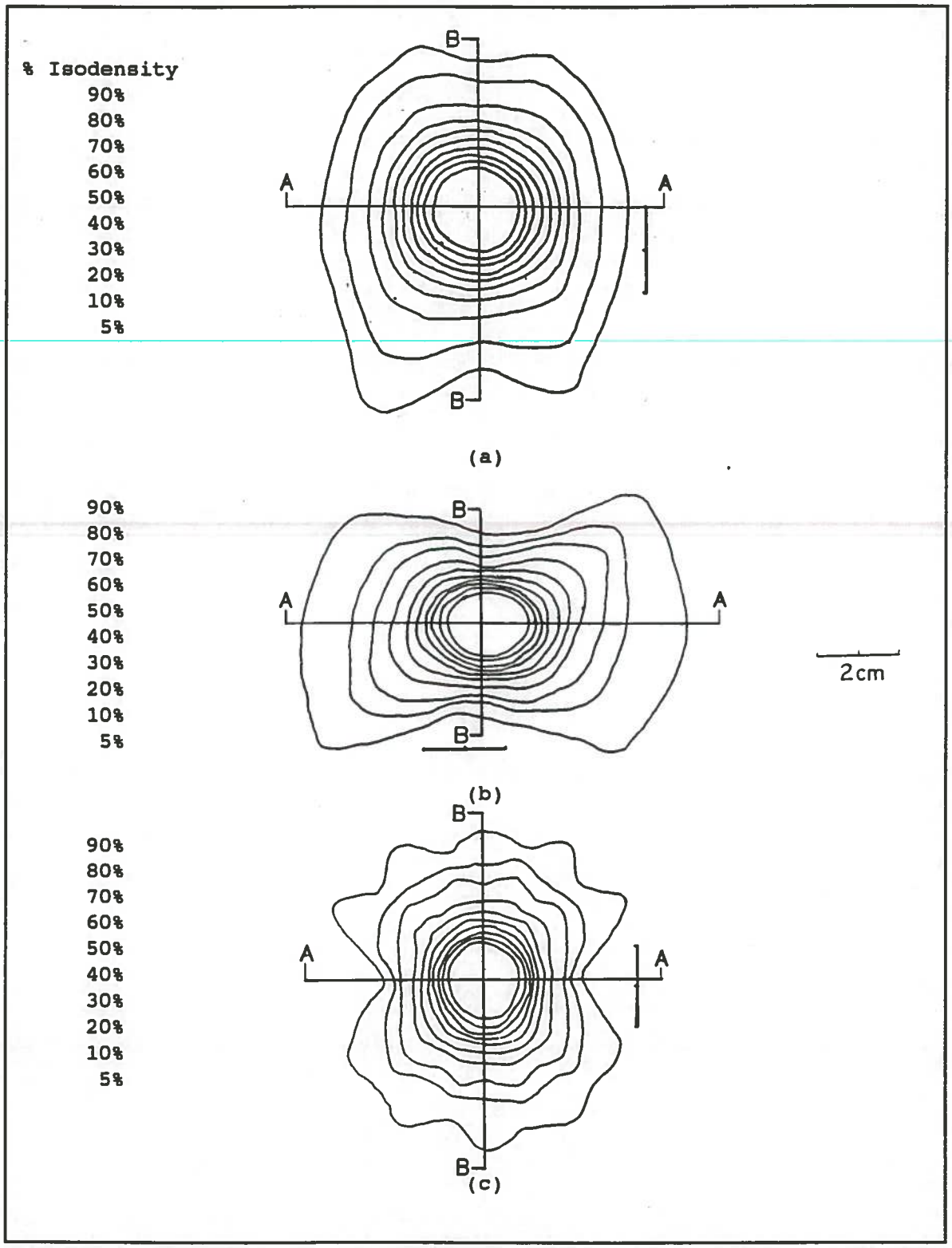

Figure 31 Isodensity distribution for cone 1 in the axial (a), sagittal (b), and coronal (c) planes for the five arc technique showing good approximation of spatial distribution using the Alderson and wax phantoms with film.

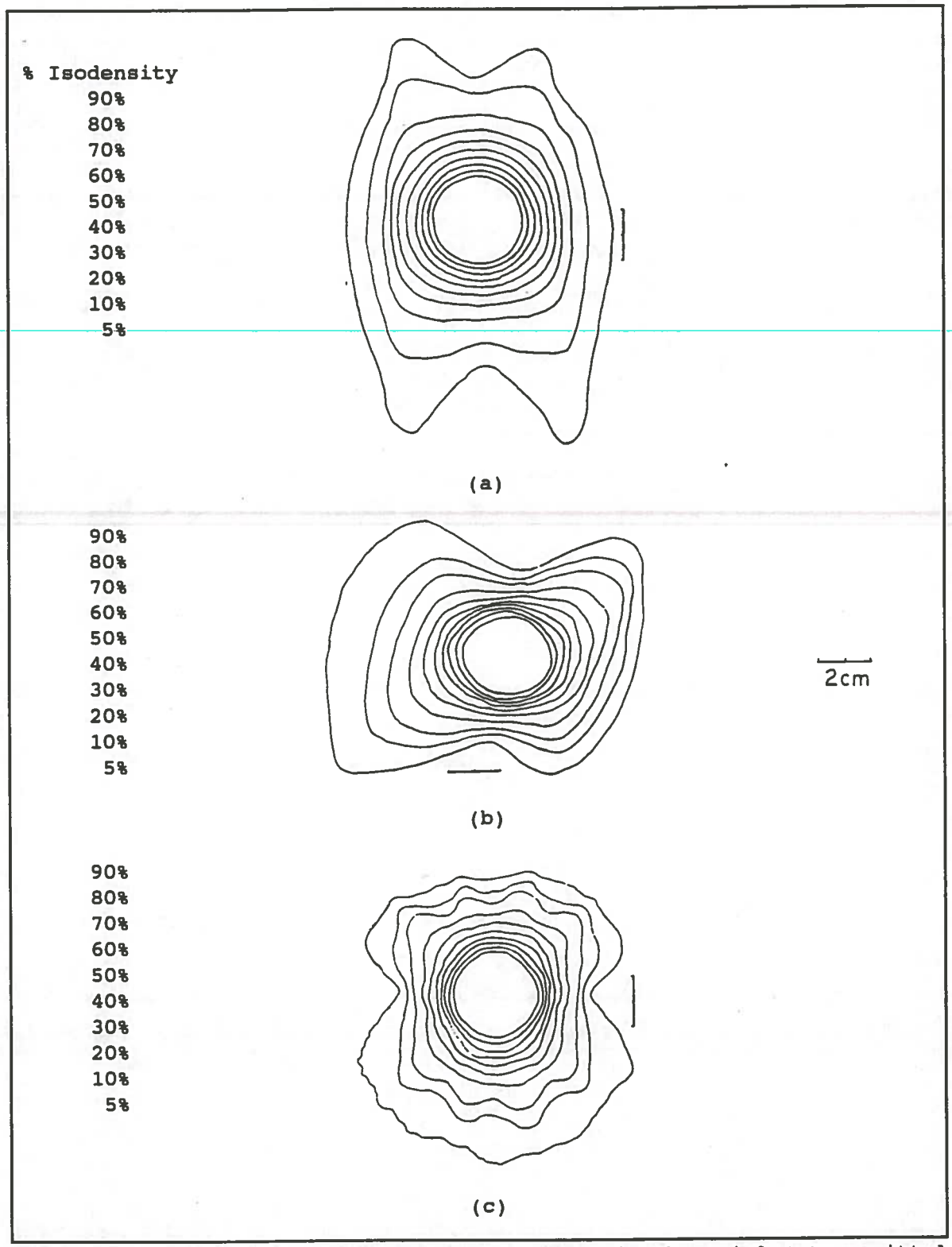

Figure 32 Isodensity distribution for cone 2 in the axial (a), sagittal (b), and coronal (c) planes for the five arc technique showing good approximation of spatial distribution using the Alderson and wax phantoms with film.

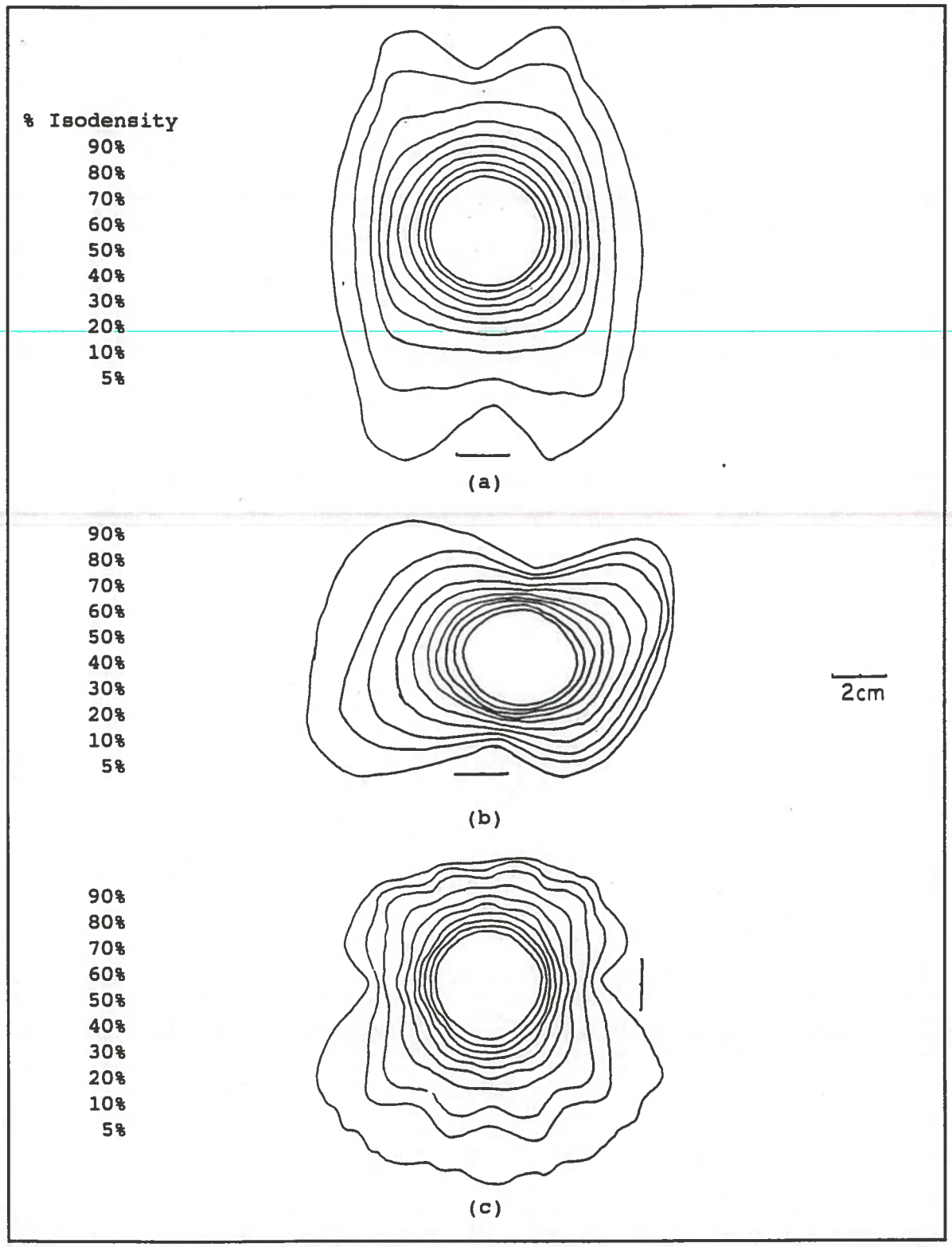

Figure 33 Isodensity distribution for cone 3 in the axial (a), sagittal (b), and coronal (c) planes for the five arc technique showing good approximation of spatial distribution using the Alderson and wax phantoms with film.

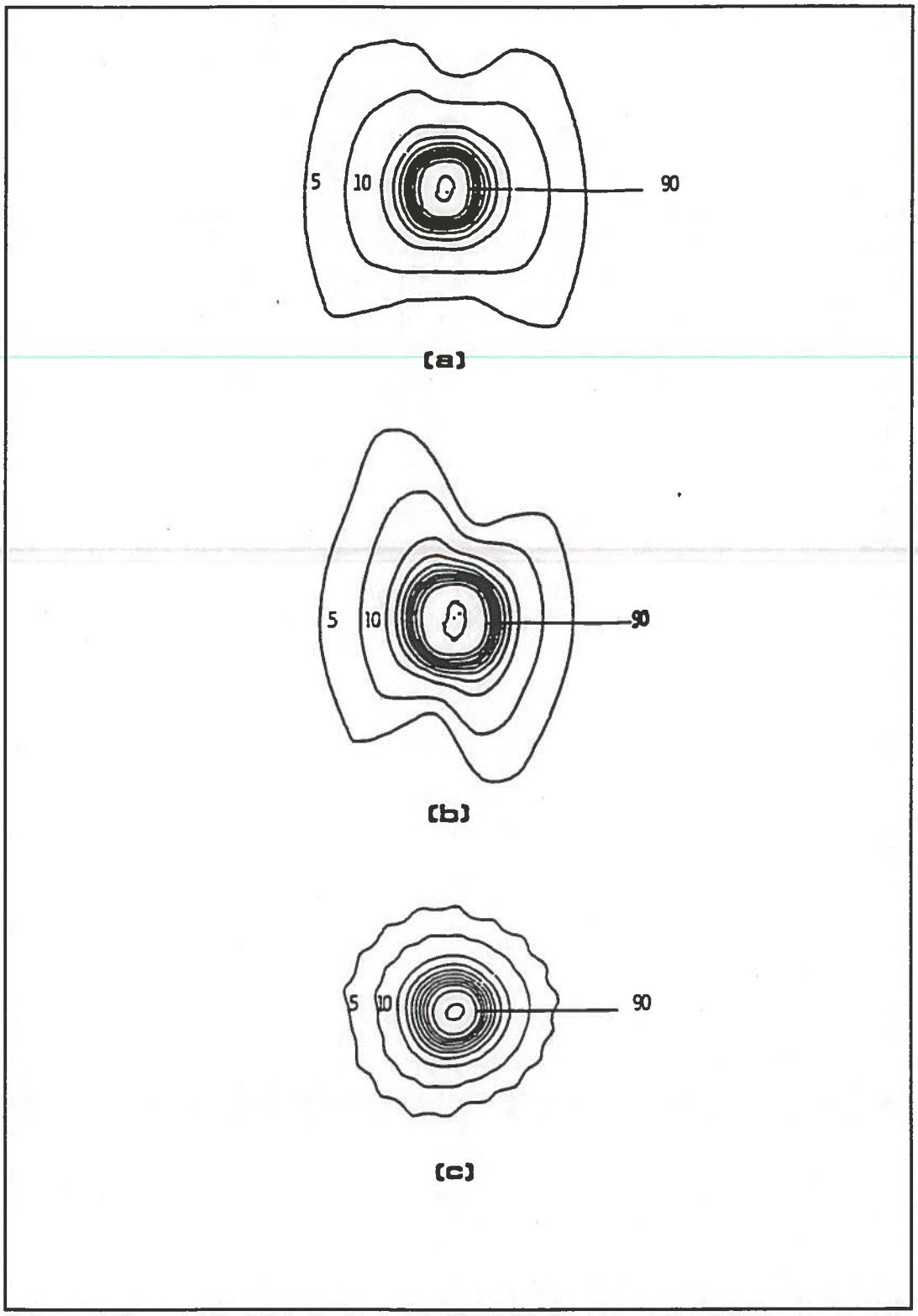

Figure 34 Isodose curves representing a typical multi-arced distribution in the three principle planes [(a) axial, (b) sagittal, and (c) coronal] (Chierego et al., 1988).

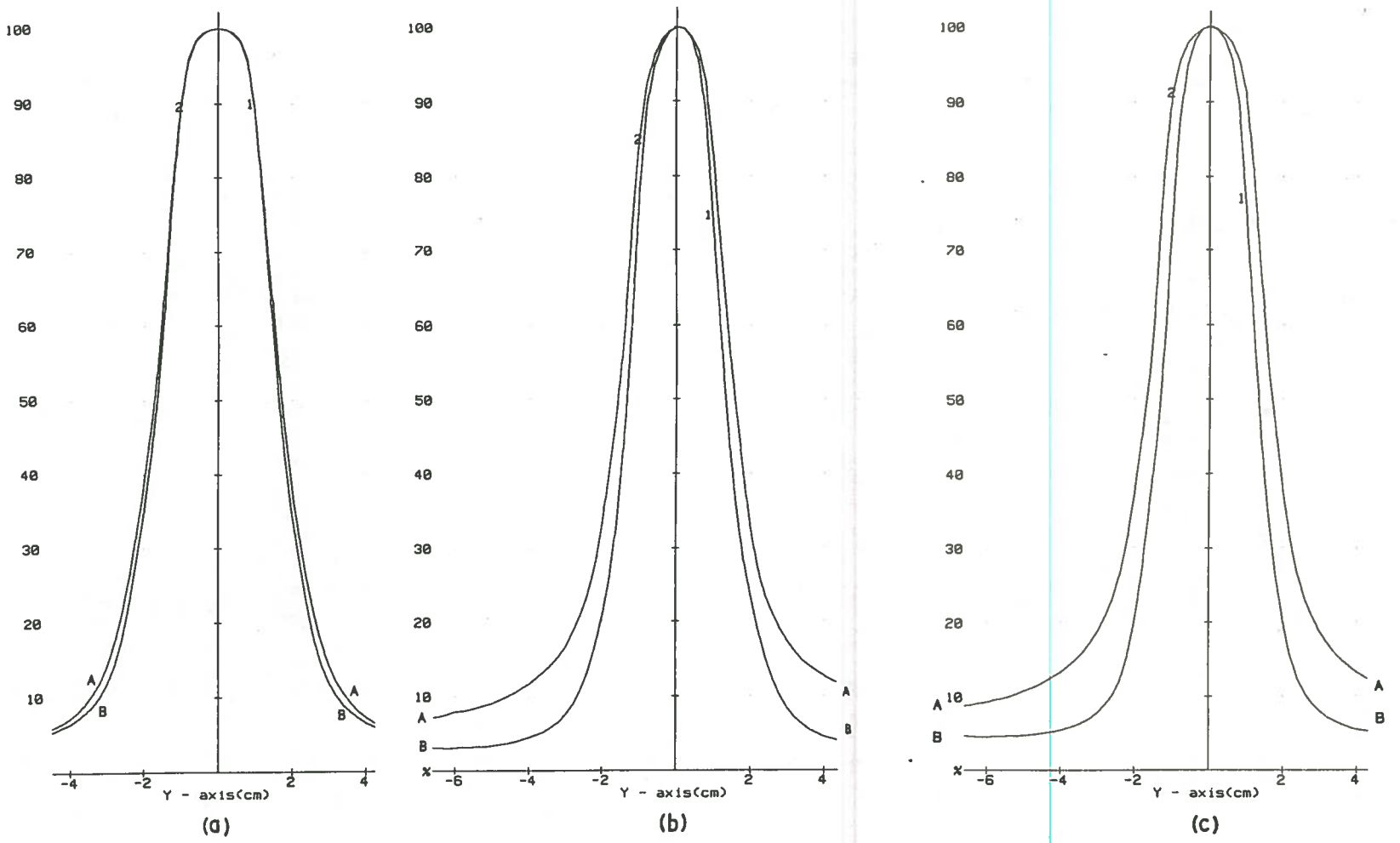

Figure 35a Crossprofile of cone 1 through the isodensity curves generated by the five arc technique with the scan direction shown by cross sections A-A and B-B as drawn in figure 31 for the axial (a), sagittal (b), and coronal (c) planes. A more pronounced spread is seen between cross sections A-A and B-B in the sagittal and coronal planes not seen in the axial plane. The difference is due to scan direction whether parallel (A-A) or perpendicular (B-B) to beam central axis.

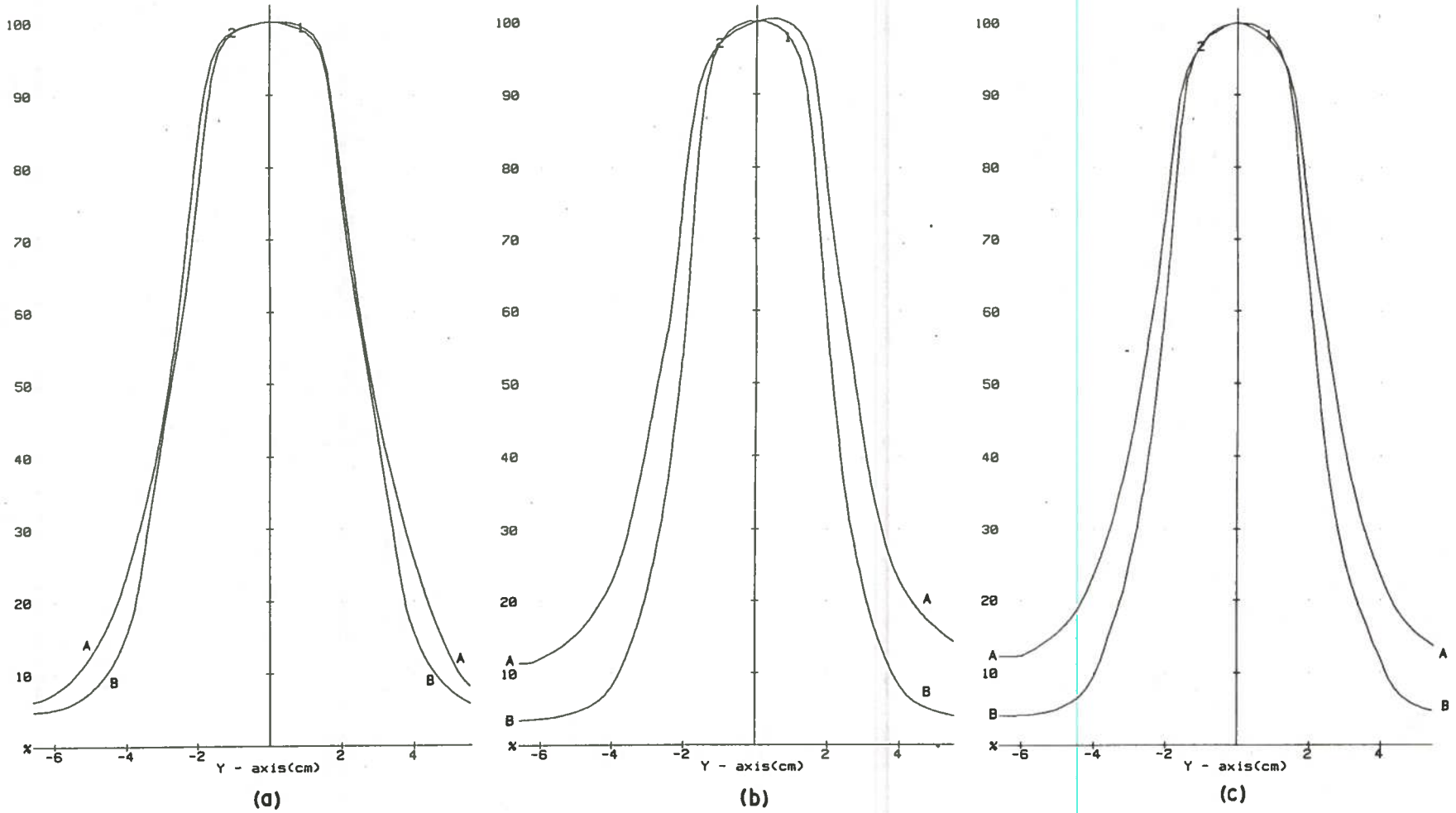

Figure 35b Crossprofile of cone 2 through the isodensity curves generated by the five arc technique with the scan direction shown by cross sections A-A and B-B as drawn in figure 31 for the axial (a), sagittal (b), and coronal (c) planes. A more pronounced spread is seen between cross sections A-A and B-B in the sagittal and coronal planes not seen in the axial plane. The difference is due to scan direction whether parallel (A-A) or perpendicular (B-B) to beam central axis.

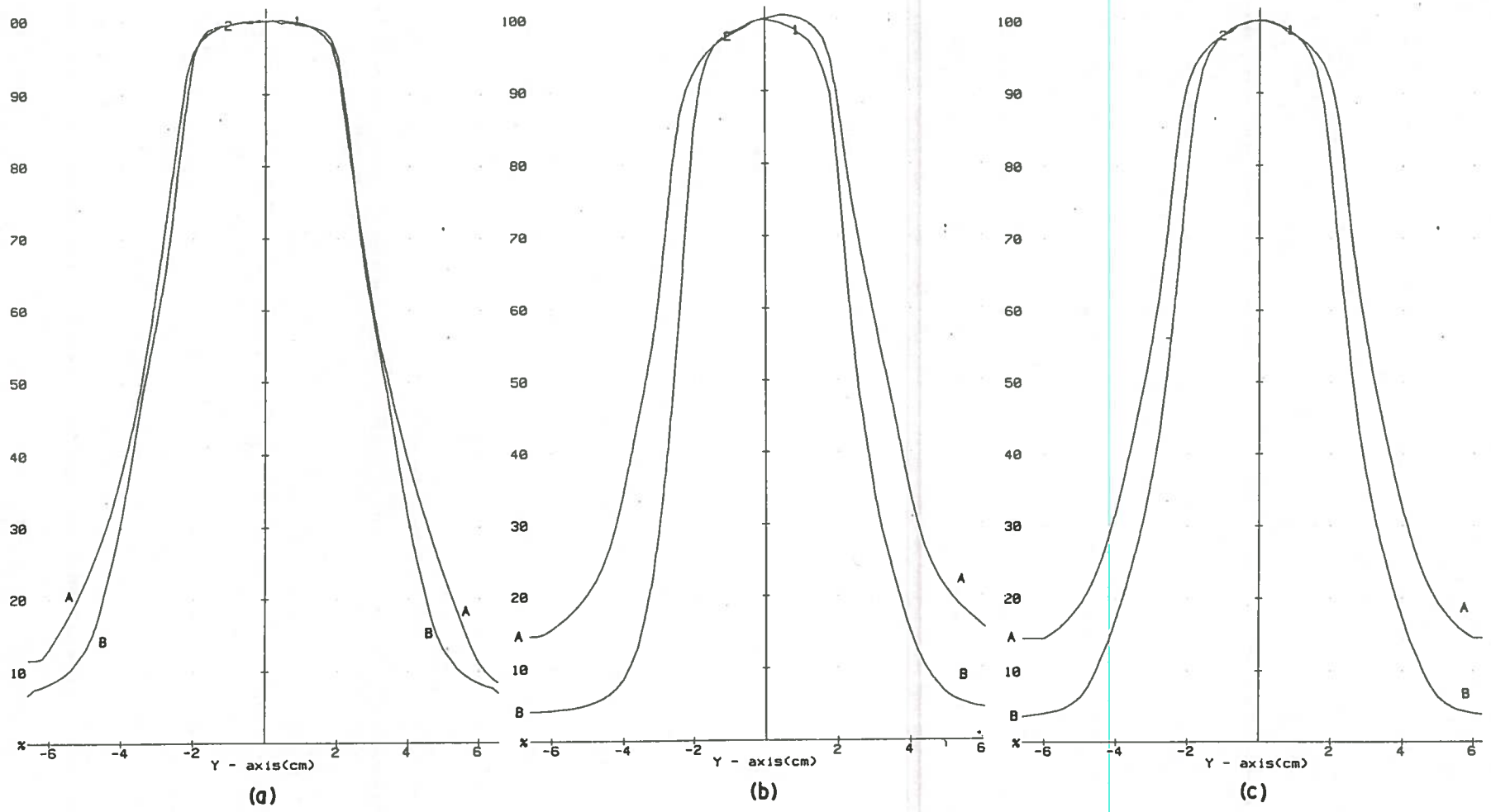

Figure 35c Crossprofile of cone 3 through the isodensity curves generated by the five arc technique with the scan direction shown by cross sections A-A and B-B as drawn in figure 31 for the axial (a), sagittal (b), and coronal (c) planes. A more pronounced spread is seen between cross sections A-A and B-B in the sagittal and coronal planes not seen in the axial plane. The difference is due to scan direction whether parallel (A-A) or perpendicular (B-B) to beam central axis.

Table 12 Five arc rotation showing the numerical results of the beam diameters measured along the cross sectional planes A-A and B-B for the axial, sagittal, and coronal planes for each cone.

	Cone 1		Cone 2		Cone 3	
Axial	A-A	B-B	A-A	B-B	A-A	B-B
90%	1.95cm	1.95cm	3.50cm	3.30cm	4.40cm	4.25cm
50%	3.35cm	3.45cm	5.60cm	5.50cm	6.85cm	6.65cm
Sagittal						
90%	1.70cm	1.50cm	3.35cm	2.80cm	4.15cm	3.60cm
50%	3.15cm	2.65cm	5.45cm	4.35cm	6.70cm	5.10cm
Coronal						
90%	2.00cm	1.50cm	3.20cm	2.95cm	4.15cm	3.35cm
50%	3.35cm	2.65cm	5.35cm	4.50cm	6.40cm	5.20cm

Where A-A and B-B are cross sectional diagram found in figure 31, 32, 33

I - 1.76 ± .23

II - 3.18 ± .26

III - 3.98 ± .41

CONCLUSION AND RECOMMENDATIONS

This study's emphasis was on the dosimetry of small stationary and rotational fields to be used with stereotactic treatment. The objective was to determine beam cross profiles, central axis depth dose, scatter correction factors, central axis tissue maximum ratios, and rotational isodensity curves of three specially designed small diameter cones.

The beam diameters defined for 90% isopoint for cone 1, cone 2, and cone 3 as specified by the manufacturer (2cm, 3cm, and 4cm respectively) were not achieved but were determined to be 1.5 +/- 0.1cm, 3.5 +/- 0.01cm and 4.3 +/- 0.03cm respectively. It was found that the penumbra width paralleled the results seen by Dawson and were found to vary from 10%/mm to 18%/mm depending on cone and specification point designated (90/10% or 80/20%).

The result of film versus diode detector in the delineation of the crossprofile shows no significate difference in the spatial resolution. However, it is recognized that the Artronix film scanning system and the diode have a finite detection area that is large compared to penumbra of the fields of interest. This leads to a question of scanning resolution and minimum width detectable which would affect the beam diameter, penumbra width, and the overall profile appearance. The solution would be to use a modified MacBeth isodensitometer or microscanning isodensitometer. The Macbeth is fitted with a plate drilled with a single small diameter pin hole (<1mm) which is fitted over the receiver diode. A micrometer film holding system is used to accurately place the film under the light emitting diode for measurement (per conversation

with Dr. Wendell Lutz).

The result from the film dose response measurements suggest that film does over respond on the order of 9.1 +/- 0.9% at depth when compared to dmax for a 10x10cm field size; however, this was not explored for the small fields being studied where the over response is possibly not seen. For future studies the film response needs to be evaluated for each of the cones and larger fields at depth to study the effects of the low energy scatter photons. The TLD dose response curve showed a linear response though the range of dose measurement (0-300 cGy). The TLDs were corrected for response by averaging the TLD output for a given dose of 100 cGy.

The evaluation of the central axis depth dose was used for a two fold purpose. First, to evaluate the Markus chamber/CRS system against known fractional depth doses and second to determine the central axis depth dose for each cone which will be used in the determination of the central axis tissue maximum ratios.

The comparison of the Markus chamber/CRS system determined fractional depth dose versus manual determination data fell within 2% for all fields as well as for the Markus chamber versus MBPCC and BJR Suppl. 17 data. Since no data exist for field sizes smaller than 4x4cm the only method to compare the depth doses determined for the cones was by extrapolation from known depth dose values and the use of the linear attenuation derived zero field size depth dose which yielded results within 1% of the CRS and manually derived depth dose. In summary the use of the Markus chamber and the CRS system gave good results in the determination of the central axis depth dose for all field sizes and

cones.

The experimentally determined narrow beam linear attenuation coefficient (0.0327 +/- 0.003 cm^{-1}) fell within the published value of 0.0326 cm^{-1} (van de Geijn et al., 1984, Thomas, 1970) and was found to be field size independent. However, cone 1 derived value (0.0334 cm^{-1}) did not fall within the experimental or published value which was possibly due to lack of electronic equilibrium.

The experimental results of the field size dependence in phantom fell within 2% of the MBPCC values with the difference being seen for the smaller field sizes. The deviation seen in figure 27 with the cone data is due to the constant primary and collimator scatter of the 5x5cm field with the cones contributing little to the primary/scatter component (Bjarngard et al.,1990).

The determination of the field size dependence in air resulted in values which were not confirmable with published values since it has been considered unmeasurable parameter in the past. Numerous detector/buildup combinations were used (Markus/superflab, Markus/high impact poly, PTW model 30-316/brass cap, and TLD) to determine the FSD_a with results falling within 2%. It was determined that the use of backscatter material was not necessary in in-air measurements using the Markus chamber combinations since the photon energy used primarily scatters in a forward and lateral directions. It was also seen that the output does not change with a change in the cone diameter if the primary collimator field size is held constant. This is explainable since no significant scatter contribution is seen from the cones (Bjarngard et al.,1990). The resulting curve generated by the ratio of the FSD_p and

FSD_s versus field size showed no deviation in the curve for the cone derived values since the NPSF is dependent only on area irradiated and is collimator field size independent. The NPSF results fell within 1% of the published values (BJR suppl. 17, 1983, Spicka et al., 1988). The resulting NPSF were fitted to a hyperbolic equation yielding a correlation coefficient (r^2) of 0.990 which was used in conjunction with the depth dose to determine the tissue maximum ratios.

The peak scatter factor (PSF) was determined for the 10x10cm field size using the PTW 0.6cc chamber and acrylic buildup cap with a measured value of 1.022 which is in good agreement with the published value of 1.021 (Personal communication from the RPC). For the other field sizes and cones the PSF was calculated by varying equation 9 using the known NPSF(s) and the PSF(10) with the results for the 20x20cm and 30x30cm within 0.5% of the expected values of 1.034 and 1.044 respectively (Personal communication with the RPC) (Table 9). The experimental determination of the peak scatter factor for a 5x5cm, 10x10cm, and 20x20cm field size using the brass buildup cap and the PTW 0.3cc chamber yielded results which were not consistent with the expected values. The experimental results yielded in-air measurements which were greater than the in-water measurements which yielded peak scatter factors ranging from 0.974 for the 20x20cm to 0.980 for the 5x5cm. The reason for this discrepancy is unknown and further evaluation is needed.

The cone TMR data was derived by three methods. First, following the conversion of the FDD and the use of NPSF's to calculate the TMR's; second, the manual determination using the Markus chamber; and third by extrapolation from a graph of zero area TMR's and collimator field sizes

from known data (BJR suppl. 17 and MBPCC). The resulting TMR's derived by FDD and NPSF were found to be within 2% of the manually derived values for each cone. The FDD/NPSF derived TMR data in comparison with the extrapolated TMR's for cone 1 showed a deviation of 3.5% at depth but decreased to minimum of 0.2% at the shallow depths with cones 2 and 3 within 1.0% at all depths. The TMR data for fields ranging from 4x4cm to 10x10cm were confirmed (within 2%) by both BRJ supplements 17 and the values used by MBPCC. The zero area TMR's obtained from both the narrow beam linear attenuation coefficient and the use of the linear attenuation coefficient derived value from the simple exponential portion of the TMR curves were in agreement with the published value with the exception of the cone TMR derived effective linear attenuation coefficient which showed a +16% variation.

The confirmation of the rotational isodensity plots consisted of the use of the Capintec RT110, TLD's, and published plots. The optical density of the film was kept below 2 to prevent film saturation from occurring which proved to be impossible during the five arc rotation using the wax head phantom. Therefore, the arc angle was reduced to 100 degrees per arc instead of the 120 degree per arc used for the Alderson head phantom. The comparison of the film derived isodensity plots with the Capintec RT110 for a single 140 degree arc showed that a discrepancy exist between the isodose generated curves from the Capintec and isodensity curves from film due to the energy dependence of the film and relationship of optical density to dose. The variation between the TLD's generated curve and the Capintec RT110 derived curve for a single 140 degree arc was significate. The study of the full five arc rotation

with arc angles limited by film saturation showed good spatial equivalency to the published curves.

In summary, the parameters required to calculate the monitor units necessary to deliver a specified dose at any depth along the central axis is obtainable with confidence with the experimentally derived values. The determination of the cross profiles and rotational isodensity curves utilizing the Artronic scanning isodensitometer are questionable in relation to its resolution accuracy and should be studied further.

The next step in this quest for an radiosurgical program is to repeat this study utilizing the 4 or 6 MV photon which has been studied extensively and found to give the best over all results (Chierego et al., 1988).

BIBLIOGRAPHY

Arcovito, G., Piermattei, A., D'Abramo, G., Bassi, F.A. (1985). Dose measurements and calculations of small radiation fields for 9-MV x rays. Med. Phys., 12(6), 779-784.

Bjarngard, B.E., Tsai J.-S., Rice R.K. (1990). Doses on the central axes of narrow 6-MV x-ray beams. Med. Phys. 17(5), 794-799.

Chierego, G., Marchetti, C., Avanzo, R.C., Pozza, F., Colombo, F. (1988). Dosimetric considerations on multiple arc stereotaxic radiotherapy. Radiotherapy and Oncology, 12, 141-152.

Cohen M., Jones D.E.A., Greene D. (1972). Central axis depth dose data for use in radiotherapy. British J. Radiol. Suppl. No. 11, pp. 81 and 95-100

Cohen M., Jones D.E.A., Greene D. (1983). Central axis depth dose data for use in radiotherapy. British J. Radiol. Suppl. No. 17, pp. 80-81, 110, 115-119, and 131-142

Colombo, F., Benedetti, A., Pozza, F. Avanzo, R. Marchetti, C., Zanardo, A. (1985). External stereotactic irradiation by a linear accelerator. Neurosurgery, 16, 160

Columbo, F., Benedetti, A., Pozza, F., Zanardo, C., Avanzo, Marchetti, C. (1985). Stereotactic radiosurgery utilizing a linear accelerator. Appl. Neurophysiol. 48, 133-145

Dawson, D.J., Schroeder, N.J., Hoya, J.D. (1986). Penumbra measurements in water for high-energy x rays. Med. Phys. 13(1), 101-104

Dawson, D.J., Harper, J.M., Akinradewo, A.C. (1984). Analysis of physical perimeters associated with the measurement of high energy x-ray penumbra. Med. Phys. 11(4), 491-497

Geijn van de, J., Fraass, B.A. (1984). The net fractional depth dose: A basis for a unified analytical description of FDD, TAR, TMR, and TPR. Med. Phys. 11(6), 784-793

Gutin, P.H., Hosobuchi, Y., Philips, T.L., Stupar, T.A. (1981). Stereotactic interstitial irradiation for the treatment of brain tumors. Cancer Treatment Report 65(suppl. 2), 103-106

Hariz, M.I., Henriksson, R., Lofrth, P.O., Latainen, L.V., Saterborg, N.E. (1990). A non-invasive method for fractionated stereotactic irradiation of brain tumors with linear accelerator. Radiotherapy and Oncology 17, 57-72.

Hartmann, G.H., Schlegal, W., Strum, V., Kober, B.Pastyr, O., Lonenz, W.J. (1985). Cerebral radiation surgery using moving field irradiation at a linear accelerator facility. Int. J Radiat. Oncol. Biol. Phys. 11, 1185-1192.

Holt, J.G., Laughlin, J.S., Moroney, M.A. (1970). The extention of the concept of tissue-air ratios (TAR) to high energy beams. Radiology 96, 437-446

Horn, R.A. (1981). Computer programs for output and depth dose from hyperbolic equations. Med. Phys. 8(1), 108-110

Hosobuchi, Y., Philips, T.L., Stupar, T.A., Gutin, P.H. (1980). Interstitial brachytherapy of primary brain tumors. J. Neurosurg. 53, 613-617

Houdek, P.V., Fayos, J.V., VanBuren, J.M., Ginsberg, M.S. (1985). Stereotaxic radiotherapy technique of small intracranial lesions. Med Phys 12, 469-472

Houdek, P.V., VanBuren, J.M., Fayos, J.V. (1983). Dosimetry of small radiation field for 10-MV Xrays . Med Phys 10, 333-336

Ikoro, N.C., Johnson, D.A., Antich, P.P. (1987). Characteristics of the 6-MV photon beam produced by a dual energy linear accelerator. Med. Phys. 14(1), 93-97

Jones, D., Christopherson, D.A., Hafermann, M.D. (1989). A technique for fractionated radiosurgery. Paper no. 7 AAPM annual meeting, Memphis, TN.

Kubsad, S.S., M. Rockwell, M.A. Gehring, D.J. Misisco, B.R. Paliwal, M.P. Mehta, T.J. Kinsella, (1990) Monte carlo and convolution dosimetry for stereotactic radiosurgery. Int. J. Radiat. Oncol. Biol. Phys. 19, 1027-1035

Larsson, B., Liden, K., Sarby, B. (1974). Irradiation of small structures through intact skull. Acta Radiol. TPB 13, 513-534

Leksell, D. (1987). Stereotactic radiosurgery: Present status and current trends. Neurological Research. 9, 60-68

Leksell, L. (1983). Stereotactic radiosurgery. J. Neurology, Neurosurgery, and Psychiatry 46, 797-803

Leksell, L. (1951). Stereotactic method and radiosurgery of the brain. Acta Chir. Scand. 102 , 316-319

Lutz, W., Winston, K.R., Malek, N. (1988). A system for stereotactic radiosurgery with a linear accelerator. Int. J. Radiat. Oncol. Biol. Phys. 14, 373-381

Mackay, A.R., Gutin, P.H., Hosobuchi, Y., Norman, D. (1982). Computed tomography-directed stereotaxy for biopsy and interstitial irradiation of brain tumors: Technical note. Neurosurgery 11(1), 38-42

Marin-Grez, M. (1983). High dose percutaneous stereotactic irradiation of solitary brain metastases using a 15 MeV linear accelerator, (Abstrct). Int. J. Radiat. Onc. Biol. Phys. 15(S1), 231

Mellenberg, D.E. (1990) Determination of build-up region over-response corrections for a Markus type chamber. Med Phys., 17(6), 1041-1044

Mohan R., Chui, C. (1985). Energy and angular distribution of photons from medical linear accelerators. Med. Phys. 12(5), 592-597

Nath, R., Schulz, R.J. (1977). On the choice of material for half-value-layer measurements for megavoltage x rays. Med. Phys. 4(2), 132-133

Phillips, M.H., Frankel, K.A., Lyman, J.T., Frabrikant, J.I., Levy, R.P. (1989). Comparison of different radiation type and irradiation geometries in stereotactic radiosurgery. Research Medicine and Radiation Biophysics Division,Lawerence Berkley Laboratory

Pike, B., Peters, T.M., Podgorsak, E.B., Pla, C., Olivier, Souhami, L. (1990). Dose distribution in radiosurgery. Med. Phys. 17(2), 296-304

Pike, B., Peters, T.M., Podgorsak, E.B., Pla, C., Olivier, A., de Lotbiniere, A. (1987). Stereotactic external beam calculations for radiosurical treatment of brain lesions. Appl. Neurophysiol. 50, 269-273

Pike, B., Peters, T.M., Podgorsak, E.B., Pla, C. (1987). Dose distributions in dynamic stereotactic radiosurgery. Med Phys. 14, 780-789

Podgorsak, E.B., Olivier, A., Pla, M., Lefebure, P.Y. Hazel, J., Pike, B. (1988). Dynamic stereotactic radiosurgery. Int. J. Radiat. Oncol. Biol. Phys. 14, 115-125

Podgorsak, E.B., Pike, B. Olivier, A., Pla, M., Lefebure, P.Y. (1989). Radiosurgery with high energy photon Beams: A comparison among techniques. Int. J. Radiat. Oncol. Biol. Phys. 16, 857-865

Rice, R.K., Hansen, J.L., Svenson, G.K., Siddon, R.L. (1987). Measurements of dose distribution in small beams of 6-MV Xrays. Phys Med. Biol. 32, 1087-1099

Ricker, G. and Grusell, E. (1987). General specifications for silicon semiconductors for use in radiation dosimetry. Phys. Med. Biol. 39, 1109-1117

Saunders, W.M., Winston, K.R., Siddon, R.L., Svensson, G.H., Kijewski, P.K., Rice, R.K., Hansen, J.L., Barth, N.H. (1988). Radiosurgery for arteriovenous malformations of the brain using a standard linear accelerator: rationale and technique. Int. J. Radiat. Oncol. Biol. Phys. 15(2), 441-447

Smith, V., Schell, M.C., Larson, D.A. (1989). The role of tertiary collimation for linac-based radiosurgery . American Association of Physicist in Medicine Annual Meeting.

Spicka, J., Herron, D., Orton, C. (1988). Separating output factor into collimator factor and phantom scatter factor for megavoltage photon calculations. Medical Dosimetry. 13, 23-24

Sturm, V. Kober, K., Hover, K., Schegel, W., Boesecke, R., Pastyr, O., Hartmann, G., Schabbert, S., Winkel, K., Kunze, S., Lorenz, W. (1987). Stereotactic percutaneous single dose irradiation of brain metastasis with a linear accelerator. Int. J. Radiation Oncology Biol. Phys. 13, 179-287

Task Group 21, Radiation Therapy Committe, AAPM (1983). A protocol for the determination of absorbed dose from high-energy photon and electron beams. Med. Phys. 10(6), 1-31

Van Dye, J. (1977). Practical dosimetric consideration of a 10-MV photon beam. Med. PHYS. 4(2), 145-153

Williamson, J.F., Khan, F.M., Sharma, S.C. (1981). Film dosimetry of megavoltage photon beams: A practical method of isodensity-to-isodose curve conversion. Med. Phys. 8(1), 94-98

VITA

Steven Cooper Harrell was born on February 20, 1963, in Bitburg, West Germany (Spangdahlem Air Force Base). He moved back to Baton Rouge, Louisiana in 1964. In May 1981, he graduated from University High School in Baton Rouge. In 1987, he obtained his Bachelor of Science Degree in Industrial Technology (Nuclear Science option) from Louisiana State University in Baton Rouge, Louisiana. He was accepted into post-graduate studies at Louisiana State University Nuclear Science Center with a full graduate assistantship. He entered graduate school in August, 1987 and in August, 1988, the assistantship duties, continued course work, and clinical training were transferred to Mary Bird Perkins Cancer Center. He is currently a candidate for the Master of Science Degree in Nuclear Science, Medical Radiation Science Option, and is presently employed with Department of Radiation Oncology at Florida Hospital in Orlando, Florida.

Harrell, Steven Cooper, B.S., Louisiana State University, 1987
Master of Science, Spring Commencement, 1992
Major: Nuclear Science (Medical Radiation Science Option)
Dosimetry of Small Fields used in Stereotactic Radiosurgery utilizing 15-MV Photons from a Linear Accelerator
Thesis directed by Oscar Hidalgo-Salvatierra
Pages in Thesis, 125. Words in Abstract, 234.

ABSTRACT

Dosimetric parameters have been determined for the small fields used in stereotactic radiosurgery utilizing the 15 MV photons from a Varian Clinac 20 linear accelerator. The specific parameters measured consisted of linear attenuation coefficients both narrow beam and TMR derived ($\mu_o(cm^{-1})$), fractional depth dose (FDD), total scatter correction factor (S_t), collimator scatter correction factor (S_c), phantom scatter factor (S_p), and tissue maximum ratio (TMR). Radiographic methods were utilized for cross profile determination due to its high spatial resolution in tandem with computer controlled beam scanner utilizing the diode detector. Isodensity plots for each cone were determined in the three principle planes (axial, sagittal, and coronal) utilizing radiographic methods and TLD.

The fractional depth dose and tissue maximum ratios showed the characteristic rapid dose fall off at shallow depths towards the zero area values for the small fields and approached the zero area values at deeper depth for the same field sizes. The total scatter correction factor showed a rapid dose fall off for the small field sizes towards the zero area and a divergence from the expected curve due to the constant head scatter. The collimator scatter factor displayed a

constant output for each cone and the same divergence as seen from the total scatter curve. The phantom scatter component did not display this characteristic curve since it is collimator field size independent and only dependent on area of phantom irradiated.